# REPORT DOCUMENTATION PAGE

*Form Approved*
*OMB No. 0704-0188*

**1. REPORT DATE** *(DD-MM-YYYY)*
05-10-2013

**2. REPORT TYPE**

**3. DATES COVERED** *(From - To)*

**4. TITLE AND SUBTITLE**

Numerical Modeling of High Irradiance Electromagnetic Beam Effects on Composite and Polymer Materials

**5a. CONTRACT NUMBER**

**5b. GRANT NUMBER**

**5c. PROGRAM ELEMENT NUMBER**

**6. AUTHOR(S)**
Tresansky, Andrew Christopher

**5d. PROJECT NUMBER**

**5e. TASK NUMBER**

**5f. WORK UNIT NUMBER**

**7. PERFORMING ORGANIZATION NAME(S) AND ADDRESS(ES)**

**8. PERFORMING ORGANIZATION REPORT NUMBER**

**9. SPONSORING / MONITORING AGENCY NAME(S) AND ADDRESS(ES)**
U.S. Naval Academy
Annapolis, MD 21402

**10. SPONSOR/MONITOR'S ACRONYM(S)**

**11. SPONSOR/MONITOR'S REPORT NUMBER(S)**
Trident Scholar Report no. 422 (2013)

**12. DISTRIBUTION / AVAILABILITY STATEMENT**

This document has been approved for public release; its distribution is UNLIMITED.

**13. SUPPLEMENTARY NOTES**

**14. ABSTRACT**

The US Navy faces a growing threat of cheaply produced UAVs and small boats that can attack en masse. Current kinetic defenses to these attacks include missiles and guns (like the CWIS). These defenses fall short because they have very limited magazine size and the cost of using them far outweighs the cost of the target they are defeating. High Energy Lasers (HEL) as Directed Energy Weapons (DEW) provide an alternative. In order to best employ this promising technology the effect of HEL on potential targets needs to be fully understood. The research presented here focused on the effects of HEL on the irradiance (energy per area) and wavelength regime of current interest to the US Navy on simple polymer and carbon fiber reinforced polymer composite materials. A physics-based computer model was developed using COMSOL Multiphysics™ (a computational modeling software) together with material property inputs determined using Differential Scanning Calorimetery (DSC), near infrared (NIR) Fiber Optic Reflectance Spectroscopy (FORS) and the Laser Flash Method (LFM). The model is used to predict the temperature field, heat affected zone (HAZ) and through thickness material removal that HEL irradiation causes in polymer and composite materials. The model predictions were compared to the experimental data and a sensitivity analysis was conducted on the model.

**15. SUBJECT TERMS**
HEL, NIR, Model, COMSOL, Irradiation, Laser, Directed Energy, Composites, Acrylite, DEW

**16. SECURITY CLASSIFICATION OF:**

**a. REPORT**

**b. ABSTRACT**

**c. THIS PAGE**

**17. LIMITATION OF ABSTRACT**

**18. NUMBER OF PAGES**
79

**19a. NAME OF RESPONSIBLE PERSON**

**19b. TELEPHONE NUMBER** *(include area code)*

U.S.N.A. --- Trident Scholar project report; no. 422 (2013)

# NUMERICAL MODELING OF HIGH IRRADIANCE ELECTROMAGNETIC BEAM EFFECTS ON COMPOSITE AND POLYMER MATERIALS

by

Midshipman 1/c Andrew C. Tresansky
United States Naval Academy
Annapolis, Maryland

Certification of Adviser(s) Approval

Associate Professor Peter Joyce
Mechanical Engineering Department

Associate Professor Joshua J. Radice
Mechanical Engineering Department

CAPT Richard J. Watkins, USN
Mechanical Engineering Department

Acceptance for the Trident Scholar Committee

Professor Maria J. Schroeder
Associate Director of Midshipman Research

## **ABSTRACT:**

The US Navy faces a growing threat of cheaply produced UAVs and small boats that can attack en masse. These vehicles could have as benign an intent as surveillance, or be as belligerent as armed or kamikaze drones. Current kinetic defenses to these attacks include missiles and guns (like the CWIS). These defenses fall short because they have very limited magazine size and the cost of using them far outweighs the cost of the target they are defeating. High Energy Lasers (HEL) as Directed Energy Weapons (DEW) provide an alternative to these weapons that have an infinite magazine, low dwell time on target, and have a cost per shot determined only by the electricity they use.

In order to best employ this promising technology the effect of HELs on potential targets needs to be fully understood. Studies have been conducted on the effects of lasers on different target materials, as well as the modeling of these effects. The research presented here focused on the effects of HEL in the irradiance (energy per area) and wavelength regime of current interest to the US Navy on simple polymer and carbon fiber reinforced polymer composite materials. This model would have applications for improving the US Navy's DEW as well as improving its ability to counter enemy DEW (C-DEW).

A physics-based computer model was developed using COMSOL Multiphysics™ (a computational modeling software) together with material property inputs determined using Differential Scanning Calorimetery (DSC), near infrared (NIR) Fiber Optic Reflectance Spectroscopy (FORS) and the Laser Flash Method (LFM). The model is used to predict the temperature field, heat affected zone (HAZ) and through thickness material removal that HEL irradiation causes in polymer and composite materials.

The heat transfer model was created in an axisymmetric domain. Radius and through thickness depth were the two dimensions modeled. A heat transfer model applies the heat diffusion equation to a domain, and then boundary conditions to the edges of that domain. The laser incident on the upper boundary was approximated as a surface heat flux. Convection and surface to ambient radiation were applied to both the upper and lower faces of the domain modeled. A material removal mechanism was incorporated with the heat diffusion equation for the interior of the domain.

Laser heating causes extremely high temperatures that can vaporize or rapidly oxidize materials. These effects cause material to be removed from the surface the laser is incident on. As material is removed, the laser becomes incident on the underlying material, and in this way drills through the material (in the through thickness direction). The movement of the incident face of the laser through thickness concomitantly moves the area where the heat is applied. This significantly changes the heat transfer problem being modeled. Failure to include material removal in a heat transfer model of laser heating leads to order of magnitude scale errors in surface temperature. To prevent this, a material removal mechanism was incorporated into the model.

Material removal can be, and has previously been, accomplished by remeshing the computational domain being modeled after each time step and removing vaporized/oxidized elements. This approach is difficult to implement, creates complex topographies and is computationally expensive. In this paper, material removal was accomplished by actuating the material properties of ablated elements to make them behave as if they had been removed (without physically removing them). Material properties were actuated using smoothed Heaviside functions over experimentally determined temperature ranges.

The model was then validated by experiments in the USNA Directed Energy Research Center. A comparatively easy to model polymer, carbon black loaded Acrylite, and more complicated carbon fiber/epoxy composite were irradiated with an HEL. Front face and rear face temperatures were recorded and the material recession rate was measured. The model predictions were compared to the experimental data and a sensitivity analysis was conducted on the model. The model was then iterated to higher accuracy by improving the mesh density, material properties and model geometry. The experimental and theoretical recession rates and surface temperatures were compared.

**KEYWORDS:**

HEL, NIR, Model, COMSOL, Irradiation, Laser, Directed Energy, Composites, Acrylite, DEW

## ACKNOWLEDGEMENTS:

I would like to thank Professor Maria Schroeder of the Trident Scholar Office, Sarwat Chappel and Dr. Lew DeSandre from the Office of Naval Research (ONR), and Quentin Saulter and Don Seeley from the High Energy Laser Joint Technology Office (HEL-JTO) for supporting and funding this research.

I am grateful to Dr. Robert Cozzens from Naval Research Laboratory (NRL) for providing continued guidance throughout this project as well as hosting me for a summer internship at NRL. Dr Chris Lloyd of Naval Surface Warfare Center (NSWC) Dahlgren, ENS Joe Puishys, and Professors Robert Ferrante and Joe Lomax from the USNA Chemistry Department all provided technical assistance throughout this research.

The help of Cort Lillard in setting up the computer to control the HEL as well as around the lab was extremely valuable. Norm Tyson and Jesse Baldwin were also instrumental in keeping the lab working as planned.

Thank you to Dr. Suzanne Lomax and Dr. John Delaney at the National Gallery of Art for performing the FORS measurements used in the research. Thank you also to Dr. Jin Gyu Park at the High-Performance Materials Institute of Florida State University for providing the LFM data used.

Special thanks are due to my advisors Professors Peter Joyce, Joshua Radice and CAPT Joe Watkins. The countless hours of assistance they have provided (many of which kept them at the Academy late) are testament to their commitment to their students.

Finally, the care and support of my parents, family, friends, and my teammates is what got me through the Academy and helped me to complete this project, thank you.

## TABLE OF CONTENTS

**TABLE OF FIGURES**

## INTRODUCTION:

High energy lasers (HEL) have been developing at a remarkable pace. Significant time and money have been invested into making deployable laser weapons for missions including (but not limited to): counter rocket artillery and mortar (C-RAM), ballistic missile defense (BMD) as well as counter unmanned aerial vehicle (C-UAV) and small boat defeat [1]. Directed energy weapons offer significant advantages over the conventional weapons that currently serve these roles. They have essentially infinite ammunition at the minimal cost of the electricity needed for power, they have higher probability of hits and kills on targets than certain kinetic systems, and in many cases they have shorter engagement and dwell times [1]. This is a solution to the growing problem of using increasingly expensive weapons (like multi-million dollar missiles) on cheaply produced enemy targets attacking en masse.

Notable successes towards employing HEL have been achieved. The Air Force's Airborne Laser (ABL) was a Chemical Oxygen Iodine Laser (COIL) installed in a converted Boeing 747 that was able to shoot down ballistic missiles in flight. Ground based lasers have demonstrated success in shooting down multiple artillery shells and rockets, and sea based lasers have had success in shooting down UAVs and disabling small boats [1]. Obviously the US Navy is interested in the sea based variety; however employing HEL on a maritime platform generates unique challenges. These include: target tracking and jitter control issues from a pitching and yawing ship as well as propagation through a maritime environment and operation in a saltwater environment. However, significant progress has been made, and the technology to deploy HEL as DEW is accessible [1]. In fact, the solid state laser technology maturation program (SSLTM) is a path towards deployable laser weapons that has led to the Laser Weapon System (LaWS) being deployed on the USS Dewey and being slated to be deployed on the USS Ponce [1].

Traditional kinetic weapons such as bullets and missiles create effects that are relatively well understood: bullets deliver kinetic energy and make holes in the target, and missiles release chemical energy and explode. These effects are tested and characterized, then the military designs new weapons that maximize these effects i.e. the bunker buster bomb or the armor piercing round. Knowledge about the effects of these weapons also allows our military to better counter these weapons through better armor designs or more survivable structures.

The benefits of HEL as directed energy weapons are presented in their very name. Instead of using a projectile or missile to carry kinetic or potential energy to a target, the energy is directed and instantaneously applied to the target. In the case of a fast moving target such as C-RAM or BMD, the ability to instantaneously engage the target would be a game changing capability. The directly applied energy is absorbed and causes damage through intense localized heating. The focused and localized nature of this heating explains how HELs work as weapons.

For example, a 100W heat lamp and a 100W laser both generate radiation at the same rate (100 Watts). When incident on a surface the energy from the heat lamp is spread out (low irradiance or energy per area) and the heat is conducted and dissipated by the material. (The measure of a material's ability to spread heat by conduction is thermal diffusivity). Conversely, the laser delivers the energy in a much smaller area and consequently with a significantly higher irradiance. The higher irradiance means the laser's deposited energy cannot spread out quickly and extremely high local temperature gradients develop. These temperature gradients are even higher in materials with low thermal diffusivity. In a very simplified view the ratio between irradiance and thermal diffusivity determines the temperature gradients seen on target.

These high temperatures cause effects like vaporization, sublimation or oxidation as well as re-radiation and the heating of nearby surfaces. Acrylite vaporizes upon exposure to these temperature gradients because it has a relatively low phase change temperature and a similarly low thermal diffusivity. Oxidation occurs in materials like carbon fiber composites because they have a combination of high phase change temperatures (carbon sublimes), and low thermal diffusivity. Intuitively, the temperature seen on target is related to the irradiance on target, and the temperatures necessary for oxidation are attained at lower irradiance levels than the temperature necessary for sublimation. Furthermore, the oxidation reaction rate is dependent on the temperature (although a minimum temperature is necessary to overcome the activation energy and begin the reaction) and this introduces nonlinearity into the governing equations making it difficult to model numerically.

The military applications of composite materials (such as drones/UAVs and small boats) are vastly increasing mostly due to their high strength to weight and stiffness to weight ratios. A composite is a heterogeneous material made of two or more discrete phases to achieve a favorable combination of their respective properties. This is in contrast to a homogeneous material like Acrylite with only one discrete phase. Additionally, Acrylite is isotropic and its material properties do not vary with direction. Conversely, heterogeneous long continuous fiber reinforced polymer composites consist of extremely strong, yet brittle, fibers in a flexible and tough polymer (in this case organic epoxy) matrix. The fibers are selected for their desirable high specific tensile strength and the matrix is selected to be tough and ductile. Two common types of fibers used are glass and carbon. They make glass fiber reinforced polymers (GFRP) and carbon fiber reinforced polymers (CFRP) respectively. CFRP has the best performance to weight ratio, but this comes at a significantly higher cost. It is therefore the predominant composite used in performance driven applications like military structures and vehicles.

Fiber reinforced polymer composite material properties can be highly dependent on the type of fiber used, its orientation and the fiber geometry. This material property dependence on direction is called anisotropy and is in contrast to typical isotropic materials that have the same properties in every direction. Unidirectional (UD) fiber reinforced polymers where the fibers are all aligned have highly directionally dependent properties. In woven fiber composites the dependency on fiber direction is somewhat decreased due to the even distribution of fibers. Especially for UD composites, the orientation of the fiber can be carefully controlled to achieve desired material properties. The strength and stiffness can be concentrated in only the direction that will be loaded, eliminating weight in other directions. This control contributes to composite materials having such high strength and stiffness to weight ratios.

Composites are significantly more difficult materials to characterize than homogenous isotropic materials like Acrylite owing to their varied constituents and fiber architectures. Additionally, laser weaponry produces more difficult-to-characterize effects than kinetic weaponry. Nonetheless, understanding and modeling the heat flow and thermal degradation of laser irradiated polymer composite materials is critical to predicting the damage mechanisms and material removal rate for these nascent directed energy weapons.

The goal of this research was to contribute to the solution of this puzzle, namely a computational model of HEL irradiation of composite materials that predicts material removal due to thermal damage. Prior to modeling complicated CFRP, a simpler polymer, carbon black loaded Acrylite, was investigated. Experimentally measured material property data was input into both models and the models were validated by measuring material recession rate post irradiation. These experimental data also served to iterate the models towards improved accuracy and higher fidelity. These models could have future applications in predicting the damage done to target materials and designing more survivable structures and would contribute to increasing the effectiveness of weapons like the Laser Weapons System (LaWS) deployed on the USS Dewey. There is potential for these weapons to neutralize targets before burning a hole in them (which is an easier response to predict). The material is weakened and structures could fail earlier, neutralizing targets sooner. If this could be predicted these weapons could be employed more effectively. Similarly, these effects could potentially be countered in US systems. However, it will require continued research into the relationship between temperature and residual strength (of which a direct correlation has been suggested) [2, 3].

The literature includes several investigations into the effect of high heating rate or high heat fluxes on composites and polymer materials. Significant studies have been conducted into the effects of heating carbon fiber composites in the context of fire safety [4]. Unfortunately, the heat flux (energy per area, analogous to irradiance) experienced during a fire is orders of magnitude lower than the irradiance a HEL generates and it is difficult to make meaningful comparisons between the two contexts. Multiple studies have been conducted into the use of high energy lasers for drilling or machining composites [5 - 8]. Pan conducted work on the prediction of the Heat Affected Zone (HAZ) in laser irradiated composites based on the computed thermal conductivity of the material [5]. Islam applied the finite element method to calculate the thermal conductivity of fiber reinforced composites [9]. McClay investigated the directional dependence of thermal conductivity in unidirectional composites [10]. Uhlman conducted similar studies into the extent of thermal damage to unidirectional composite laminates [7].

Studies have also been conducted into modeling laser induced temperature fields using both finite element and finite difference methods for various types of composites and composite structures [11-16]. Cheng developed a 3D model for heat flow in laser drilling of CFRPs [11]. Hirogaki applied the finite element technique to determine the width of the kerf created by laser drilling and machining [12]. The effect of laser wavelength on material removal was investigated by Dell'erba [13]. Garrison developed models for photothermal and photochemical modes of HEL material interaction on the microscopic level [16]. Zhou investigated the effects of dithering or rotating a laser beam approximated as a surface heat flux without material removal [14].

Previous studies have been conducted on the material removal effects of lasers on polymers and fiber reinforced polymers. Early work by Kibler attempted to quantify the residual strength of irradiated composite materials [2] and work by Nikitin attempted to elucidate the mechanisms of laser material interaction [17]. Cozzens studied the infrared ablation of polymers using a $CO_2$ laser and related ablation energy to irradiance as well as investigating the method of ablation [18]. Lloyd studied the use of ablative polymeric materials for NIR (1.06μm) high energy laser beam diagnostics and quantified the response of linearly ablating polymers including carbon black loaded Acrylite (PMMA) [19].

When applied to the near-IR case, these studies fall short in a few areas. They focus on the use of long wave infrared (LWIR) $CO_2$ lasers at 10.7 μm [5, 6, 7, 11, 12, 13, 17] or ultraviolet excimer lasers [13, 16]. Additionally, these studies typically deal with the high irradiances used in laser machining contexts [5, 6, 7, 8, 11, 12, 13] or they fail to account for material removal [14].

$CO_2$ lasers emit radiation at a wavelength 10 times longer than NIR Yb:YAG lasers (10.6 μm vs 1.07 μm). The wavelength of radiation is significant because the energy content of radiation is inversely proportional to its wavelength (Equation 1).

$$E = \frac{hc}{\lambda} \tag{1}$$

$E$ is the energy of radiation at a specific wavelength $\lambda$, $c$ is the speed of light, and $h$ is Planck's constant. Therefore, a shorter UV wavelength radiation has significantly more energy than NIR radiation, which also has more energy than LWIR radiation. These different energy levels influence whether the laser interacts with the material photochemically or photothermally. Furthermore, different media present in the atmosphere absorb different wavelengths of radiation and affect propagation through the atmosphere (discussed further later).

Earlier literature deals mostly with $CO_2$ lasers [5, 6, 7, 11, 12, 13, 17] and LWIR radiation because $CO_2$ lasers were, until recently, the most available and well developed HEL. Additionally, previous applications for directed energy weapons such as the ABL envisioned using HEL at high altitudes where propagation losses due to the atmosphere were less significant and $CO_2$ lasers were therefore viable [20].

Relatively recent developments in solid state laser technology have produced robustly designed diode pumped solid state lasers with wall plug efficiencies above 30% at decreasing costs. Furthermore, solid state laser media such as Yttrium aluminum garnet (YAG) doped with Ytterbium (Yb:YAG) or Neodymium (Nd:YAG) lase at NIR wavelengths (1.06-1.07μm). These novel lasers operating at NIR wavelengths have minimized propagation losses because they exploit absorption gaps (discussed further shortly) in the maritime atmosphere. Furthermore, novel solid state lasing media geometries like fiber lasers have increased heat transfer efficiency and opened the door to higher power solid state lasers.

In actual application, NIR radiation interacts with carbon-black loaded Acrylite via a purely photothermal mechanism. Acrylite is made of a polymer called Polymethylmethacrylate (PMMA). Carbon black loaded Acrylite is used because pure PMMA is nominally transparent to

NIR radiation. The NIR wavelength does not have sufficient energy for an individual photon to break a polymer bond in PMMA via a photochemical mechanism [19]. However, as multiple incident photons are absorbed as thermal energy (photothermally), the heat causes the polymer bonds to break and the PMMA to unzip into its gas monomer fragments upon reaching its decomposition temperature. The gaseous monomers are propelled away from the surface as a jet due to their rapid production [19]. Higher energy UV radiation produced by excimer lasers has the required energy per photon to break apart bonds in polymers photochemically. This results in much less heat transfer to the material because the energy is absorbed mainly by the polymer bonds and not aggregately as heat.

Laser machining is a short range, highly focused application of laser energy [5, 6, 7, 8, 11, 12, 13]. At close ranges typical of laser machining power on target orders of magnitude higher than those at range can be realized since atmospheric propagation losses are essentially nil. Part of the appeal of laser machining is that the beam can be focused to a very small area for detailed material removal contributing to the orders of magnitude higher irradiances and minimal thermal effects observed.

As radiation propagates through the atmosphere at increased range losses due to scattering, spreading and absorption can reduce and limit on target irradiance. Scattering occurs when photons (quantized packets of radiation) collide with particles in the atmosphere and can be quantified as either Rayleigh or Mie scattering depending on the size of the particle [20]. Spreading, also called diffraction, occurs because of the way waves (a laser beam is electromagnetic radiation and is a wave in addition to being a photon) propagate. Laser light is collimated meaning all the individual rays of light a beam is composed of are parallel. This minimizes the increase in beam size over distance compared to non-collimated light. However, a collimated laser beam originating from an aperture is subject to diffraction and its wavefront will eventually occupy a larger area than the aperture (even if it is focused). The Gaussian beam profile changes size while maintaining its shape as it propagates and the beam assumes an hourglass shape (oriented lengthwise along the axis of propagation) [20]. The Huygens-Fresnel principle describes diffraction as every point on a wavefront being a point source for a secondary spherically expanding wave, which subsequently causes constructive and destructive interference and changes the shape of the propagating wavefront [20]. The propagation distances in this research are short enough that the effects of diffraction are negligible and the beam shape can be assumed a constant size Gaussian distribution independent of distance.

Losses due to absorption are due to the energy contained in radiation being taken up by gases in the atmosphere during propagation. This phenomenon is governed by the makeup of the atmosphere the radiation propagates through. LWIR radiation can propagate well in the upper atmosphere, however water vapor in the lower atmosphere (especially the maritime domain) has a high absorbance for LWIR. NIR, notably the 1.06-1.07μm wavelength of Nd:YAG and Yb:YAG laser radiation is able to pass through a gap in the absorbance spectrum of water vapor and propagates well in the maritime domain [20].

Laser radiation propagating through the atmosphere is also subject to difficult to model nonlinear effects such as thermal blooming and optical turbulence [20]. Thermal blooming occurs when the laser energy absorbed by the atmosphere heats the air in the beam path [20]. This causes the air's refractive index (which is temperature dependent) to change causing refraction. This spreads and distorts the beam profile seen on target [20]. Optical turbulence is a similar effect, although the variations in the index of refraction are due to naturally occurring temperature variations instead of being due to the absorption of laser energy [20].

These propagation effects depend to a certain extent upon the irradiance of the laser beam and act to limit the total power that can be put on a target at range. Furthermore, changing the wavelengths and irradiance level produces different results when irradiating complex materials like fiber reinforced polymers (composites) or even simple unreinforced polymer materials. The Department of Defense is in need of more research into the effects of potential on target irradiances on polymers and composites [18, 21, 22]. An accurate model of the heat transfer and the resulting temperature field in a composite structure could be used to predict the thermal degradation of composite structures and moreover the loss of strength and function for the structure. This could be used to better employ HEL as weapons and defeat emerging UAV and small boat threats.

## TARGET MATERIALS:

The potential targets of an HEL weapon (C-UAV, C-RAM, BMD and small boats) are made of materials that include metals, plastics and composites. A composite is a material made of two or more discrete materials that yields a favorable combination of their respective properties as discussed earlier. CFRP are widely used in UAVs and other high performance applications.

Fiber reinforced composites are much more complicated to analyze or model because they are anisotropic and nonhomogeneous materials, meaning that their material properties vary with direction and position. For an isotropic and homogenous material, material constants can be represented by single scalars, in a non-isotropic material matrices are required to fully describe the material properties. Bulk properties that are not directionally dependent such as density or heat capacity can be approximated with a rule of mixtures, a volume weighted average of the constituent phase properties, and expressed as scalars.

Two basic types of fiber architecture are plain woven and unidirectional. Unidirectional (UD) composites where the fibers are aligned are much more anisotropic [9]. Woven composites are less anisotropic and have more planes of symmetry; motivation for treating woven composites as transversely isotropic follows later.

The properties of a composite material are strongly related to the type of fiber and the fiber architecture used in the model [23]. The overall properties of the composite also depend on the type of matrix and the ratio of matrix to fiber [23]. Micromechanics is the study of composite or heterogeneous materials on the scale of the constituent phases. In the case of fiber reinforced polymer composites micromechanics considers representative elements on the scale of the fiber diameter [23]. Analytical micromechanics models are sometimes applied to the mechanical properties of UD composites, while the complicated fiber geometry of woven composites often precludes analytical solutions and requires the use of numerical micromechanics models. A development of an analytical micromechanics model for thermal conductivity in UD composites follows. This was later extrapolated to apply to woven composites using simplifying assumptions.

When approached from a micromechanics perspective, the thermal conductivity of a composite lamina can be approximated with an electric circuit analogy [24]. The electric circuit analogy is a way to quantify heat transfer through dissimilar materials, and in this case is applied to a representative volume element. The thermal conductivity of a UD composite lamina in the parallel and perpendicular (to the fiber) directions and the respective circuit analogy are shown in Figure 1. Transversely isotropic materials are symmetric around an axis normal to a plane of symmetry. In UD composite lamina, this plane of symmetry exists normal to the fiber direction. The symmetry means the material properties of the UD composite are independent of direction in this plane. The fiber direction is denoted as subscript 1, and the in-plane perpendicular and through thickness perpendicular directions denoted as subscripts 2 and 3.

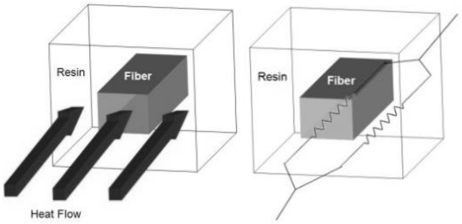

**Figure 1a** Parallel circuit or flux parallel to UD fiber direction [10].

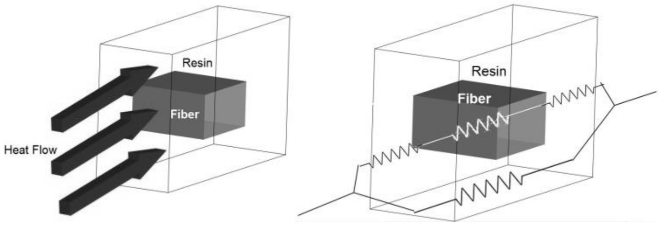

**Figure 1b** Series circuit or flux perpendicular to UD fiber direction [10].

The thermal conductivity in the fiber direction (subscript 1) is predicted by Equation 2 derived from the representative volume element geometry shown in Figure 1a using a parallel circuit analogy [23].

$$k_1 = V_{fiber}k_{fiber} + V_{matrix}k_{matrix} \tag{2}$$

$V_{fiber}$ and $V_{matrix}$ are the volume fractions of fiber and matrix respectively. $k_1$ is the thermal conductivity in the fiber direction, while $k_{fiber}$ and $k_{matrix}$ are the thermal conductivities of the fiber and matrix phases respectively. The transverse thermal conductivity in the plane of symmetry is derived as a series circuit (Equation 3) [10].

$$k_2 = k_m\left(1-\sqrt{V_f}\right)+\frac{k_f k_m \sqrt{V_f}}{\sqrt{V_f}\,k_m + k_f\left(1-\sqrt{V_f}\right)} \tag{3}$$

A laminate is made of multiple lamina, sometimes with different fiber orientations. The in-plane thermal conductivity of multiaxial laminates is typically attained through the use of a summation method, where the global thermal conductivities of the laminate (denoted by uppercase K) are calculated based on summations of the thermal conductivity and thickness for each lamina [10, 25]. $K_1$ is the global thermal conductivity in the fiber direction for a composite laminate composed of lamina of thickness $\delta$, $K_2$ is in the transverse direction and $K_3$ is in the through thickness direction [25]. $k_1$ is the thermal conductivity of each ply in the 1-direction and $\delta_i$ is the ply thickness of each ply, similarly for $k_2$ and $k_3$ in Equations 4, 5 and 6.

$$K_1 = \frac{\sum_{i=1}^{N}(k_1\delta)_i}{\sum_{i=1}^{N}\delta_i} \tag{4}$$

$$K_2 = \frac{\sum_{i=1}^{N}(k_2\delta)_i}{\sum_{i=1}^{N}\delta_i} \tag{5}$$

$$K_3 = \frac{\sum_{i=1}^{N}\delta_i}{\sum_{i=1}^{N}(\frac{\delta_i}{k_3})} \tag{6}$$

Pan determined that the shape (usually elliptical) of an HAZ in a UD composite lamina can be related to the parallel and perpendicular thermal conductivities with Equation 7 [5]:

$$k_2 = \left(\frac{r_2}{r_1}\right)^2 k_1 \tag{7}$$

$k_1$ and $k_2$ are the thermal conductivities parallel and perpendicular to the fiber direction, and $r_1$ and $r_2$ are radii of an elliptical HAZ in the parallel and perpendicular to fiber directions. In UD composites the HAZ is elliptical because of the higher thermal conductivity in the fiber direction. Additionally, if the HAZ is circular, as observed in woven composites, and the quotient $\frac{r_2}{r_1}$ goes to unity, the thermal conductivity in the different directions must necessarily be equal.

Therefore for the woven fiber composites of interest in this project, the thermal conductivity can be treated as transversely isotropic with the plane of symmetry being the same plane as the lamina. This means that there is not a preferential in-plane thermal conductivity direction, eg. $k_1 = k_2 \ \forall \ \theta$ since the high thermal conductivity fibers are equally distributed perpendicular to each other. Additionally if all layers of the textile composite laminate are the same weave and the same thickness the global thermal conductivity $K_1 = K_2 = k_1$. Figure 2 shows a circular HAZ formed as the result of HEL irradiation that provides evidence of in-plane isotropic behavior. The teardrop shaped char on the GFRP sample in Figure 2 is due to a vacuum applied to remove smoke and debris during irradiation.

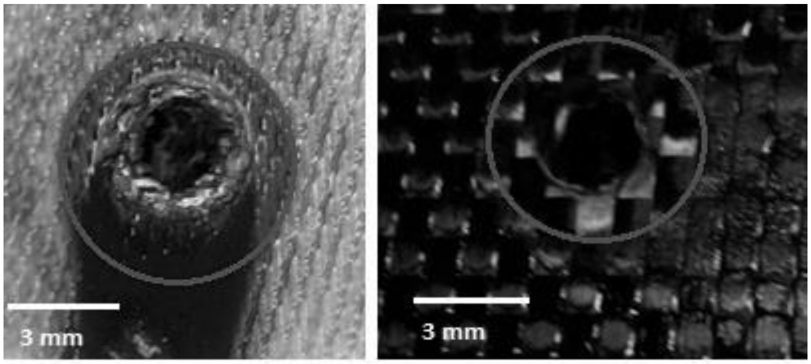

**Figure 2:** Left: Glass Fiber/Epoxy with Nomex honeycomb core sandwich structure irradiated by HEL. Right: Carbon Fiber/Epoxy Nomex honeycomb core irradiated by HEL.

A heat flux in a woven composite in the through thickness direction will pass through layers of fiber and matrix similar to the perpendicular direction in UD composites and can be approximated by $k_2$ [25]. The global through thickness conductivity $K_3$ is the same as $k_2$ because the thickness of each ply is the same, and the through thickness conductivity of each ply is also the same, therefore the thickness weighted average, $K_3$ is approximately equal to $k_2$. Because only woven fiber composite laminates were used this simplifies the inputs for the model to two values: an in-plane thermal conductivity, $k_r$, $(k_1 = k_r)$ and a through-thickness conductivity, $k_z$, $(K_3 = k_2 = k_z)$ and saves computational expense.

More accurate means of thermal conductivity analysis are available using the finite element method, and the thermal conductivity of a composite can be directly measured using the laser flash method or a Mathis probe [5,7]. A first approximation for this project was made using the aforementioned equations, and later laser flash method (LFM) measurements were made and incorporated into the model.

Composites are employed in many applications as sandwich structures. Sandwiching a lightweight closed or open cell core between two composite laminates creates a lightweight structure that is extremely strong in bending. In bending the core provides the structure lateral support and spacing, and the skins carry the tensile or compressive flexural stresses. In a wing structure exposed to bending, the skyward face experiences compressive stress while the landward face experiences tensile stress. Fiber reinforced composites are naturally weaker in compression because the fibers are susceptible to micro-buckling because of their high slenderness ratio. This proclivity towards buckling is even more pronounced in woven composites because the weaving process has crimped and unstraightened the fibers, further aggravating their predisposition for buckling. The matrix provides the majority of the lateral support preventing buckling. When a wing is irradiated from the ground the matrix in the skyward face of sandwich structure is burnt away [26]. This makes the structure even more susceptible to compressive failure and can contribute to the failure of a structure well before a large amount of carbon fibers are removed by oxidation.

## MATERIAL PROPERTY MEASUREMENTS:

The numerical model developed in this research requires measured material property values for its inputs. These values were measured via differential scanning calorimeter (DSC), fiber optic reflectance spectroscopy (FORS) and laser flash method (LFM). DSC provided the thermal properties of specific heat and latent heats as well as the phase transition temperatures. These properties determine how a material's temperature responds to heating. FORS was used to determine the hemispherical spectral absorbance at 1.07µm, which measures how much of the incident laser energy is absorbed by the material. LFM was conducted to measure the through thickness and in-plane thermal conductivities of the composite material. The thermal conductivity of isotropic materials like Acrylite GP does not vary with direction and this value was taken from the material data sheet.

### Thermal Analysis

DSC works by heating a sample and a reference pan at a constant heating rate (the time derivative of temperature $\frac{\mathrm{dT}}{\mathrm{dt}}$ measured in °C/s is held constant) and precisely measuring the difference in specific heat flow ($\frac{\mathrm{dH}}{\mathrm{dt}}$ in W/g) between the sample and a reference sample. From the DSC data an effective specific heat that is the sum of the specific heat $C_p$ (in J/g°C) and specific heat of thermal events, $C_{Thermal\ Events}$ can be calculated (Equation 8). The specific heat is a measure of how much energy it takes to raise a mass of material's temperature. The thermal events include latent heats of vaporization, crosslinking, and oxidation reactions that produce or consume heat. The latent heat of thermal events is determined by integrating the specific heat of thermal event over the temperature interval over which the event occurs (Equation 9).

$$\mathrm{C_{effective}} = \mathrm{C_p} + \mathrm{C_{thermal\ event}} = \frac{\frac{\mathrm{dH}}{\mathrm{dt}}}{\frac{\mathrm{dT}}{\mathrm{dt}}} \tag{8}$$

$$\Delta H_{thermal\ event} = \int_{T_{start}}^{T_{stop}} (C_{thermal\ event})dT \tag{9}$$

DSC was performed on carbon black loaded Acrylite at a 10°C/min heating rate in an Aluminum pan in a nitrogen atmosphere from room temperature to 600 °C using a TA instruments DSC-2010. Care was taken to match the weight of the sample pan to the reference pan. Ideally the test would be run under air to match the oxidizing environment HEL irradiated materials are subject to, but the DSC used was only configured to run on nitrogen. APPENDIX A provides additional details on the procedure used.

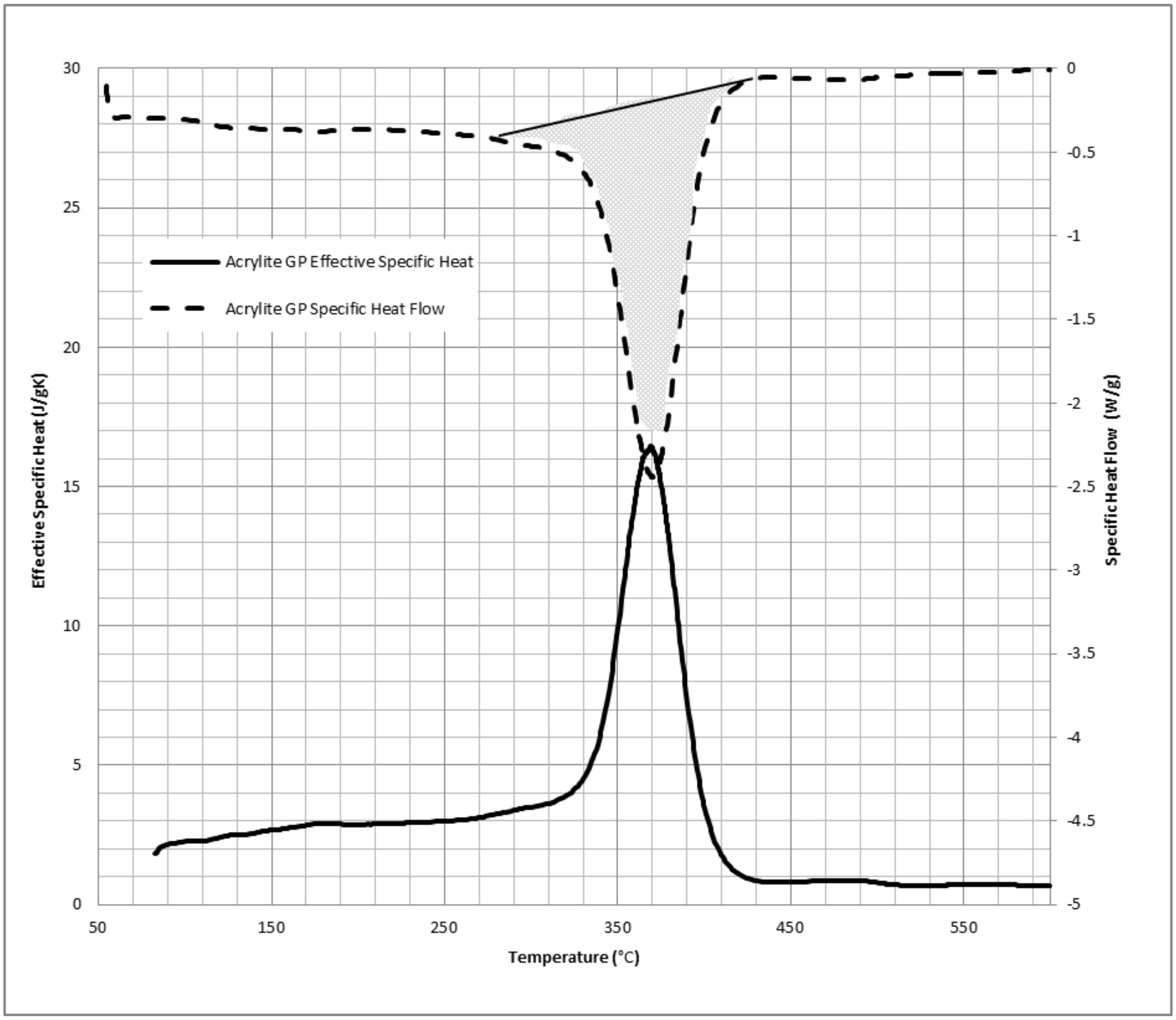

**Figure 3:** DSC of carbon black loaded Acrylite. Specific heat flow is plotted endotherm down.

Figure 3 shows the average of 3 DSC runs on carbon black loaded Acrylite GP. At approximately 280°C the endothermic phase change from liquid to vapor for Acrylite GP occurs. The endotherm is the latent heat of vaporization that manifests itself in the model as an increase in effective specific heat. The latent heat of the transition from solid to liquid was negligible and this transition was neglected. The latent heat of vaporization is the shaded area under the peak in Figure 3, and can be calculated by placing a secant line from the onset and offset points of the transition and integrating. The placement of this secant line is somewhat subjective, and it was important that the same person place the secant lines to minimize variability introduced in the data. The local maxima and minima of the derivative of the specific heat flow were used to place the secant line. The model was insensitive to variation in inputs derived from DSC data therefore the model was insensitive to secant line placement.

Additional types of carbon black loaded Acrylite were also investigated via DSC and the data from these trials is presented in APPENDIX B.

DSC was conducted on CFRP following the same procedure in APPENDIX A. A 2.4mm thick 20 ply carbon fiber/epoxy laminate was constructed for testing using Cytec 5215 modified epoxy resin prepreg with a 1K tow in plain weave architecture. A 16” x 16” panel was made by first debulking three sets of 6 plies under vacuum for 30 minutes before curing into an 18 ply (~2.4mm thick when cured) laminate at 200 °C for 3 hours under vacuum.

CFRP exhibits four thermal events or physical transitions. Each of these transitions was treated analogously to the single phase change in PMMA and is marked by a shaded area in Figure 4. The specific heat flow and subsequent calculated effective specific heat of CFRP are shown in Figure 4. The first three thermal events were captured by the DSC (Figure 4). The first event was theorized to be crosslinking, due to a relatively low latent heat, the temperature range over which it occurs and knowledge of the epoxy used in the CFRP. The second event at about 250°C was epoxy burn off. The third event at 350°C is associated with material degradation and removal of residue from the epoxy. The fourth thermal event is the removal of the carbon fiber by oxidation at temperatures above the capability of the DSC used and is not shown on the following graph. The rate of oxidation is temperature dependent, and the amount of time experienced at temperature during irradiation is on the order of seconds to minutes, so the temperature (which is related to irradiance) must be high enough so that oxidation occurs at a rapid rate otherwise material removal will not be noticeable. Oxidation does not occur to an appreciable amount during the timescales of irradiation in this paper unless surface temperatures exceed approximately 800-900 °C [29].

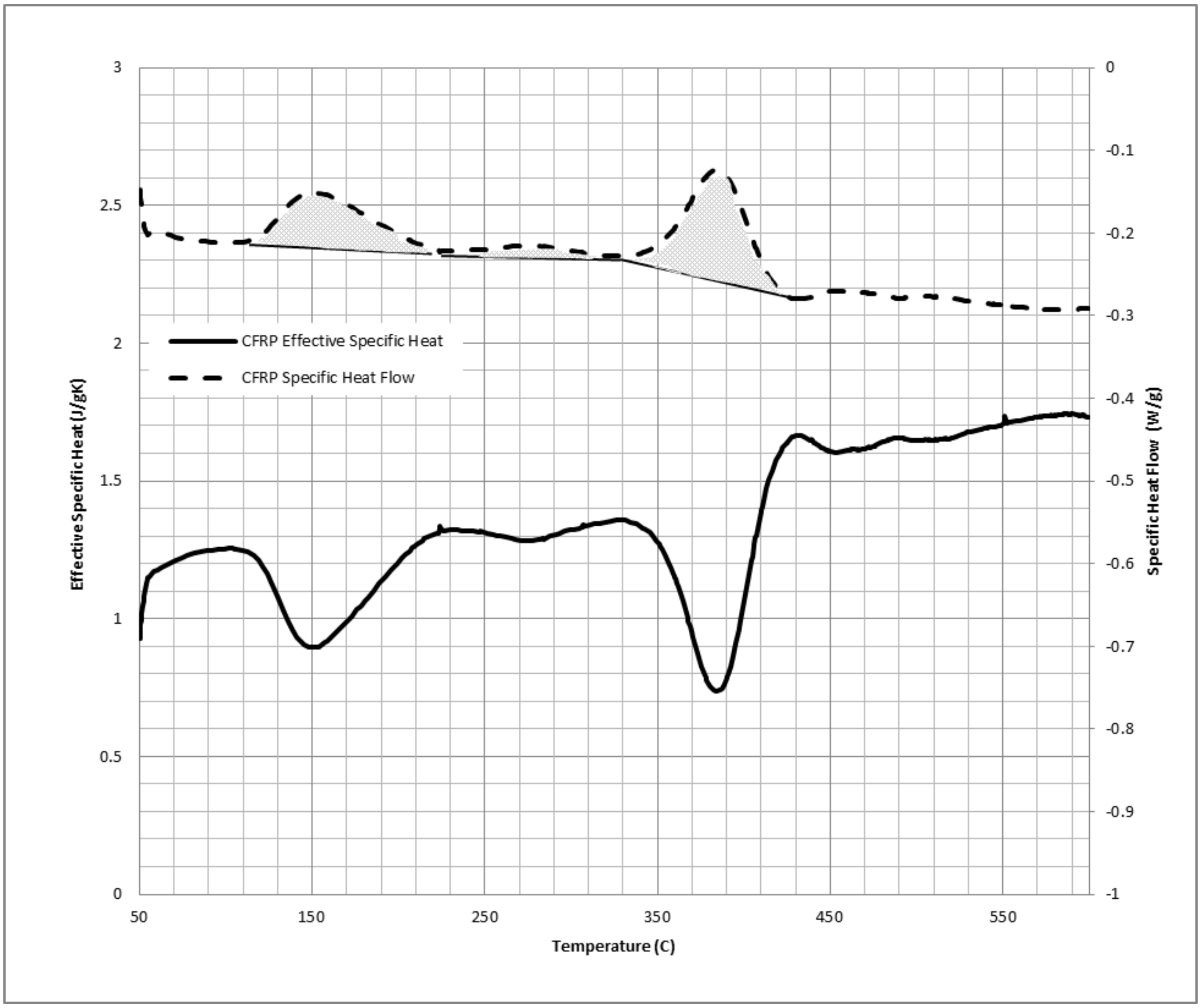

**Figure 4:** Average of three DSC scans of CFRP.

## Absorptivity Analysis

NIR spectroscopy was performed by Dr. Suzanne Lomax at the National Gallery of Art on the carbon black loaded Acrylite sample using a FieldSpec-3 fiber optic reflectance spectroscopy (FORS) from ASD Inc. FORS determines the absorptivity at the near infrared wavelength of the electromagnetic radiation being studied. There are many variations of spectrophotometry, however the basic principle is to place the sample against an integrating sphere and illuminate it with a monochromatic light. A broadband light is usually passed through an interferometer to create a monochromatic light at an adjustable wavelength. The light is passed through the integrating sphere and onto the sample surface. The light reflected specularly and diffusely from the sample is then captured within the integrating sphere, and the total power inside of it is measured with a power meter. When compared to a reference sample of close to 100% reflectivity, the relative reflectivity of the sample can be measured spectrally. FORS takes these measurements through fiber optics so it is possible to measure a sample without placing it inside a machine. Further details about the FORS are provided in APPENDIX E.

Normally absorbance is an exponential decay of transmitted power through a material. If this rate of absorbance is extremely high, effectively all the energy is absorbed at an infinitesimal depth from the surface. An assumption made was that the sample was nearly opaque and that no energy was transmitted through it in the near infrared wavelength. Therefore the absorbance could be calculated directly from the reflectance measured. This assumption affects whether the model invokes volumetric heating or surface heating and must be further investigated. Furthermore, it was not possible to measure these properties at the significantly elevated temperatures experienced during HEL irradiation so temperature independence was assumed. With the assumptions made, the absorptivity (fraction of incident energy absorbed by the material) can be calculated with Equation 10:

$$\rho_{1.07} + \alpha_{1.07} + \tau_{1.07} = 1 \text{ with } \tau_{1.07} = 0 \tag{10}$$

$\tau_{1.07}$ is the spectral transmissivity (fraction of energy transmitted through the incident plane at 1.07μm wavelength), which is equal to zero for an opaque material, $\alpha_{1.07}$ is the hemispherical spectral absorptivity, and $\rho_{1.07}$ is the hemispherical spectral reflectivity (fraction of incident energy reflected at wavelength).

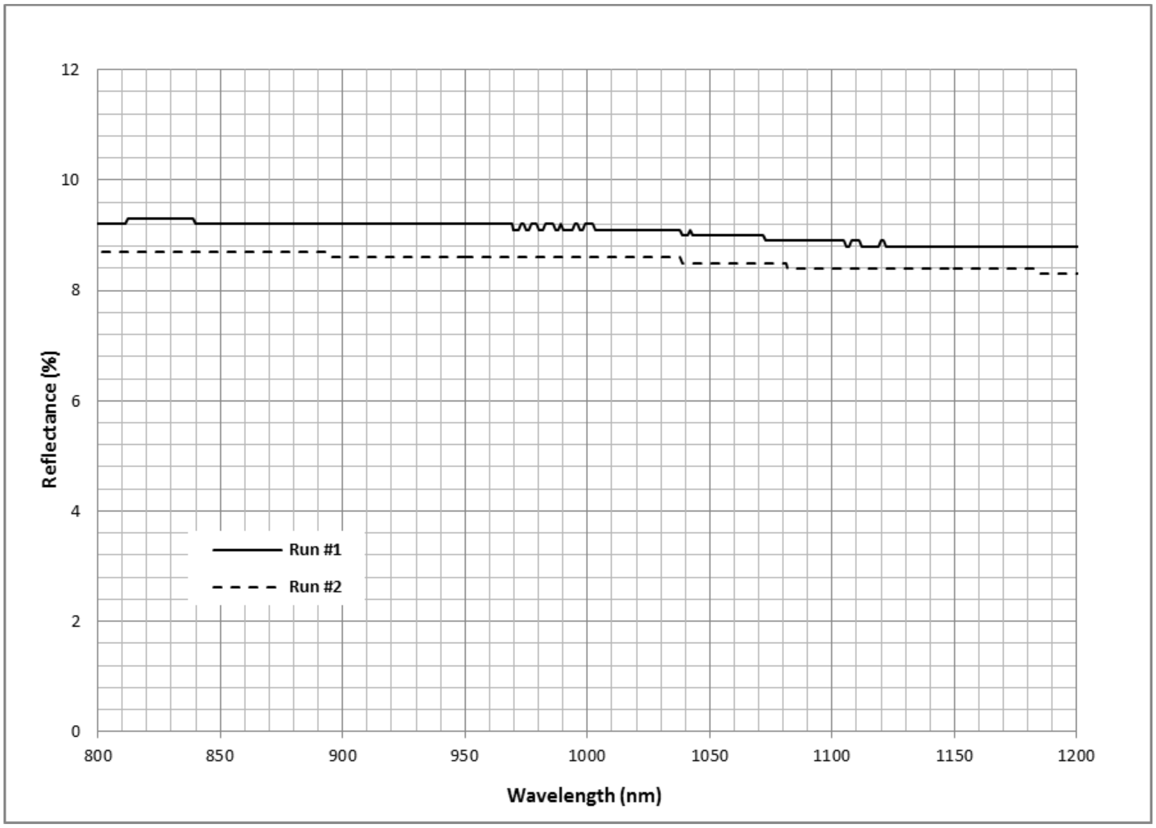

**Figure 5:** FORS data for carbon black loaded Acrylite.

The reflectivity of the carbon black loaded Acrylite was characterized by the FORS (Figure 5). The spectral sampling rate was 1.4nm from 350-1000nm and 2.0 nm from 1000-2500nm with an integration time of 100msec and 64 spectra averaging. The reflectance is plotted on the vertical axis and is between 8% and 10% at 1070nm. Multiple experiments performed at USNA, as well the data from Dr. Lomax shown above, established that the reflectivity was approximately 9% and by the above assumptions the surface absorptivity was 91%. CFRP absorbance was measured at USNA to be ~91% as well (APPENDIX E). The similarity is most likely due to a minimal amount of surface reflectivity in both samples.

## Thermal Conductivity

The thermal conductivity of isotropic Acrylite is easily obtained from its material data sheet. For the CFRP a first approximation to the thermal conductivities were calculated using rule of mixtures and thermal circuit analogies. The calculated values were later replaced with the measured values from LFM and density measurement. As previously described the thermal conductivity of CFRP depends on the fiber content and the fiber orientation and as such must be measured in both the through thickness and radial (in-plane) directions. Dr Jin Park at the High Performance Materials Institute of Florida State University performed LFM using a Netzsch LFA 457 laser flash diffusivity machine following ASTM E1461 guidelines. More details are in APPENDIX D.

The laser flash method measures thermal diffusivity, $\alpha$, by heating one side of a sample with a pulse of laser energy, and then measuring the thermal response on the opposite side of the sample.

$$\alpha = \frac{k}{\rho C_p} \tag{11}$$

In Equation 11 the thermal conductivity $k$ can be calculated from the measured thermal diffusivity $\alpha$ if the density $\rho$ and specific heat $C_p$ are known. The density is known from the material data sheet or experiment, and the specific heat is measured from the DSC as discussed above. The data are shown below in Figure 6.

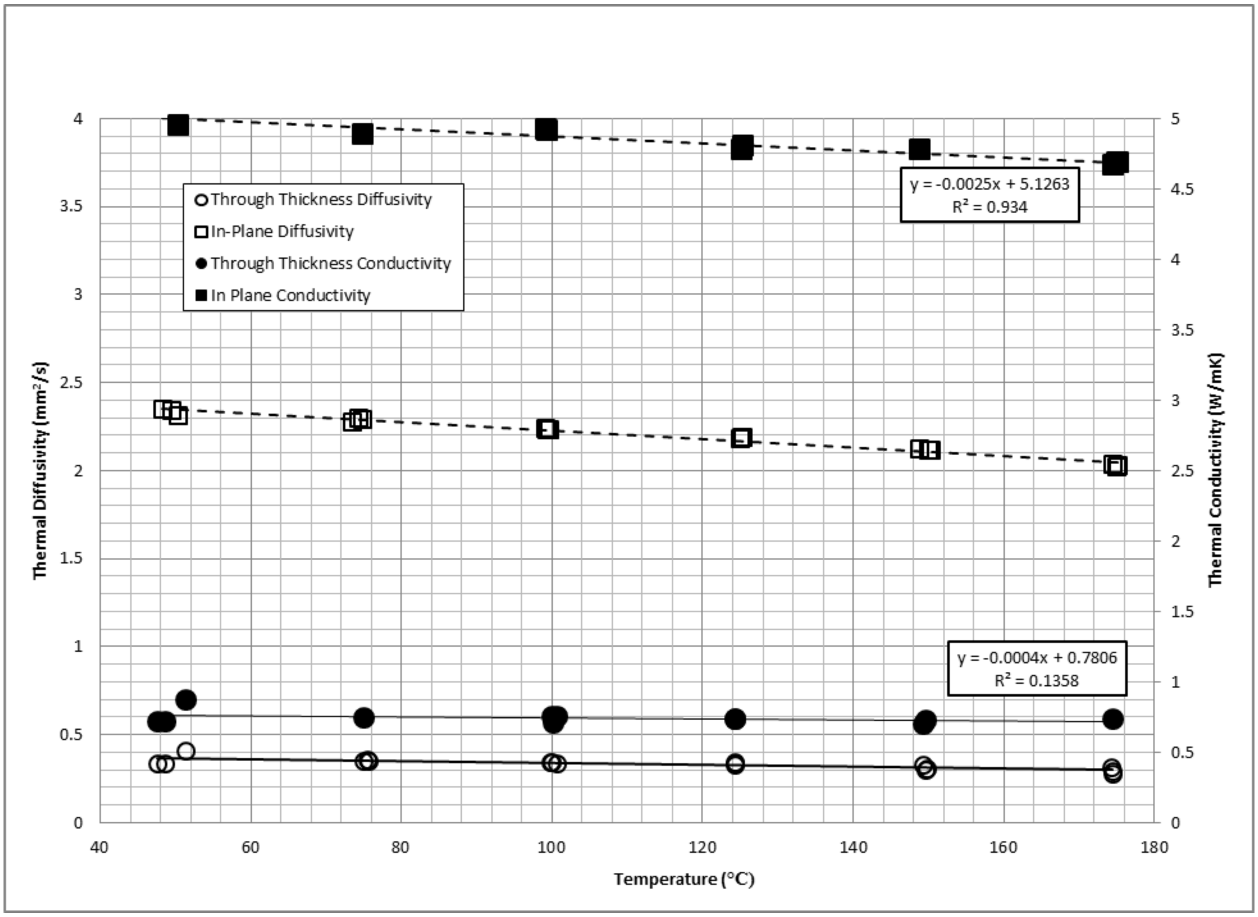

**Figure 6:** The thermal diffusivity measured by the LFM and the thermal conductivity calculated from it.

The through thickness thermal conductivity is lower, and this is explained by the perpendicular thermal circuit in Equation 3. The in-plane thermal conductivity is higher, this can be explained by the parallel thermal circuit in Equation 2. The through thickness and in-plane thermal conductivities calculated from the LFM were assumed to be temperature independent because of a lack of high temperature measurements. Values of 5.5W/mK and 1 W/mk for in-plane and through thickness thermal conductivity were used as inputs to the CFRP model.

# NUMERICAL MODEL

## Heat Transfer Theory

The heat diffusion equation for an isotropic and homogeneous material is derived from Fourier's law which states that the rate of heat transfer through a material is proportional to the gradient of temperature and the conservation of energy principle applied to a control volume [31].

$$\frac{\partial T}{\partial t} = \alpha\, \nabla^2 T = \alpha \left( \frac{\partial^2 T}{\partial x^2} + \frac{\partial^2 T}{\partial y^2} + \frac{\partial^2 T}{\partial z^2} \right) \;\; where \;\; \alpha = \frac{k}{\rho C_p} \tag{12}$$

The time derivative of temperature ($\frac{\partial T}{\partial t}$) is proportional to the Laplacian ($\nabla^2$) of temperature (T) (Equation 12). The thermal diffusivity of a material ($\alpha$) is equal to the quotient of the thermal conductivity ($k$), density ($\rho$) and specific heat ($C_p$). This equation applies only to materials with $k$ , $\rho$ , $C_p$ that are independent of direction (isotropic), independent of position (homogenous) and independent of temperature.

To solve a partial differential equation like the one presented above, boundary conditions (to satisfy the spatial derivatives) and initial conditions (to satisfy the time derivatives) are necessary [31]. The initial condition is normally the initial temperature of the domain. The boundary conditions can be one of three types. A Dirichlet boundary condition is a prescribed temperature [31]. A Neumann boundary condition is a prescribed normal derivative or flux ($\frac{\partial T}{\partial x}$, $\frac{\partial T}{\partial y}$, or $\frac{\partial T}{\partial z}$) [31]. Neumann boundary conditions are used to account for heat transfer modes on the surface (convection, radiation, etc) by setting the equation for the external heat transfer equal to the normal derivative or flux. Mixed or Robin boundary conditions also exist.

To demonstrate how heat conduction equations are solved analytically, a one dimensional problem for which a simple analytical solution exists is considered: [31].

$$\frac{\partial T}{\partial t} = \alpha \frac{\partial^2 T}{\partial x^2} \tag{13}$$

In Equation 13 the Laplacian has been simplified to the second partial derivative of *T* with respect to *x* by considering a one dimensional domain. The solution to this equation uses a separation of variables and Fourier series technique from [31]. The solution to the equation is assumed to be a product of spatial (*F(x)*) and temporal (*G(t)*) functions.

$$T(x,t) = F(x)G(t) \tag{14}$$

When the above equation is substituted back into the heat diffusion equation it can be separated into two ordinary differential equations as follows (Equations 15-17):

$$\frac{\partial T}{\partial t} = \frac{\partial}{\partial t}(FG) = F\frac{dG}{dt} \tag{15}$$

$$\alpha\frac{\partial^2 T}{\partial x^2} = \alpha\frac{\partial^2}{\partial x^2}(FG) = \alpha\frac{d^2 F}{dx^2}G \tag{16}$$

$$\frac{\partial T}{\partial t} = \alpha\frac{\partial^2 T}{\partial x^2} \;\; \rightarrow \;\; F\frac{dG}{dt} = \alpha\frac{d^2 F}{dx^2}G \tag{17}$$

This equality of two ordinary differential equations can then be reordered into Equation 18:

$$\frac{\frac{dG}{dt}}{\alpha G} = \frac{\frac{d^2F}{dx^2}}{F} = -p^2 \tag{18}$$

Because the two sides of Equation 18 depend on different variables the only way for the two to be equal and maintain the independence of those two variables ($t$ , $x$) is to equate them to a constant (-$p^2 = \alpha$). The two equations can now be separated into individual homogenous ordinary differential equations and solved.

$$\frac{d^2F}{dx^2} + p^2F = 0 \quad and \quad \frac{dG}{dt} + c^2p^2G = 0 \tag{19}$$

When boundary conditions are applied the Eigenfunctions of these two equations are Equation 20:

$$F_n(x) = \sin\left(\frac{n\pi x}{L}\right) \; and \; G_n(t) = B_n e^{-\lambda_n^2 t} \quad \lambda_n = \frac{cn\pi}{L} \tag{20}$$

Where $n$ is an integer (1,2,3…) and $L$ is the length of the 1D domain of this equation. Since $T$ was assumed to be of the form $T(x,t) = F(x)G(t)$ the solutions to $T$ must be the product of the Eigenfunctions $F_n(x)$ and $G_n(t)$ (Equation 21).

$$T_n(x,t) = \sin\left(\frac{n\pi x}{L}\right) B_n e^{-\lambda_n^2 t} \tag{21}$$

The full solution $T(x,t)$ (Equation 22) must be the sum of the individual solutions $T_n(x,t)$.

$$T(x,t) = \sum_{n=1}^{\infty} u_n(x,t) = \sum_{n=1}^{\infty} \sin\left(\frac{n\pi x}{L}\right) B_n e^{-\lambda_n^2 t} \tag{22}$$

The coefficients $B_n$ can be evaluated by recognizing that $T(x,t)$ is of the form of a Fourier sine series and using the initial condition $T(x,0)$ (Equation 23).

$$B_n = \frac{2}{L}\int_0^L u(x,0) \sin\left(\frac{n\pi x}{L}\right) dx \tag{23}$$

Substituting back in, the entire solution to $T(x,t)$ is (Equation 24):

$$T(x,t) = \sum_{n=1}^{\infty} \sin\left(\frac{n\pi x}{L}\right) \left(\frac{2}{L}\int_0^L T(x,0) \sin\left(\frac{n\pi x}{L}\right) dx\right) e^{-\lambda_n^2 t} \tag{24}$$

Since solutions with higher values of $n$ rapidly become negligible it is possible to approximate the solution (with increasingly high accuracy) by using a $j^{th}$ partial sum in Equation 25.

$$T(x,t) = \sum_{n=1}^{j} \sin\left(\frac{n\pi x}{L}\right) \left(\frac{2}{L}\int_0^L T(x,0) \sin\left(\frac{n\pi x}{L}\right) dx\right) e^{-\lambda_n^2 t} \tag{25}$$

Thus a closed form analytical approximation to a 1D heat transfer equation is possible [31]. This is not an applicable solution to the problem treated in this paper for several reasons. Heat transfer for HEL irradiated composites is a three dimensional problem shown in Equation 26 (although this is later simplified to two dimensions by modeling the problem axisymmetrically in our approach).

$$\frac{\partial T}{\partial t} = \alpha\left(\frac{\partial^2 T}{\partial x^2} + \frac{\partial^2 T}{\partial y^2} + \frac{\partial^2 T}{\partial z^2}\right) \ \ where \ \ \alpha = \frac{k}{\rho C_p} \tag{26}$$

Because composite materials are anisotropic and heterogeneous the thermal conductivity changes from a scalar value to a second order symmetric tensor (Equation 27):

$$\boldsymbol{k} = \begin{bmatrix} k_{xx} & k_{xy} & k_{xz} \\ k_{xy} & k_{yy} & k_{yz} \\ k_{xz} & k_{yz} & k_{zz} \end{bmatrix} \tag{27}$$

Additionally, $k$ , $\rho$ , $C_p$ are now temperature dependent functions, making $\alpha$ a function of temperature. Because $k, \rho, and\ C_p$ are now functions of temperature and position they cannot be combined in the heat diffusion equation into a single term $\alpha$. Therefore, the three dimensional heat equation in a fully anisotropic, heterogeneous, material with temperature dependent thermal conductivity, density and specific heat is (Equation 28):

$$\rho(T)C_p(T)\frac{\partial T}{\partial t} = \nabla\cdot(\boldsymbol{k}(T)\nabla T) \tag{28}$$

The above equation is a second order nonlinear partial differential equation that is essentially unsolvable analytically. The high degree of nonlinearity introduced by temperature dependent material properties causes the difficulty in solving it. Therefore, the heat transfer problem was approached numerically using COMSOL Multiphysics, a finite element program.

Finite element analysis involves creating a mesh or discretization of the domain being modeled. This splits up the domain into a collection of small elements or subdomains. The governing heat transfer equations are applied to each of these small elements. The individual equations are then combined into a system of equations and solved by computer. The complex differential equations for heat transfer can then be solved by complex numerical methods beyond the scope of this work that are performed by COMSOL.

## Material Removal Method

Because of the high temperatures experienced by laser irradiated materials, significant amounts of material are removed by vaporization, oxidation, or ablation. Failure to incorporate these effects in a heat transfer model of laser irradiated materials will lead to errors in the form of unrealistically high surface temperatures [14]. There are two approaches to modeling material removal: either have the model actually remove an element that has been vaporized and then create a new mesh or have the model retain the vaporized element and cause it to numerically act as if it has been removed.

Removing and remeshing around those elements is computationally expensive. Remeshing in between each time step will significantly slow down a model and requires more computing power. Furthermore, this creates complex topographies (a hole shape instead of a flat surface) that boundary conditions must be applied to. These complex topographies also slow down the model and increase the computing power required [11-16]. Additionally they introduce a potential place for the model to fail.

Conversely, a model can retain elements that have been vaporized by numerically forcing those elements to act as if they do not exist. This is the approach used in this research and was based on the idea of modeling phase change. For example, picture an ice cube warming. Now apply a mesh to the ice cube splitting it up into equally sized finite elements. Applying the heat diffusion equation through the volume of the ice cube allows the calculation of how heat will flow through its volume. Boundary conditions are applied to the surfaces of the ice cube to develop a complete set of equations (discussed later). It is then possible to calculate the temperature at any time and place in the ice. However, if the temperature field had elements in the ice cube above 0°C, the results would be illogical because ice melts at 0°C. When ice reaches its melting point, its temperature stops rising (more complicated materials have temperature ranges over which phase changes occur, this will be discussed in more depth later), and thermal energy that would normally increase its temperature according to its specific heat is now applied to overcoming the latent heat of phase change. Once enough energy has been added the whole of the material has changed phase. With this change occurs associated changes in material properties i.e. the density of water is greater than that of ice. By changing the material properties after the phase change to values that make the element thermally act as if it did not exist, the element is effectively removed from the model.

To simulate material removal, a numerical technique of varying the material properties as described above and presented in [26] was used. To accomplish this, three forcing functions are needed for each phase change or thermal event experienced by the material. Acrylite was modeled as subliming, and thus is one phase change requiring three forcing functions. This assumption was made based on observations from the DSC. The CFRP model required four thermal events to fully capture the behavior measured by DSC and its forcing functions are presented following the Acrylite functions.

Smoothed Heaviside functions and their derivatives were used to actuate the material properties and mathematically achieve the material removal mechanism. By definition, a Heaviside function changes from 0 to 1 instantaneously (and discontinuously). Conversely, a smoothed Heaviside function changes over an interval with finite width (Figure 7). The Heaviside functions used in the model needed to be smoothed because the discontinuity of a regular Heaviside function caused convergence errors when the COMSOL software attempted to solve the model.

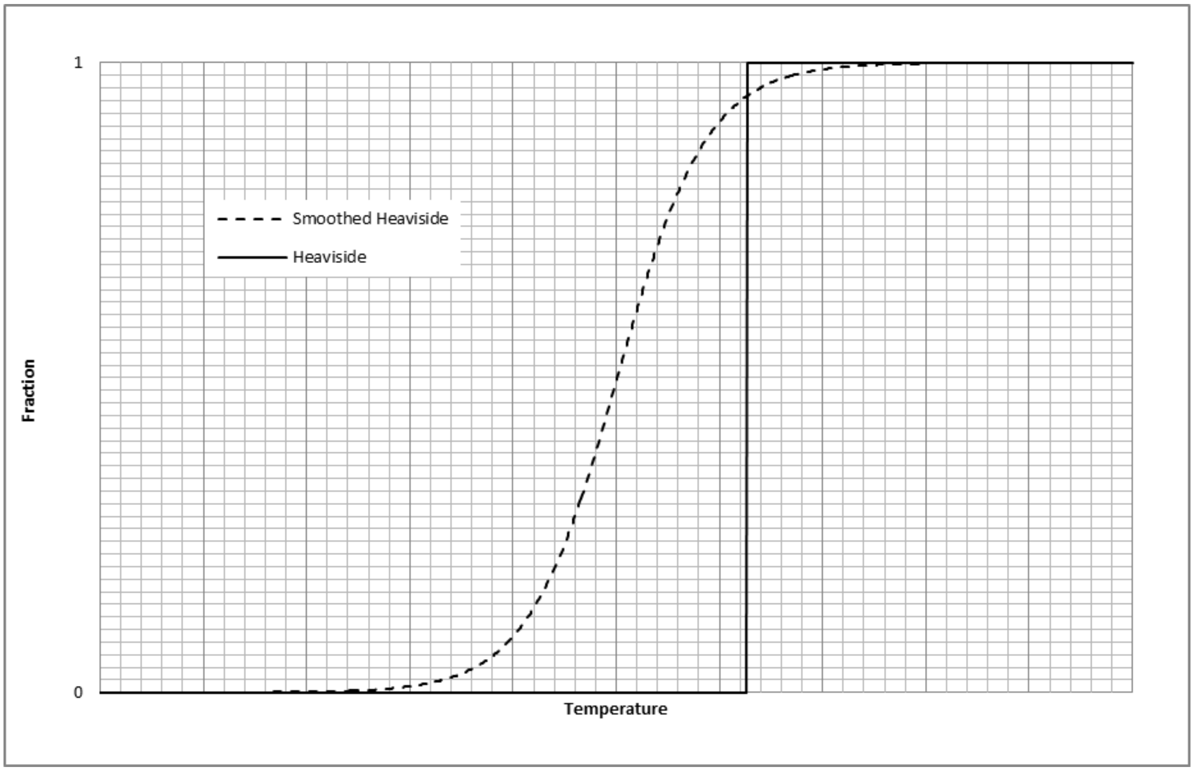

**Figure 7**: Heaviside and smoothed Heaviside functions.

The derivative of a Heaviside function is a Dirac Delta function, or a widthless pulse with area 1. Since the Dirac Delta function has infinitesimal width, the height of the function must be infinite at the transition (Figure 8). (The Dirac Delta function is technically a single line but it is shown here with finite width for illustrative purposes.) This physically makes sense because for the Heaviside function to transition from zero to unity over a widthless interval, the slope must be infinite. Conversely, the derivative of a smoothed Heaviside is still a pulse with area 1, but it has a finite width: the width of the smoothing interval.

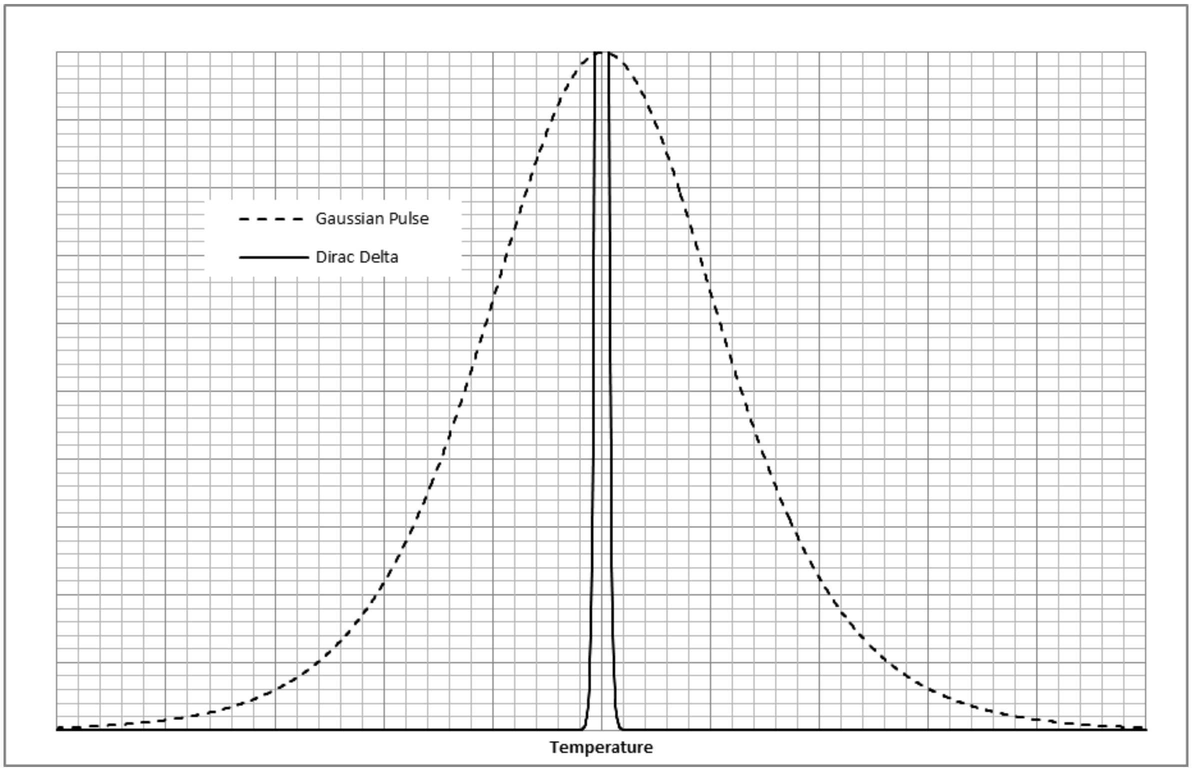

**Figure 8:** Dirac delta function and Gaussian pulse functions. Dirac delta function given finite width for illustrative purposes.

The integrals of both the Dirac Delta and the Gaussian pulse functions are equal to unity. Therefore multiplying a Dirac delta or Gaussian pulse function by a scalar gives a product that has a total area equal to the magnitude of the scalar, however that magnitude is distributed across the interval of the function.

The smoothed Heaviside and derivative functions used in the COMSOL model follow (Figure 9).

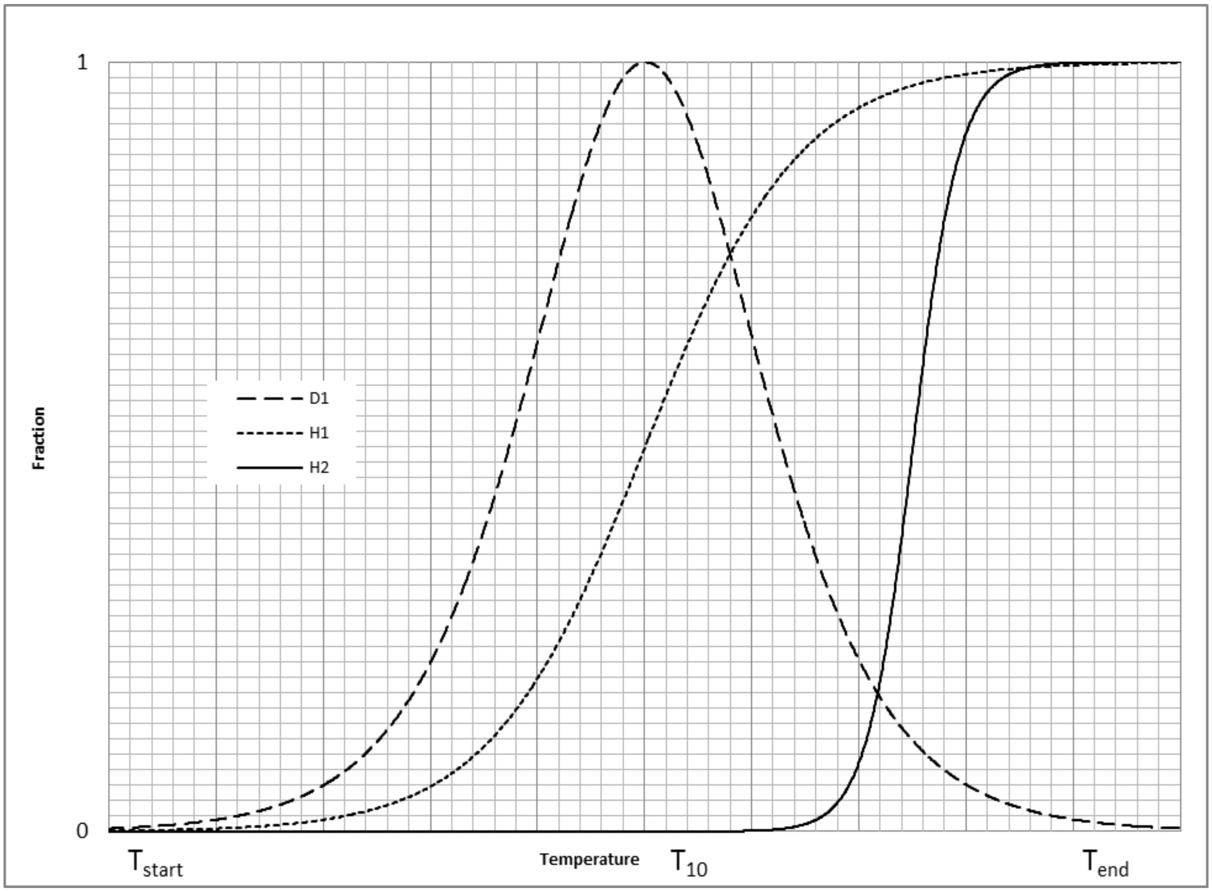

**Figure 9:** The smoothed Heaviside functions used to actuate material property functions.

The first function, $H_1$ is the fraction of material removed as a function of temperature, and increases from 0 to 1 across the phase change interval ($T_{start}$ to $T_{end}$). The second function, $D_1$ is the derivative of $H_1$ with respect to temperature and is used to distribute the latent heat of sublimation across the phase change interval The latent heat of sublimation is the energy required to turn a material from a solid to gas. The area under the function $D_1$ across the phase change interval is equal to unity. Therefore, the product of $D_1$ and the latent heat of sublimation is the latent heat of sublimation distributed across the phase change interval.

The last forcing function, $H_2$ has a smoothing interval over the last 10° C of the material transition temperature range. $H_2$ is used to actuate the material property functions to simulate recession of the irradiated face at the temperature the material is vaporized.

These three forcing functions artificially make an element act as if it has been removed by lowering the radial thermal conductivity by orders of magnitude, raising the through thickness thermal conductivity by orders of magnitude, lowering the density by orders of magnitude and lowering the specific heat by orders of magnitude as shown in Figure 10. This channels the heat applied by the Gaussian surface heat flux through the “removed” elements to the undamaged elements. This through thickness movement of the applied heat models material removal by a laser, because as material is removed, the irradiated surface will concomitantly progress through thickness.

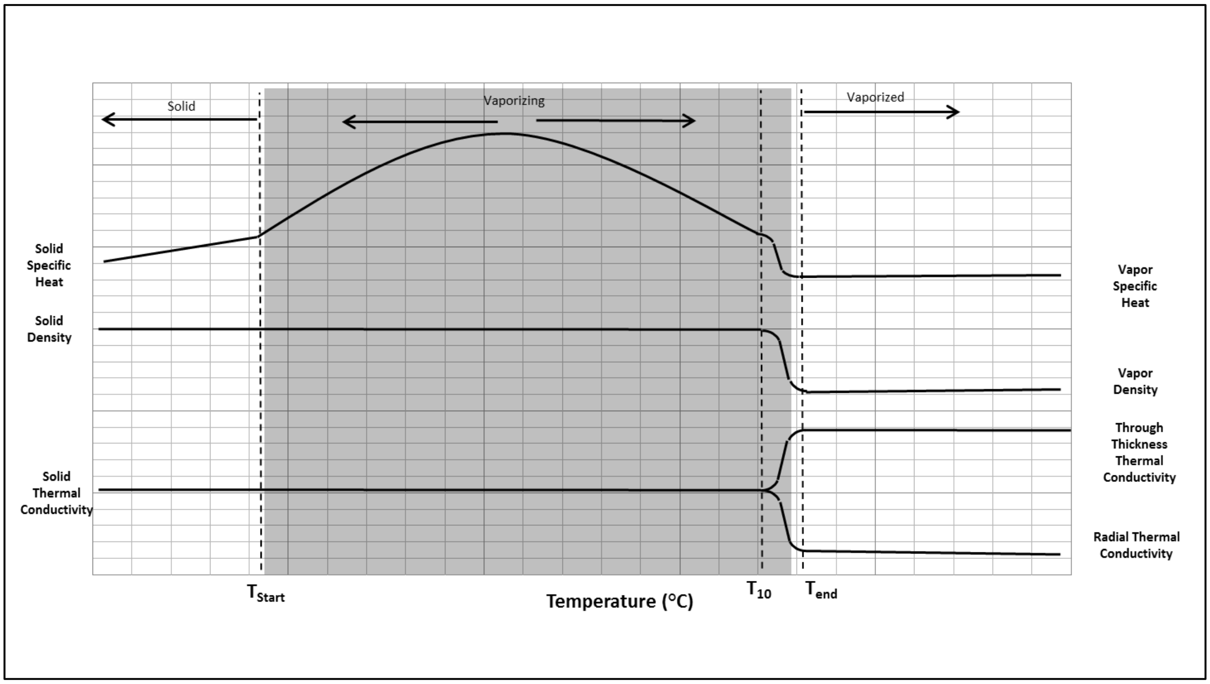

**Figure 10:** Material Property Functions used in Model. $T_{start}$, $T_{end}$ and $T_{10}$ are the start, end and end minus 10ºC temperatures of the phase change interval.

The temperature dependent material density function shown in Figure 10 using the smoothed Heaviside functions in Figure 9 is (Equation 29):

$$\rho = \rho_{solid}(1 - H_2) + \rho_{vapor}(H_2) \tag{29}$$

Similarly the temperature dependent material property functions for effective specific heat $C_{effective}$, radial thermal conductivity $k_r$ and through thickness thermal conductivity $k_z$ follow in Equations 30, 31 and 32:

$$C_{effective} = C_{solid}\,(1 - H_2) + C_{Vapor}(H_2) + \Delta H_{latent}(D_1) \tag{30}$$

$$k_r = k(1 - H_2) + 0.001k(H_2) \tag{31}$$

$$k_z = k(1 - H_2) + 1000k(H_2) \tag{32}$$

Where *k* is the nominal solid thermal conductivity. The radial and through thickness thermal conductivities ($k_r$ and $k_z$) are initially the same in Acrylite because it is an isotropic material, however it is modeled as a transversely isotropic material in order to use the different radial and through thickness properties in Figure 10.

In order to avoid using a complex polynomial as the effective specific heat input for the model, a simpler function was constructed by superimposing the specific and latent heats. Linear fits for specific heat before and after the thermal events were combined with a latent heat of sublimation value distributed across the phase change interval.

The material property functions for CFRP are shown below in Figure 11. They are not to scale and the figure is for illustrative purposes. Exothermic events plot as downward pulses on the effective specific heat line.

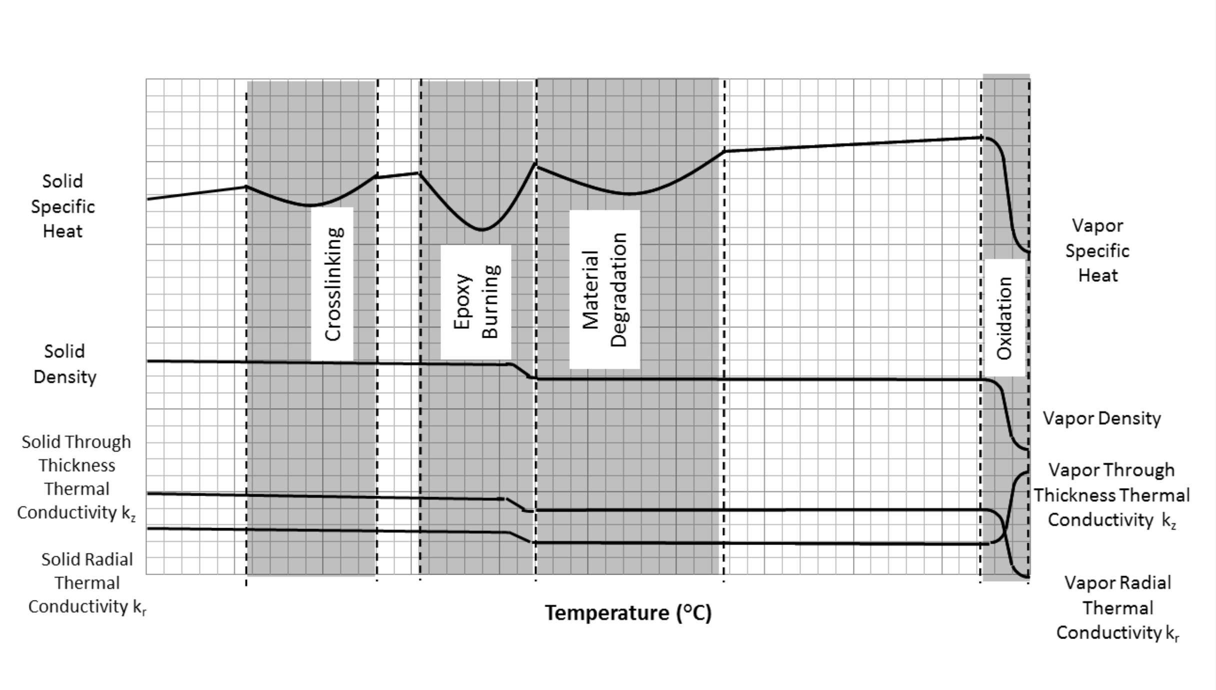

**Figure 11:** Material property functions used for the CFRP model

The material property inputs are functions of temperature that incorporate the forcing functions to actuate them to simulate material removal and distribute latent specific heat. Figure 11 was constructed based on Figure 4, the DSC of CFRP. The first transition is crosslinking, which has an exothermic latent heat associated with it in this case. The next event is epoxy burning, which again has an exothermic latent heat associated with it. The epoxy burning results in the volume of the composite that was epoxy being replaced with air, and a subsequent decrease in the density and thermal conductivities. Since the LFM only captured data on undamaged material, thermal circuit micromechanics models were used to extrapolate the data to include this effect. Equations 2 and 3 were used to compute the thermal conductivity of the damaged material with the matrix density and thermal conductivity values replaced with those of air. Lowering the matrix thermal conductivity values of a micromechanics model results in a lowered overall average thermal conductivity. As the material further degrades, there is another exothermic latent heat associated with it. The exact mechanism of this degradation needs to be investigated further, although it was included in the model analogous to the other effects.

The final thermal event is the removal of the carbon fiber due to oxidation at elevated temperature. This results in the artificial removal of the element as discussed previously. The through thickness and radial thermal conductivity are initially different because this research assumed woven CFRP laminate is a transversely isotropic material. Tresansky et al. [26] showed the validity of this in-plane isotropic assumption for woven fiber composites under HEL irradiation.

The equations for material property functions graphed in Figure 11 are presented below. Each of the four thermal events that occur in CFRP required the three forcing functions shown in Figure 9 so a total of 8 Smoothed Heaviside/ Gaussian Pulse functions were used.

$$k_r = k_{ri}(1 - H_4\ ) + k_{r2}(H_4)(1 - H_8) + k_{r3}(H_8) \tag{33}$$

$$k_z = k_{zi}(1 - H_4) + k_{z2}(H_4)(1 - H_8) + k_{z3}(H_8) \tag{34}$$

$$\rho = \rho_i(1 - H_4) + \rho_2(H_4)(1 - H_8) + \rho_3(H_8) \tag{35}$$

$$C_p = C_{function}(1 - H_8) + C_{final}(H_8) + D_1(C_{latent1}) + D_3(C_{latent2}) + D_5(C_{latent3}) \tag{36}$$

$$C_{function} = 0.7359(T) + 1407.9 \tag{37}$$

As the temperature of an element reaches the temperature at which a thermal event occurs (and the corresponding smoothed Heaviside function changes to unity) the material property functions (Equations 33-37) shift from one value to another as shown in Figure 11. $C_{function}$ in Equation 37 is a linear regression fit with empirical coefficients to the specific heat data shown in Figure 4 that captures the temperature dependency of CFRP specific heat.

## Axisymmetric Model

A 1D proof of concept model was developed specifically to test the computational technique for modeling material removal described previously in this report [26]. After proving the technique a more computationally intensive three dimensional model using best guess material properties was developed [26]. Consistent experimental observations of circularly shaped heat affected zones (HAZ) supported the use of an axisymmetric model [27]. The approximate transverse isotropy of CFRP and full isotropy of Acrylite discussed previously also indicated that an axisymmetric model would perform equally well [10, 25, 26]. Therefore, the model was reduced from 3D to 2D axisymmetric. The axisymmetric model offers improved computational efficiency over the 3D model without a significant loss of fidelity.

The first model with measured material properties developed in this work was for Acrylite loaded with carbon black. This was an effort to capture the behavior of the polymer matrix of a fiber reinforced polymer. Acrylite was chosen based on its expected simplicity (it was recommended as a linearly ablating polymer by Cozzens and Lloyd [19]) and it still produced challenges due to material property dependencies on temperature over the large temperature range experienced during irradiation.

Carbon fiber reinforced polymer (CFRP) was the next material experimentally tested and theoretically modeled. CFRP laminates comprise the skins of a composite sandwich structure, so they are the first logical step towards a sandwich structure model. CFRP reacts differently to electromagnetic radiation than PMMA, reaching and sustaining blackbody radiative equilibrium. In blackbody radiative equilibrium, the heat deposited in the sample by the laser is almost completely re-radiated back to the surroundings.

$$I_{laser}\alpha_{1.07}A \approx \sigma\varepsilon(T_{surface}^4 - T_{surroundings}^4) \tag{38}$$

The left hand side of Equation 38 is the total heat flux into the target calculated as the product of laser irradiance $I_{laser}$, spectral hemispherical absorptivity at 1.07μm $\alpha_{1.07}$, and the beam target area. The right hand side is the heat flux radiated away from the surface calculated as the product of the Stefan-Boltzman constant σ, the total hemispherical emissivity ε, and the fourth power temperature difference between surface and surroundings. The HAZ is formed because some heat is not re-radiated and instead diffuses outwards by conduction and the extent of this HAZ is partially determined by the thermal diffusivity of the material. At the high temperatures maintained in blackbody equilibrium, the carbon fibers are slowly oxidized [28].

The axisymmetric coordinate system and boundary conditions shown in Figure 12 were used for the model.

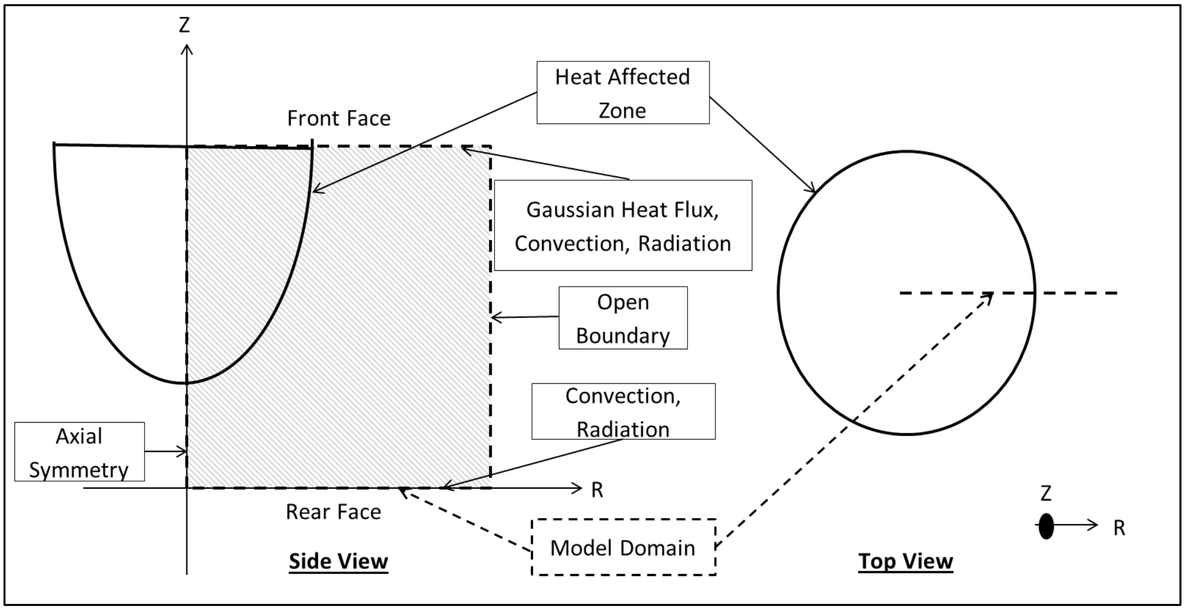

**Figure 12:** Boundary Conditions. Dashed and shaded area is model domain. Solid line is experimental HAZ.

The top surface of the model corresponds to the irradiated face (front face). Three effects are applied here: A Gaussian profile surface heat flux to simulate irradiation (Equation 40), forced convection (Equation 41) and surface to ambient radiation (Equation 45). These three heat fluxes are equated to the heat flux conducted inwards using a surface energy balance in Equation 39.

$$k\frac{\partial t}{\partial z} = q_{laser} + q_{convection} + q_{radiation} \tag{39}$$

Equation 40 is the Gaussian Heat flux as a function of radial position from the beam axis. $\alpha_{1.07}$ is the spectral hemispherical absorbance at 1.07μm (approximated from measurements made with NIR spectroscopy), $I_0$ is the peak irradiance, and $\omega$ is the beam radius defined by the 1/e$^2$ irradiance level (shown later in Figure 15). The value of $I_0$ was chosen so the surface integral of this function (without the absorbance term) over the top surface area is the total power irradiated on the target. This is equal to > 99% of the laser power output. This was selected in order to model the nearly Gaussian beam profile of the IPG-Photonics YLR-100-AC Yb:YAG NIR laser beam (max M$^2$ = 1.07) in the USNA Directed Energy Research Center (DERC) used for the validation experiments [29].

$$q_{laser} = f(r) = \alpha_{1.07} I_0 e^{-\frac{2r^2}{\omega^2}} \tag{40}$$

Equation 40 above assumes that the radial profile of the beam does not change with through thickness position because the propagation distance is small enough for diffractive effects to be negligible. Equation 41 is the heat flux due to convection with a convection coefficient of $h$ = 250 W/m$^2$K.

$$q_{convection} = h(T_{surface} - T_{ambient}) \tag{41}$$

There are two types of convection: forced and free. Forced convection is heat transfer due to fluid flow over a surface due to external means (like a pump or fan or flow over a wing). Free convection is due to buoyancy driven flow caused by the difference in density of fluids of different temperatures; the fluid flow over the surface is caused by the heat of the surface. Nusselt number ($Nu_L$) correlations for forced and free convection were used to set upper and lower bounds for the heat transfer coefficient. Nusselt numbers are dimensionless numbers calculated using dimensionless Reynolds ($Re_L$), Rayleigh ($Ra_L$), and Prandtl ($Pr$) numbers as well as the characteristic length $L$. Using the Nusselt number, $h$ was calculated to be between 25 W/m$^2$K and 250 W/m$^2$K. Convection coefficients for free convection are typically on the order of 10-100 W/m$^2$K and forced convection coefficients on the order of 100-1000 W/m$^2$K [30]. The degree to which the convection was forced or free was then determined using a Grashof number inequality [30]. The upper bound is set based on forced convection with the surface airflow applied using a 100 cfm vacuum (Equation 42).

$$Nu_L = 0.664(Re_L)^{\frac{1}{2}}(Pr)^{\frac{1}{3}} = \frac{hL}{k_{air}} \tag{42}$$

A different Nusselt number correlation for free convection on a vertical plate approximates the lower bound [30] (Equation 43).

$$Nu_L = 0.68 + \frac{0.670 Ra_L^{\frac{1}{4}}}{\left(1 + \left(\frac{0.492}{Pr}\right)^{\frac{9}{16}}\right)^{\frac{4}{9}}} \tag{43}$$

The following Grashof number inequality (Equation 44) is satisfied. The Grashof number ($Gr_L$) is a dimensionless number that approximates the ratio of buoyant to viscous forces and consequently is the ratio of free to forced convection. Equation 44 indicates that the forced convection effects completely dominate, therefore $h$ was chosen to be the upper bound of 250 W/m$^2$K.

$$\frac{Gr_L}{Re^2} \ll 1 \quad \text{where} \quad Gr_L = \frac{g\beta(\mathrm{T}_{\mathrm{surface}} - T_\infty)L^3}{\nu^2} \tag{44}$$

Equation 45 is the heat flux due to surface to ambient radiation. Since surface to ambient radiation is dependent on the fourth power temperature difference between the surface and the temperature of the surroundings, it is logical that the higher temperature experienced by CFRP upon irradiation would cause a large outward heat flux. Similarly, the heat loss due to radiation in Acrylite would be significantly less. The extremely small value of the Stefan Boltzman constant $\sigma$ $5.67\times10^{-8}$ $\mathrm{W/m^2K^4}$ means the fourth power temperature difference must be very large for the heat flux to be significant. Therefore, surface to ambient radiation was neglected in the model for Acrylite.

$$q_{radiation} = \varepsilon\sigma(T_{surface}^4 - T_{ambient}^4) \tag{45}$$

Emissivity and absorptivity are material, direction, wavelength, and temperature dependent. When an emissivity is being referred to as dependent upon all these variables it is described as a spectral directional emissivity (similarly for absorptivity) at a specific temperature [30].

Unless the direction of radiation is of particular interest to the work being done it is common to work with hemispherical emissivity and absorptivity as was done here [30]. Hemispherical values deal with the average value of absorptivity or emissivity across $2\pi$ steradians. A steradian is a unit of solid angle, with $4\pi$ steradians subtending a sphere [30]. A flat surface can absorb or emit radiation across a hemisphere or $2\pi$ steradians, and the average value of emissivity or absorptivity across this solid angle is called the hemispherical emissivity or hemispherical absorptivity.

Furthermore, emissivity and absorptivity depend on wavelength. When described as wavelength dependent they are referred to as spectral emissivity or spectral absorptivity. Since a particular wavelength radiation (1.07µm or NIR) is absorbed by the materials in this research it is necessary to measure the spectral absorptivity of the materials using FORS. The radiation emitted from the material is considered as a broadband outward heat flux in this work and the spectral emissivity is not relevant (except in the context of camera saturation which will be discussed later). Therefore a total or average spectral emissivity was used.

Additionally, emissivity and absorptivity depend on temperature [30]. For all materials the total hemispherical emissivity and total hemispherical absorptivity at a specific temperature are equal. Since all materials are constantly both emitting and absorbing radiation this is necessary to satisfy the laws of thermodynamics. However, both spectral and total hemispherical emissivity and absorptivity are temperature dependent. This dependence is difficult to measure and was not investigated in this research.

The other boundaries in Figure 12 are axial symmetry along the beam axis or model radial axis. Axial symmetry is accomplished by setting the derivative of temperature with respect to direction (proportional to the heat flux due to conduction) equal to zero, which is commonly known as an insulative boundary condition (Equation 46).

$$k\frac{\partial T}{\partial r} = 0 \tag{46}$$

An open boundary condition is applied to the outer surface of the model to limit the computational domain and increase the efficiency of the model (Equation 47). An open boundary simulates that there is more material beyond the boundary and allows heat to flow out, but heat does not flow in.

$$k\frac{\partial T}{\partial r} = 0 \quad only\ if \ \ r \rightarrow - \tag{47}$$

The bottom surface (rear face) is analogous to the top (front face) without the laser heat flux applied (Equation 48).

$$k\frac{\partial T}{\partial Z} = q_{convection} + q_{radiation} \tag{48}$$

### Material Property Inputs

The material properties used as inputs for the computational model are summarized in the following tables.

**Table 1**: Acrylite GP Material Property Inputs

| Parameter | Units | Variable | Solid Value | Vapor/ Ablated Value |
|---|---|---|---|---|
| Sample Thickness | mm | $Z$ | $6.19_1$ | $6.19_1$ |
| Simulation Time | s | $t_{stop}$ | $2_1$ | $2_1$ |
| Phase change start | °C | $T_{start}$ | $327_1$ | $327_1$ |
| Phase change end | °C | $T_{end}$ | $437_1$ | $437_1$ |
| Phase change end - 10 | °C | $T_{10}$ | $427_1$ | $427_1$ |
| Initial Temperature | °C | $T_0$ | $22_1$ | $22_1$ |
| Latent Heat of Sublimation | $\frac{kJ}{kg}$ | $\Delta H$ | $521_1$ | $521_1$ |
| Radial Thermal Conductivity | $\frac{W}{mK}$ | $k_r$ | $0.19_2$ | $0.00019_3$ |
| Through Thickness Thermal Conductivity | $\frac{W}{mK}$ | $k_z$ | $0.19\ _2$ | $190_3$ |
| Density | $\frac{kg}{m^3}$ | $\rho$ | $1190_2$ | $1_3$ |
| Specific Heat (range of function) | $\frac{J}{gK}$ | $C$ | $1250\text{-}2400_1$ | $500_3$ |
| Beam Radius | mm | $\omega$ | $2.77_2$ | $2.77_2$ |
| Absorptivity | % | $\alpha$ | $91_1$ | $91_1$ |
| Laser Power | W | $P$ | $100_1$ | $100_1$ |
| # of Radial Mesh Elements/ Element Ratio | - | - | $40_1$ / $10_1$ | $40_1$ / $10_1$ |
| # of Through Thickness Mesh Elements/ Element Ratio | - | - | $180_1$ / $1_1$ | $180_1$ / $1_1$ |
| Tolerances | - | - | 0.0001 | 0.0001 |

$_1$ properties measured/calculated at USNA or by collaborators, $_2$ properties from the literature, $_3$ simulated properties to cause material ablation

Table 1 details the material property inputs used for modeling Acrylite. The specific heat, heat of sublimation and phase change interval were determined using the DSC, while the absorptivity was determined using FORS. The other values were either obtained from the literature, or were simulated to create material removal. The values used to simulate material removal (subscript 3) can be clarified using Figure 10.

The material property inputs for CFRP are shown below in Table 2.

**Table 2**: Material Property Inputs for CFRP Model

| **Parameter** | **Units** | **Variable** | **Undamaged** | **Crosslinking** | **Epoxy Burn off** | **Material Degradation** | **Carbon Fiber Oxidation/Removed Element** |
|---|---|---|---|---|---|---|---|
| Sample Thickness | mm | $Z$ | $2.62_1$ | $2.62_1$ | $2.62_1$ | $2.62_1$ | $2.62_1$ |
| Simulation Time | s | $t_{stop}$ | $300_1$ | $300_1$ | $300_1$ | $300_1$ | $300_1$ |
| Phase change start | °C | $T_{start}$ | - | $155_1$ | $327_1$ | $450_1$ | $1000_2$ |
| Phase change end | °C | $T_{end}$ | - | $295_1$ | $450_1$ | $633_1$ | $1525_2$ |
| Phase change end - 10 | °C | $T_{10}$ | - | $285_1$ | $440_1$ | $623_1$ | $1515_2$ |
| Initial Temperature | °C | $T_0$ | $22_1$ | $22_1$ | $22_1$ | $22_1$ | $22_1$ |
| Crosslinking Latent Heat | $\frac{\mathrm{kJ}}{\mathrm{kg}}$ | $\Delta H$ | - | $-12.4_1$ | - | - | - |
| Epoxy Burning Latent Heat | $\frac{\mathrm{kJ}}{\mathrm{kg}}$ | $\Delta H$ | - | - | $-27.2_1$ | - | - |
| Material Degradation Latent Heat | $\frac{\mathrm{kJ}}{\mathrm{kg}}$ | $\Delta H$ | - | - | - | $-19.2_1$ | - |
| Radial Thermal Conductivity | $\frac{\mathrm{W}}{\mathrm{mK}}$ | $k_r$ | $5.5_2$ | $5.5_2$ | $4.6_2$ | $4.6_2$ | $0.0001_3$ |
| Through Thickness Thermal Conductivity | $\frac{\mathrm{W}}{\mathrm{mK}}$ | $k_z$ | $1_2$ | $1_2$ | $0.5_2$ | $0.5_2$ | $1000_3$ |
| Density | $\frac{\mathrm{kg}}{\mathrm{m}^3}$ | $\rho$ | $1700_2$ | $1700_2$ | $1000_2$ | $1000_2$ | $1_3$ |
| Specific Heat | $\frac{\mathrm{J}}{\mathrm{gK}}$ | $C$ | $1.25\text{-}1.75_1$ | $1.25\text{-}1.75^1$ | $1.25\text{-}1.75_1$ | $1.25\text{-}1.75_1$ | $0.5_3$ |
| Beam Radius | mm | $w$ | $2.77_2$ | $2.77_2$ | $2.77_2$ | $2.77_2$ | $2.77_2$ |
| Absorptivity | % | $a$ | $91_1$ | $91_1$ | $91_1$ | $91_1$ | $91_1$ |
| Laser Power | W | $P$ | $100_1$ | $100_1$ | $100_1$ | $100_1$ | $100_1$ |
| # of Radial Mesh Elements/ Element Ratio | - | - | $50/10_1$ | $50/10_1$ | $50/10_1$ | $50/10_1$ | $50/10_1$ |
| # of Through Thickness Mesh Elements/ Element Ratio | - | - | $45/1_1$ | $45/1_1$ | $45/1_1$ | $45/1_1$ | $45/1_1$ |

$_1$ properties measured/calculated at USNA or by collaborators, $_2$ properties from the literature, $_3$ simulated properties to cause material ablation. Negative latent heats denote endotherm.

The specific heat, latent heats, and nominal thermal conductivity were measured using DSC and LFM. The crosslinking, epoxy burning and material degradation values for density and thermal conductivities were calculated using rule of mixtures and thermal circuit analogies. The values used to simulate material removal (subscript 3) can be clarified using Figure 11.

## THEORETICAL ACRYLITE RESULTS

The model was run using the parameters in Table 1 with the beam applied as in Equation 40 and the theoretical thermal field and recession rate were calculated. The theoretical recession rate is determined by analyzing the burn depth predicted by the model at specific times and plotting the results. To show both material removal and the temperature field on the same graph, the meaningless temperature field associated with vaporized or actuated elements had to be suppressed using Equation 49.

$$T * ((1 - H_2) > 0.99\ ) \tag{49}$$

$H_2$ is the smoothed Heaviside function that changes from zero to unity to artificially remove an element. The inequality in Equation 49 is satisfied only when $H_2$ has not yet artificially removed an element. Equation 49 creates a plot that displays the temperature of elements that have not been removed, and plots removed elements as being 0 degrees or colored black in this scale. The 0.99 in the inequality helps to smooth out noise created during the numerical methods used for solution. The outputs from the model (plots of Equation 49) are shown in Figure 13. The thermal gradient predicted is very large and the HAZ is small due to the low thermal diffusivity of Acrylite.

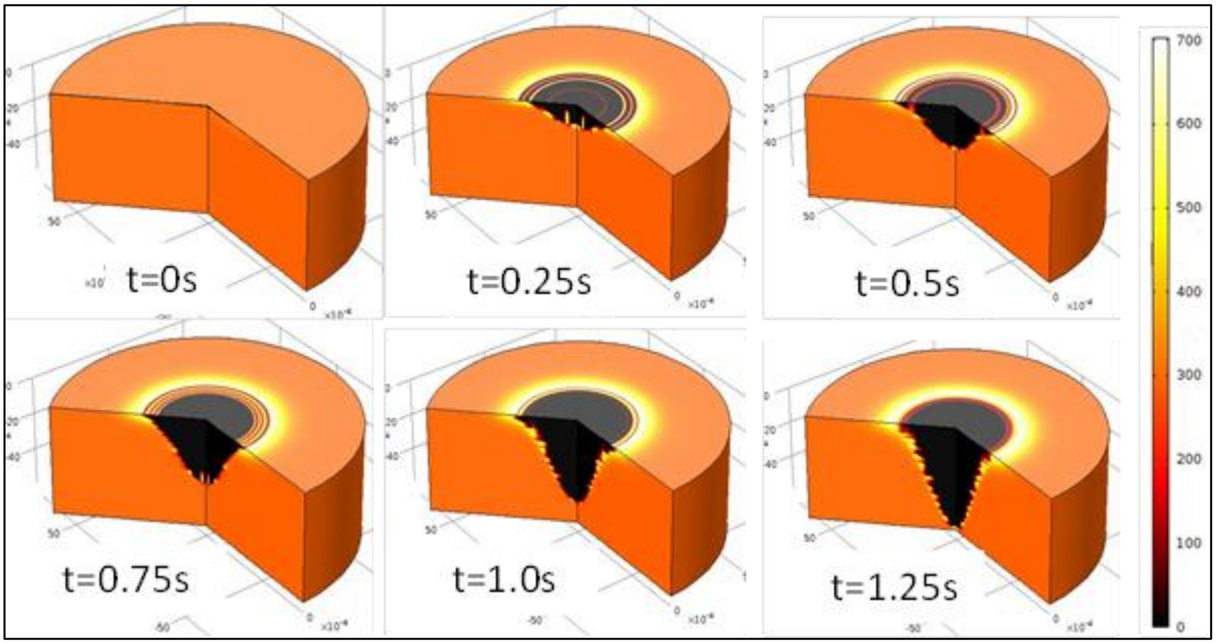

**Figure 13:** The function T*((1-$H_2$)>0.99) is plotted. T*((1-$H_2$)>0.99) is the temperature field with vaporized elements removed and plotted as 0 K in black. The scale is in Kelvin.

A sensitivity analysis was conducted on the Acrylite model in an effort to reduce the preliminary error in recession rate. The analysis was conducted by a one factor at a time perturbation or repeatedly running the model and changing one input in between each run. The sensitivity of a model's output to each input can be viewed as a partial derivative (Equations 50 and 51).

$$output = f(input_A, input_B, input_C, input_D \dots) \tag{50}$$

$$SensitivityA = \frac{\partial ouput}{\partial input_A} \tag{51}$$

The results from this analysis are summarized in the following table.

**Table 3**: results of sensitivity analysis conducted on Acrylite model.

| **Parameter** | **Units** | **Variable** | **Sensitivity** | **Notes** | **Actions Taken** |
|---|---|---|---|---|---|
| Tolerances | - | - | 5.5556 | - | Tolerances tightened to reduce convergence issues |
| Absorptivity | % | $a$ | 5.0161 | Measured by FORS and confirmed by NIRS at USNA | - |
| Beam Radius | mm | $w$ | 2.5759 | Provided by laser manufacturer | - |
| Thermal Conductivity | $\frac{W}{mK}$ | $k$ | 0.4094 | Provided by Acrylite manufacturer | - |
| Power | W | $P$ | 0.0323 | Measured by Thermopile at USNA | - |
| Phase change end | °C | $T_{end}$ | 0.0074 | Measured by DSC at USNA | DSC repeated, average of three tests used. |
| # of Radial Mesh Elements/ Element Ratio | - | - | 0.0067 | Higher mesh size is more accurate. | Revised model elements were increased until sensitivity driven to zero. |
| # of Through Thickness Mesh Elements/ Element Ratio | - | - | 0.0060 | Higher mesh size is more accurate. | Revised model elements were increased until sensitivity driven to zero. |
| Solid Density | $\frac{kg}{m^3}$ | $\rho_i$ | 0.0047 | Provided by manufacturer | - |
| Latent Heat of Vaporization | $\frac{kJ}{kg}$ | $\Delta H$ | 0.0027 | Measured by DSC at USNA | DSC repeated, average of three tests used. |
| Initial Temperature | °C | $T_0$ | 0.0025 | Measured by thermocouple at USNA | - |
| Convection Heat Transfer Coefficient | $\frac{W}{m^2K}$ | $h_c$ | 0.0004 | Calculated using Nusselt number correlations | Recalculated based on forced convection. |
| Phase change start | °C | $T_{start}$ | 0.0002 | Measured by DSC at USNA | DSC repeated, average of three tests used. |
| Vaporized Density | $\frac{kg}{m^3}$ | $\rho_v$ | 0.0000 | - | - |
| Total Hemispherical Emissivity | - | $\varepsilon$ | 0.0000 | - | - |
| Specific Heat | $\frac{J}{gK}$ | $C$ | 0.0000 | Measured by DSC at USNA | - |
| Sample Thickness | mm | $Z$ | 0.0000 | Measured by calipers at USNA | - |
| Multiplier for Forcing Functions | - | - | 0.0000 | Value arbitrary provided it is significantly large | - |

Using the above approach the most sensitive inputs were determined to be the convergence tolerances, absorptivity, beam radius, thermal conductivity, power, $T_{end}$, element size, and solid density. The least sensitive inputs were the multiplier for the forcing functions, the sample thickness, specific heat, emissivity, and $T_{end}$. There was significant confidence in the measurements/source for the absorptivity, beam radius, thermal conductivity, laser power, the solid density, and initial temperature to not necessitate further investigation. Additionally, the model was proven to be wholly insensitive to inputs whose values were chosen to cause material removal such as the multiplier for forcing functions and the vaporized density, meaning the model architecture was robust.

The changes detailed in Table 3 were made to the model following the sensitivity analysis to increase the model accuracy. Using better tolerances reduced convergence issues in the model. When COMSOL assembles matrices using the governing equations for solving it has to make them fit together. The goodness of this fit is determined by the tolerances. Looser tolerances may make a model run faster, but they leave it at risk for convergence issues.

The DSC measurements were repeated and new values that were the average of three runs were used to increase confidence in the subsequent inputs. The number of elements in both the radial and through thickness direction were increased. The number of elements used increases the size and complexity of the matrices COMSOL must solve at each time step and can significantly slow down the model. However, using too few elements makes the element size large and reduces the resolution of the results. Furthermore, because the model architecture involves numerically removing elements, if the element size is too large, the recession rate will be artificially increased as large chunks of material will be removed, instead of moving at the actual recession rate.

## THEORETICAL CFRP RESULTS

Following the Acrylite model a CFRP model was created. The CFRP model was then run and the transient thermal field and material recession rate were calculated. To show both material removal and the temperature field on the same graph, the removed elements meaningless temperature had to be suppressed using Equation 52.

$$T * ((1 - H_8) > 0.99\ ) \tag{52}$$

Equation 52 is analogous to Equation 49 except that $H_2$ has been replaced by $H_8$. $H_8$ is the smoothed Heaviside function that changes from zero to unity to artificially remove an element from the CFRP model. The inequality in Equation 52 is satisfied only when $H_8$ has not yet artificially removed an element. Equation 52 creates a plot that displays the temperature of elements that have not been removed, and plots removed elements as being 0 K. The outputs from the model (plots of Equation 52) are shown in Figure 14.

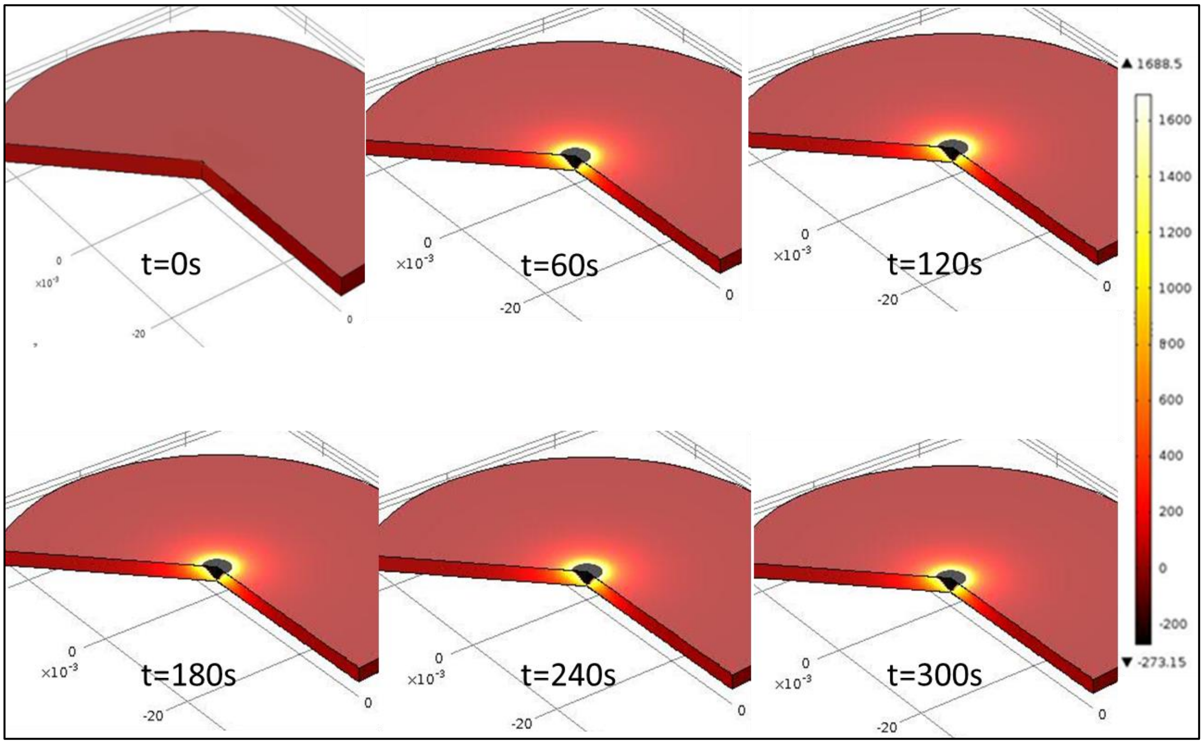

**Figure 14:** Plots of transient temperature and material removed (Equation 52) generated with CFRP model. Temperature scale is in Kelvin.

Figure 14 above shows the thermal field (Equation 52) from the front face as it develops during irradiation. Qualitatively, the front face HAZ and rear face HAZ match what is observed experimentally, and the front face and rear face temperatures are similar to what has been reported and observed [26, 27, 31]. Possible sources of error include material property variation at high temperatures and lack of reaction rate kinetics of carbon fiber oxidation.

An instantaneous material removal is correct for Acrylite, because it undergoes a phase change and vaporizes instantly. However, for CFRP, the material removal mechanism is a chemical reaction that requires a finite amount of time to complete. Therefore, the modeling mechanism for oxidation needs to take a finite amount of time. This is modeled by the Arrhenius equation. The amount of time it takes is temperature dependent, and the hotter it is the faster it will oxidize [28]. This reaction rate dependence would reduce the material removal rate and change the model in the direction of less error.

# EXPERIMENTATION

The primary goal of this research was to produce a computational model capable of predicting both the temperature field caused by HEL irradiation and capture concomitant material removal. This was accomplished with a two pronged approach of modeling and experimentation. HEL irradiation experiments provide material removal (recession) rate data as well as temperature data for comparison to the model predictions. These comparisons were used to iterate the model towards higher accuracy.

USNA's Directed Energy Research Center (DERC) has a 100W nominal power Yb:YAG fiber coupled laser produced by IPG Photonics that lases at 1.07 µm or NIR. It has a maximum 5.5mm $1/e^2$ beam diameter as measured by the manufacturer giving an equivalent tophat profile average irradiance of approximately 500 W/cm$^2$ [29]. An electromagnetic beam has an infinite width (though rapidly diminishing to negligible power), as does a Gaussian distribution. Therefore the beam diameter needs to be defined, and the $1/e^2$ value of the peak or on axis irradiance is used as the beam radius by convention [18,19]. Figure 15 shows a Gaussian beam and how the beam diameter is defined.

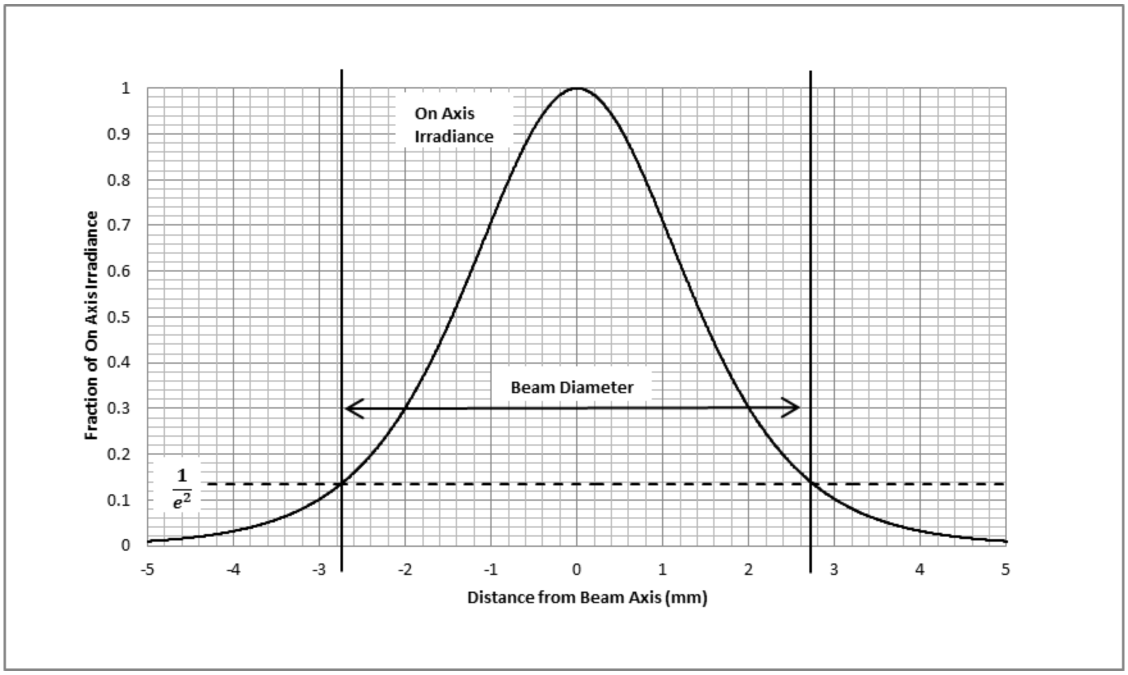

**Figure 15:** Beam diameter defined on a Gaussian beam profile.

The $M^2$ value of a beam describes its beam quality and is the ratio of the diameters of a perfect (diffraction limited) beam to a beam with less than perfect quality at the focal length of the beam. The laser's max $M^2$ value of 1.07 is very close to unity indicating that the beam is near diffraction limited and has a nearly Gaussian shape. Because of this, side lobes and the Airy disk (shapes of beams with higher $M^2$) were neglected in calculations and the beam was assumed to be purely Gaussian.

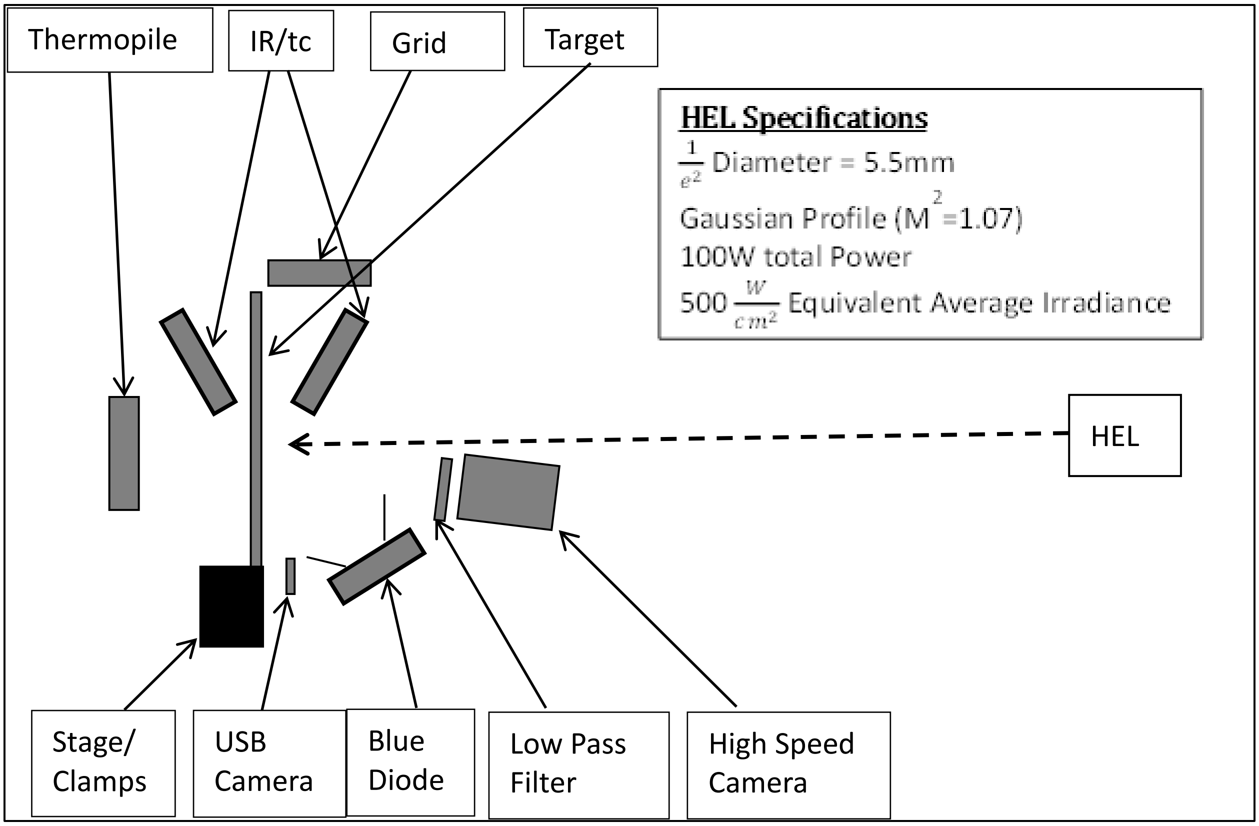

**Figure 16:** A top down view of the laser table set up for burn through experiments at the USNA DERC.

Figure 16 shows the experimental setup used in the DERC at USNA to test recession rate. The samples were held and moved by the stage/clamp. A USB camera collected video of the front face during Acrylite irradiation. A grid (see Figure 16) was setup to help make qualitative observations of material ejected or horizontal jets off the surface. A nominally 0.25 inch thick Acrylite GP sample and a nominally 2.5mm thick CFRP sample were irradiated for 0.5, 1, 1.5, 2, and 2.5 seconds at 100W power. After irradiation, measurements were made of the hole depth for each test in each sample. Care was taken to space the experiments to avoid overlap of the HAZ from different tests.

To measure temperature, two OS37-60-CF-S infrared thermocouples (IR/tc) were acquired from Omega and installed as shown in Figure 16 above. IR/tc are a non-contact temperature measurement device that work by measuring emitted IR radiation. The IR/tc work best at elevated temperatures and longer timescales than those seen during Acrylite testing, however were extremely valuable for CFRP testing. The IR/tc required significant calibration against samples and to each other. Additionally, view factors and placement had to be considered when employing them. More information on IR/tc can be found in APPENDIX G.

Because the CFRP samples reach such elevated temperatures during irradiation, they emit significant amounts of both IR radiation (measured by the IR/tc) as well as visible radiation. (This was a lesser concern for Acrylite but still an issue nonetheless). As a material gets hotter, it will emit radiation with shorter wavelengths. The spectral emissive power of a surface is governed by equation [30]:

$$E_{\lambda,b}(\lambda,T) = \frac{C_1}{\lambda^5\left(e^{\frac{C_2}{\lambda T}} - 1\right)} \tag{53}$$

Where $E_{\lambda,b}(\lambda,T)$ in Equation 53 is the spectral emissive power or the irradiance emitted per wavelength. $C_1$ and $C_2$ are the first and second radiation constants and are equal to $3.742 * 10^8$ Wμm$^4$/m$^2$ and $1.439 * 10^4$ μm K respectively [30]. The spectral emissive power is plotted against the wavelength, showing the spectral distribution of radiation emitted from different temperature surfaces.

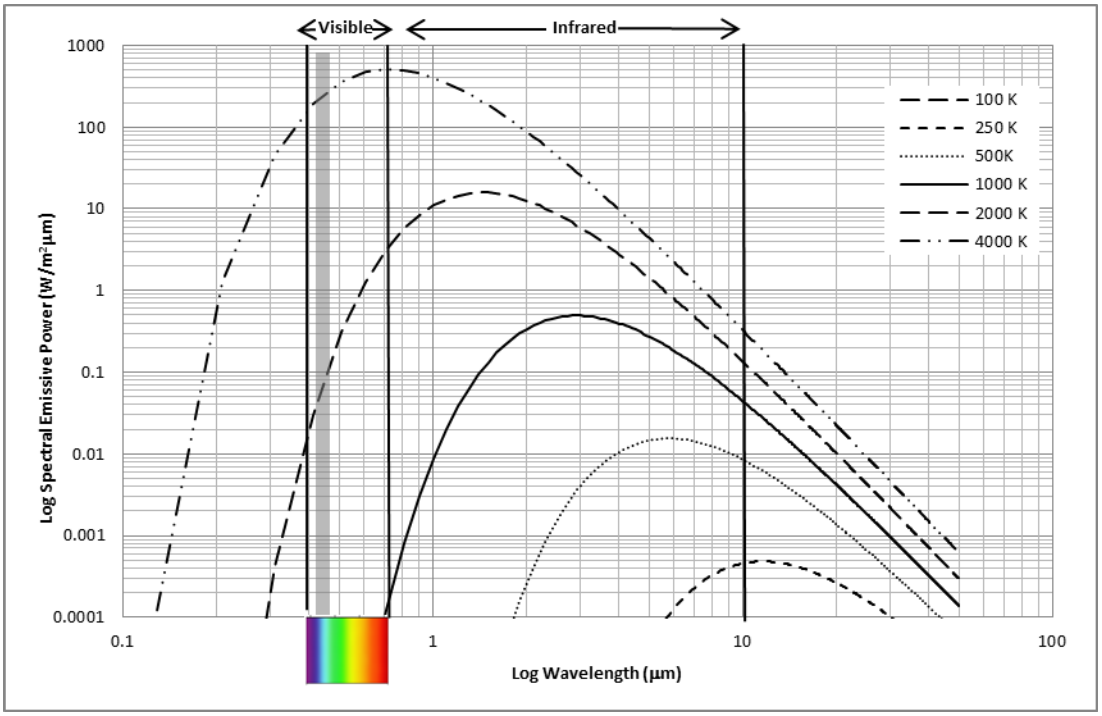

**Figure17:** The spectral emitted radiation distribution for a theoretical blackbody.

Visible radiation has a shorter wavelength than IR radiation, and blue and violet light have even shorter wavelengths in the visible spectrum. Shorter wavelength radiation is higher energy and comes from proportionally higher temperatures. Very little blue light is emitted from the irradiated material (approximate surface temperature of 1600C). To prevent the camera from being saturated with radiation emitted from the target a filter that only allows blue light (4.35-4.90 μm) through it was placed in front of the camera. The shaded grey area in Figure 17 is the pass bandwidth of the filter. The power emitted from a 1600C blackbody with a wavelength less than 4.9μm (the upper wavelength of the pass band for the filter) is less than 2 W/m$^2$μm and is negligible. Diodes at 4.45μm were used to illuminate the target with blue light (which is not emitted from the surface) to provide light for the camera [32]. The blue light is reflected by the material and the diodes act as floodlights to provide enough light in a wavelength that can pass through the filter to get proper images with the camera.

Recession rate was determined after each set of tests by measuring with calipers the depth of the holes created. By comparing the hole depth to the irradiation time for each hole, a recession rate was calculated. The HEL creates a hole in the material related to the shape of the beam profile, so care was taken to measure to the bottom of the hole created.

The effect of smoke produced by material ablation was investigated as a potential source of error in recession rate. When PMMA is vaporized by a HEL, a horizontal jet of carbon black laden smoke was observed originating from the irradiated area and moving through the beam propagation path. This smoke was determined to have a velocity of 75cm/s by analysis of the video captured (Figure 18). When the smoke was illuminated by the laser as shown in Figure 18, it was postulated that significant energy was being absorbed by the smoke before it could reach the sample.

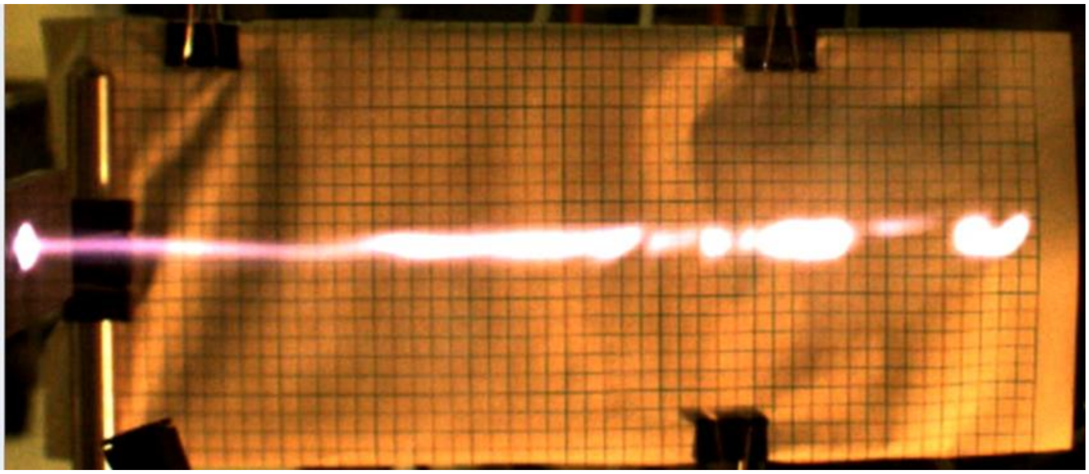

**Figure 18:** Photograph of smoke in beam path illuminated by HEL (grid squares are 0.2 inch on a side).

The effect of the smoke on recession rate was investigated by applying a 100 cfm vacuum above the sample. The vacuum creates airflow that disrupts any smoke produced by the sample and prevents the smoke from entering the beam path. The results from irradiation with and without smoke are plotted in Figure 19.

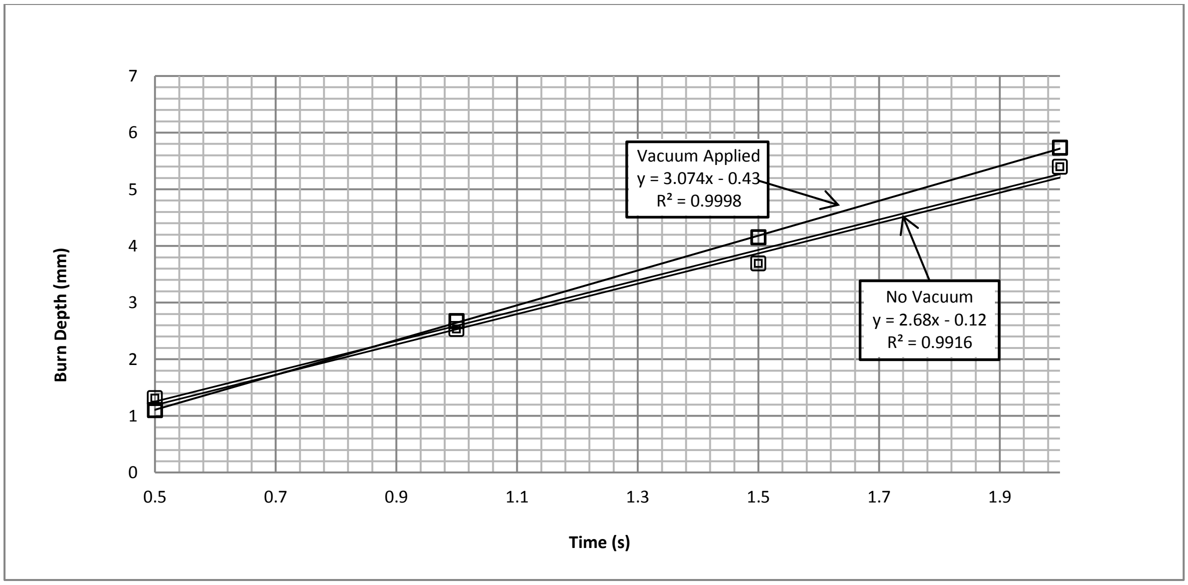

**Figure 19:** The burn depth for specific burn times for Acrylite GP with and without smoke removal.

Applying a vacuum (hence removing smoke) increases the average of the instantaneous burn rates evaluated at each data point by 2%. The slope of the linear regression fits increases 14% with the vacuum applied. Therefore there is a slight increase in burn rate by applying a vacuum and removing the smoke, although this effect was difficult to quantify and also of low statistical significance given variation in the data. Additionally, any heat transfer by advection, or the removal of heat by mass transfer, is captured by the model. The model removes an element artificially by altering its material properties. By lowering the specific heat and density the model is effectively removing thermal mass and captures heat transfer by advection.

Carbon black loaded PMMA in the form of Acrylite GP was chosen because PMMA was recommended as a linearly ablating material [18, 19]. Often PMMA is colored using blue or indigo dyes to achieve a black color to the human eye [18,19]. However, these dyes do not absorb NIR radiation and the HEL will pass though it virtually unabsorbed. Carbon black has an extremely high absorbance for the NIR wavelength of the HEL in question and couples the radiation to the PMMA very efficiently.

## EXPERIMENTAL RESULTS:

Figure 20 compares the theoretical recession rate of Acrylite to the experimental recession rate for three samples of Acrylite with material property inputs measured for each sample. The model is over predicting the recession rate by approximately 25%. Both are nearly linear for the time span of 0 to 2.5 seconds (at 2.5 seconds a 0.25 inch sample is completely penetrated). The model predicts burn through at approximately 1.75 seconds. After complete burn through has occurred in the model, the model will continue to report the burn depth as the sample thickness, which would suggest nonlinearity that is not present. More data are needed in the low burn time region, however they are difficult to collect because the effects are much less pronounced and harder to measure.

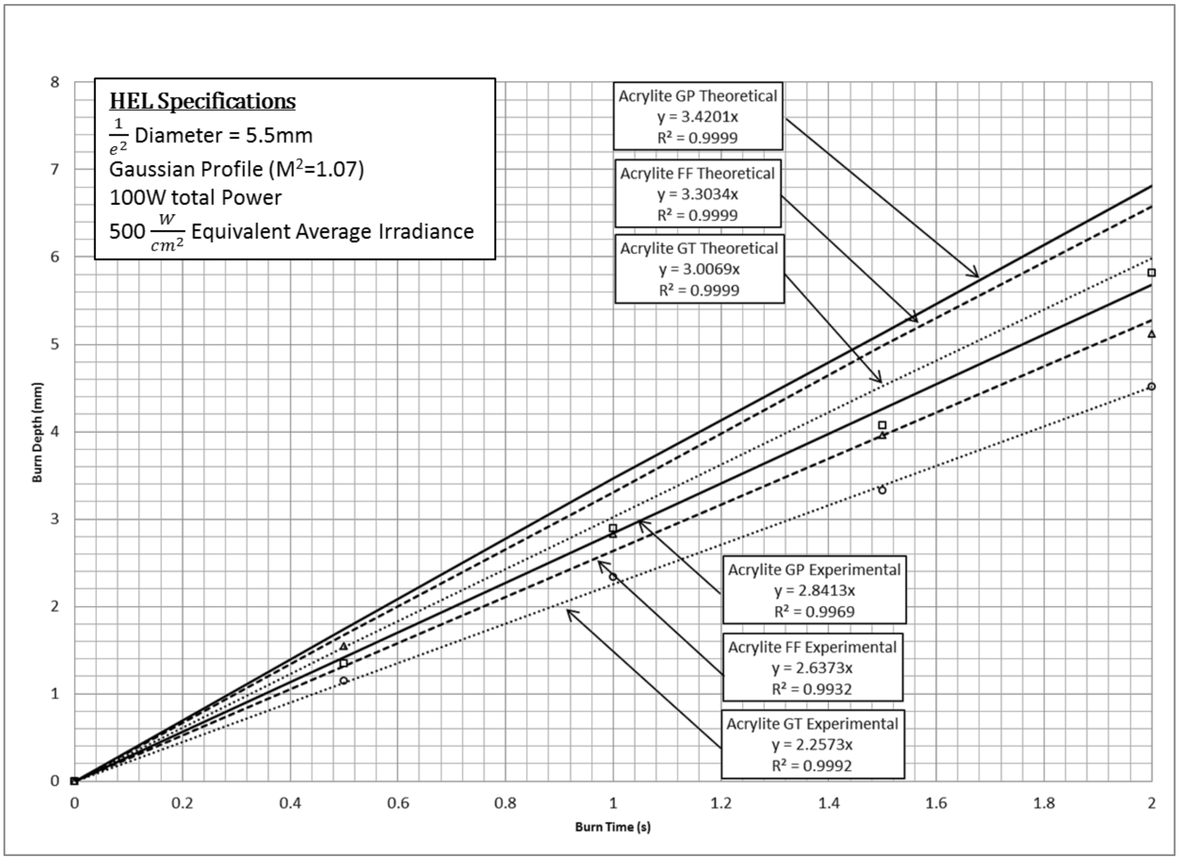

**Figure 20:** Comparison of the experimental and theoretical recession rates for three samples of Acrylite.

The CFRP laminate described previously was tested experimentally for comparison to the theoretical model. The sample was irradiated with the same IPG photonics laser used for the Acrylite testing for 100, 150, 200, 250, and 300 seconds again at 100W power. An airflow of 100 cfm was applied to the sample to prevent flames, and to represent airflow conditions experienced by CFRP in flight. Figure 21 shows pictures from the rear face during irradiation.

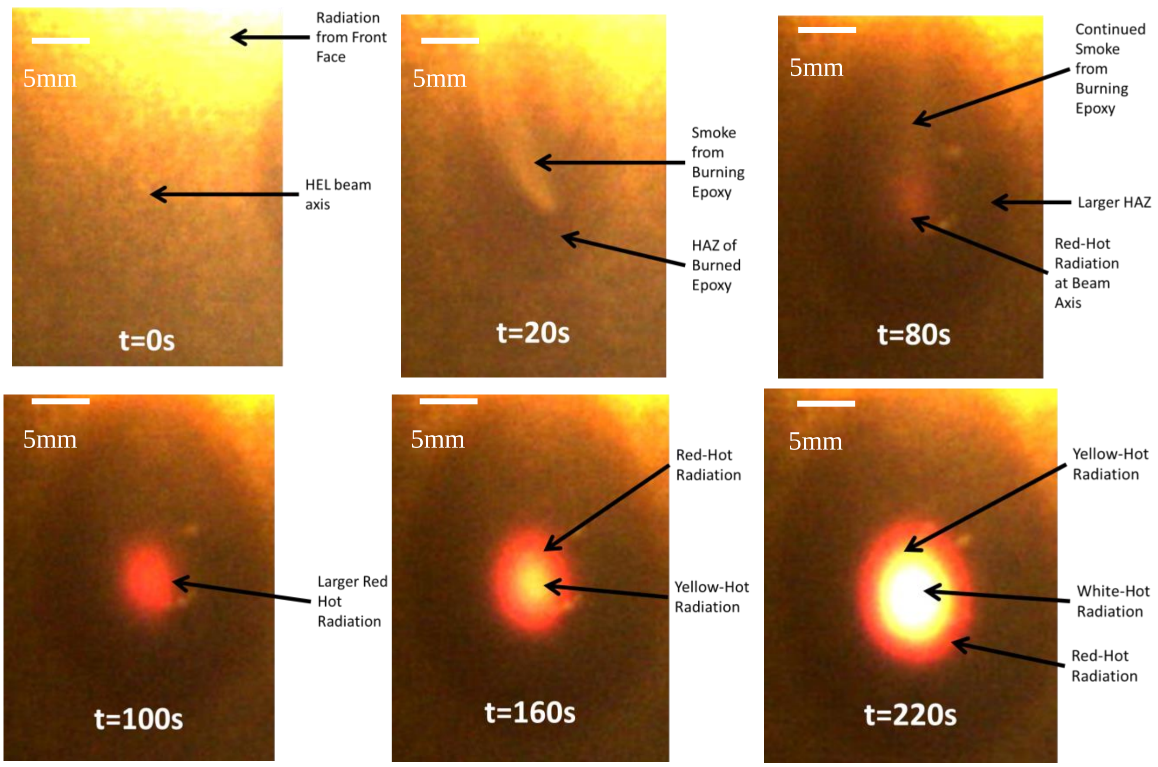

**Figure 21:** Pictures of the rear face of CFRP while irradiated.

Following irradiation the sample was inspected and measurements taken of the size of the HAZ, the epoxy damage diameter, the burn hole diameter and the hole depth. The HAZ diameter was defined as the edge of discoloration in the epoxy, and the epoxy damage diameter was defined as the area where the epoxy had been completely removed. The hole diameter was defined as the edge of the white ash that coated the hole, and the hole depth was defined as the lowest point of the Gaussian shaped hole. A picture of the front face posttest and a diagram of the measurements made are shown below in Figure 22.

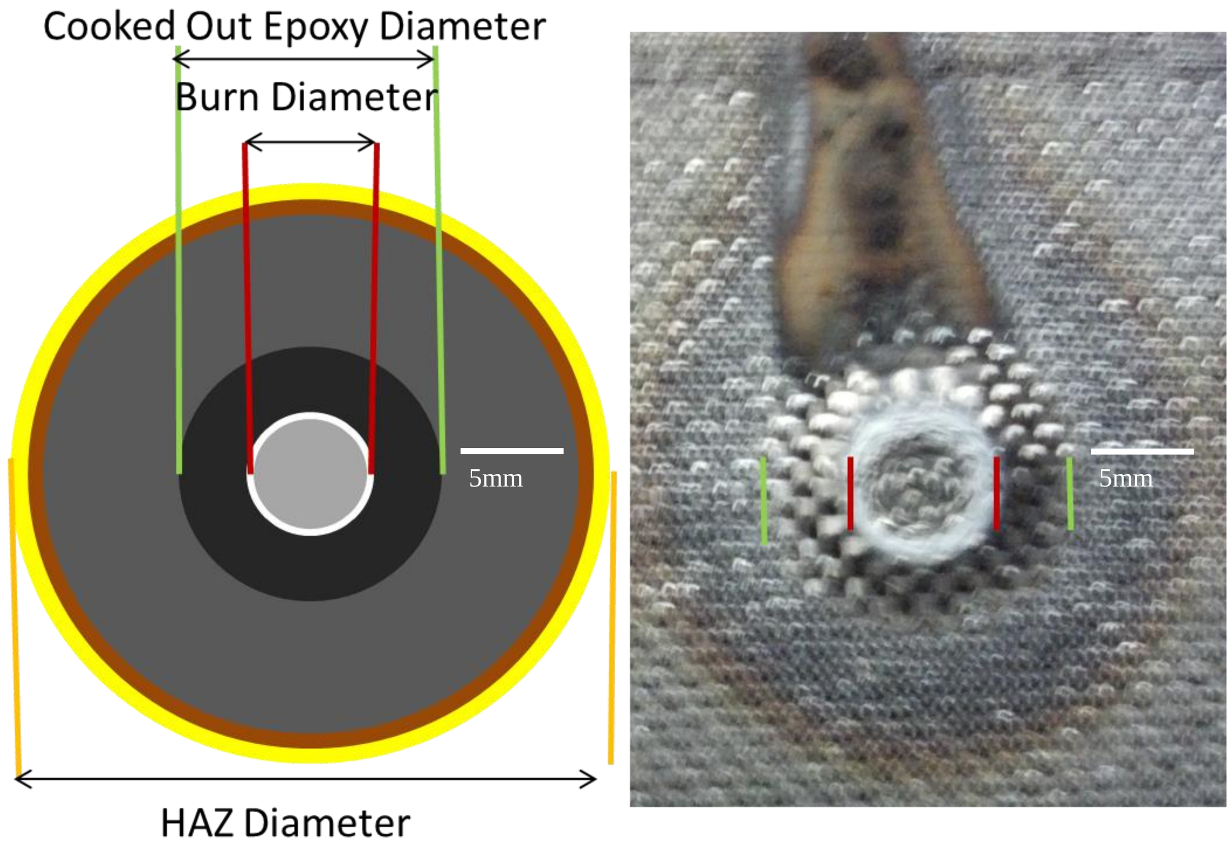

**Figure 22:** Left: Diagram of the measurements taken. Right: The front face of a 2.5mm thick CFRP sample irradiated for 300 s.

Post-test measurements were taken and then the data were compiled into a graph as shown below in Figure 23. All measurements were taken using digital calipers. A linear fit was applied to the hole depth. Logarithmic fits were applied to the hole diameter, epoxy damage diameter and HAZ diameter. This was done because at a time of zero, there must necessarily be zero damage done to the material, and therefore the damage must increase rapidly, most likely following a logarithmic curve. However, a bilinear relationship could not be ruled out and more research must be done at the low time scale and thin material region. Again, the difficulty with collecting data in this region is that the effects are smaller and therefore more difficult to measure.

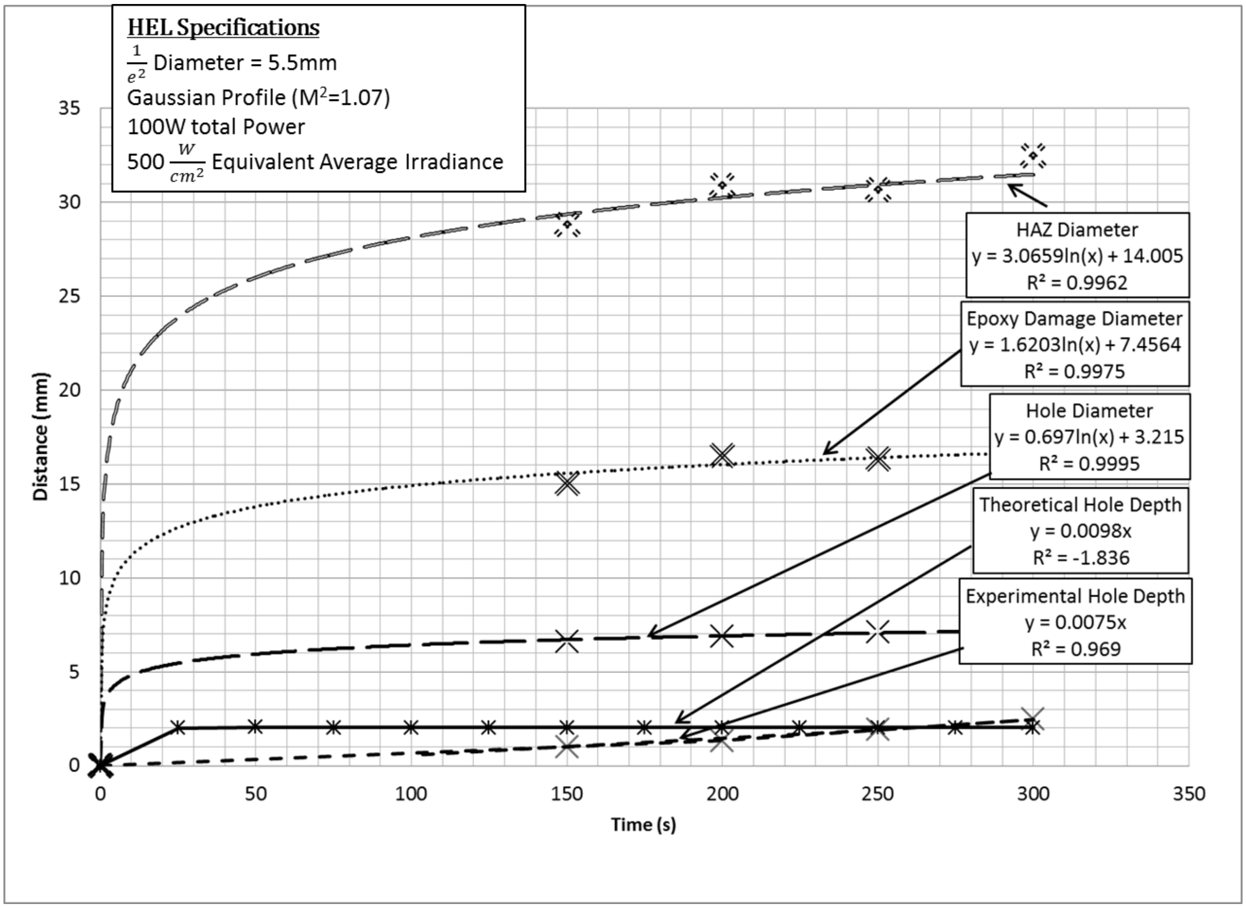

**Figure 23:** Measurements of the damage evolved to the CFRP sample upon irradiation.

The temperature of the front and rear face of the CFRP during irradiation were measured using IR/tc as described previously. Figure 24 shows the results of these measurements.

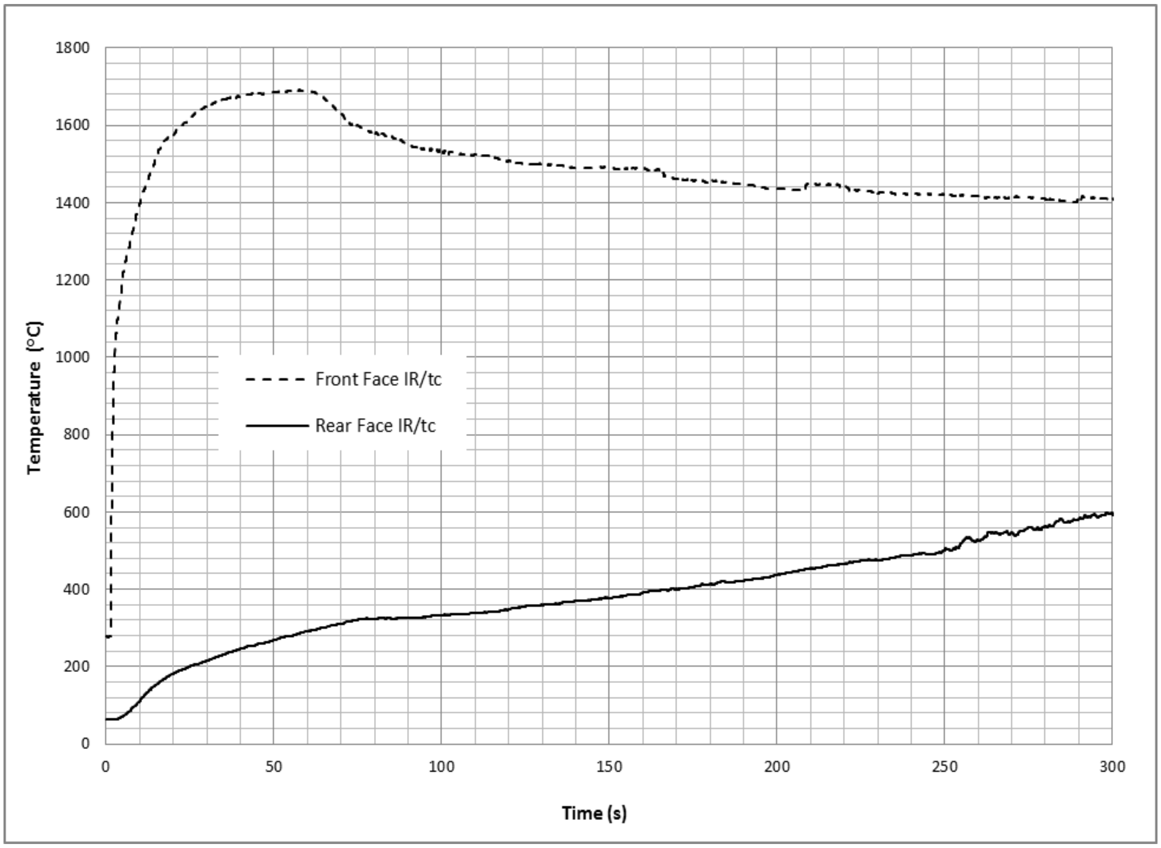

**Figure 24:** Measurements of the front and rear face temperature of CFRP during irradiation.

Table 4 shows the theoretical and experimental recession burn rates for Acrylite and CFRP as well as the percent difference between the two. This percent difference was calculated as the average of the difference in burn rate at each data point. The CFRP model predicts a bilinear shape which skewed the error compared to the linear experimental data.

**Table 4:** Comparison of experimental and theoretical results for CFRP and PMMA.

| Material | Theoretical Recession Rate (mm/s) | Experimental Recession Rate (mm/s) | % Difference (Average at each data point) | Theoretical Surface Temperature (ºC) | Experimental Surface Temperature (°C) | % Difference (average over interval) |
|---|---|---|---|---|---|---|
| Acrylite (Average for three samples) | 3.26 | 2.69 | <25% | - | - | - |
| CFRP | 0.007-0.08* | 0.007 | See Figure 23 | 1680 | 1400-1700 | <15% |

*Bilinear

The significant difference between recession rates in Acrylite and CFRP is due to the high temperature resistance of carbon fiber. This temperature resistance is enhanced by carbon fiber's efficiency as a blackbody emitter. A significant amount of energy is radiated away from the carbon fibers at high temperature, and the carbon fiber must remain at an elevated temperature for an extended period of time to be oxidized compared to the near instantaneous vaporization of the Acrylite.

Currently the Acrylite theoretical recession rate is greater than the experimental recession rate by 25% when measured as the average of the difference between each data point. This value is for the average of three separate materials and implies wide applicability. The HAZ predicted is qualitatively similar to the experimental HAZ. As of yet there has not been a comparison made between the temperatures predicted by the model to the experimental temperatures due to a lack of experimental temperature data (the IR/tc has too large of a time constant and cannot measure temperature accurately over the ~2s of irradiation the Acrylite is subjected to). This discrepancy could potentially be due to volumetric absorbance effects and unmeasured material property dependencies on temperature or heating rate. The effect of smoke in the beam propagation path was determined to be both difficult to quantify in the numerical model and experimentally negligible.

The CFRP model predicts a bilinear recession rate that cannot be meaningfully compared to the experimental recession rate. This is possibly due to the fact that the final material removal is based on reaching a fixed temperature of 1600 °C and not based on reaction rate kinetics. Furthermore, temperature and material degradation dependent data is needed for thermal conductivity values, especially because the model has high sensitivity to these values. Further investigation into the material properties and their high temperature dependence should be conducted to reduce the error associated with the model.

## CONCLUSIONS:

This research created a robust transient heat transfer model of HEL irradiation of composite and polymer materials. This model has applications in predicting the damage done and time to failure of UAVs and small boats when irradiated by HEL used as DEW. This could both enhance the survivability of US assets, as well as enhance the ability of HEL to defeat emerging foreign threats in the form of UAV and small boat attacks en masse.

The model uses material properties measured at USNA or by external collaborators on widely available analytical chemistry equipment like LFM, DSC, and FORS. This means that a model can be developed using properties based on knowledge of what the potential target is made of. The types of materials UAVs are made of do not vary much, and the material properties vary little within the family of CFRPsused.

The model includes material removal. This eliminates order of magnitude errors present when material removal is not included and also allows prediction of the hole developed and consequent structural damage to targets. This material removal mechanism is more computationally efficient than constant remeshing after each time step. Also, this mechanism handles the thermo-physical response of different materials and works for both phase change and oxidation, though further refinement is needed to include Arrhenius based reaction rate kinetics.

The models created for both carbon black loaded Acrylite GP and CFRP were experimentally validated. The model accurately predicts the thermal field developed qualitatively for both materials. This is useful in determining the extent of the HAZ and the thermal damage that would result in a loss of structural integrity and consequent failure of the structure. Quantitative comparisons were unable to be made for the Acrylite because of the short timescales involved. Quantitatively the CFRP front face surface temperature agrees within 15%, but there is a slight disagreement because of the heat generated by the combustion of the epoxy matrix.

Additionally, the model predicts the rate of material removal for both materials. For three different samples of carbon black loaded acrylate the average error was an overprediction of approximately 25%. This error could be due to heating rate dependency of some of the material properties that was overlooked. The max heating rate of the thermal analysis equipment available is significantly lower than the heating rate of a HEL and also only accommodates testing under an inert atmosphere. Latent heat values would likely change significantly under an oxidizing atmosphere. Additionally, these comparisons were made based on the assumption that the experimental data is completely accurate. Another potential source of error in the Acrylite model is the mechanism of laser absorption in Acrylite. This model treated the polymer as a surface absorber. When the photon flux of the laser beam is incident upon the surface, the photons are absorbed according to Beer’s law and the photon flux decreases exponentially over a very small distance. The size of this distance and if it is small enough to be approximated as the surface of the material is not known. If the photons are penetrating farther into the material, the material will be heated volumetrically and a surface heat flux is an incorrect approximation.

For the CFRP the error was difficult to quantify because the model predicted a bilinear shape, while the experimental data showed a linear response. The bilinear response is most likely due to a lack of Arrhenius based react rate kinetics in the model. These provide a transient term in the material removal mechanism that would act to slow down material removal in the CFRP and reduce the material removal rate in the direction of less error. This would also affect the first part of the bilinear shaped response and smooth the response to something more linear. Experimentally, more data are needed for thin laminates or low burn times in order to fully characterize the material response of CFRP to irradiation. The goal is to develop a model with as few empirical coefficients as possible, so that it is primarily physics based and most widely applicable. There is a variation in material properties at high temperatures that is difficult to characterize that causes error.

The ability to predict both material removal and the temperature field developed upon HEL irradiation has potential to both enhance offense and defensive capabilities for DEW. The developing threats of attacks en masse by UAV or small boats provide the perfect targets for these nascent DEW. Better prediction of their effects will ensure better employment of these weapons and will contribute to the continued dominance of the US Navy.

## FUTURE WORK

Future work to improve the CFRP model would include upgrading to fully anisotropic 3D to handle complicated UD composite laminates, inclusion of sandwich structured composites, and also the ability to predict temperature of structures behind or near the irradiated material based on thermal radiation generated by the hot surface. A preliminary 3D sandwich structure model was presented by Tresansky et al [26]. This model did not use measured properties or include phase change and was only qualitatively compared to previous experimental results, as the experimental results in this paper were not yet available.

Additional effects that would enhance the model would be the ability to model beams that are not perpendicular to the surface, as well as more complicated beam profiles that might include jitter or airy disks. This would make the model more generic, although the Gaussian profile used approximates these forms fairly well.

Including mechanical properties such as residual strength and stiffness into the model would make it possible to predict when HEL irradiation would cause a structure to fail. COMSOL is the perfect platform for this as it already contains an integrated solid mechanics module. All that is lacking are mechanical property measurements on laser damaged materials in order to make predictions about when irradiated structures would fail under loading.

Additionally, thermal expansion and other stress effects introduced by the high thermal gradients developed could be included in the model using the aforementioned solid mechanics module. This would enhance the fidelity of any structural failure predictions.

The fullest fruition of this research would be a model that can handle multiple angles of irradiance on different types of structures (composite laminates and sandwich structures) using material property inputs obtained via instruments available in most university chemistry labs. This model would be able to predict the mechanical strength of the structure following irradiation and when it would mechanically fail. Additionally, the thermal effects on components inside or behind the structure could also be predicted based on the thermal radiation emitted from the irradiated structure. This could be used to determine when a UAV or small boat would be defeated by an HEL and would enhance DEW capabilities.

## REFERENCES

[1] R. Flatley, An Overview of Development and Applications of Navy and Joint Directed Energy Weapons, Naval Surface Warfare Center Dahlgren. Presentation at United States Naval Academy, 18 September 2012. (FOUO)

[2] K. Kibler, H. Carter and J. Eisenmann, Residual Strength of Laser-Damaged Graphite Composites, General Dynamics, Ft. Worth, TX, *Journal of Composite Materials,* **9**, 1975.

[3] C. M. Medford, An Investigation into the Effect on Residual Strength of Composite Materials Following Irradiation by a High Energy Laser, United States Naval Academy EM496 Research Project, 3 May 2011.

[4] U. Sorathia, Materials and Fire Threat, *Fire Technology*, **33**, 1997.

[5] C. Pan, Evaluation of Anisotropic Thermal Conductivity for Unidirectional FRP in Laser Machining*, Composites Part A,* **32,** 2001.

[6] C. Pan, Prediction of Extent of HAZ in Laser Grooving of Unidirectional Fiber Reinforced Plastics, *Journal of Engineering Materials and Technology,* **120,** 1998.

[7] E. Uhlmann, The Extent of Laser Induced thermal Damage of UD and Crossply Composite Laminates, *International Journal of Machine Tools & Manufacture,* **39**, 1999.

[8] W. Rodden, A Comprehensive Study of the Long Pulse Nd:YAG Laser Drilling of Multi-Layer Carbon Fiber Composites, *Optics Communications,* **210**, 2002.

[9] M. Islam, Thermal Conducitivty of Fiber Reinforced Composites by the FEM, *Journal of Composite materials*, **33,** 1999.

[10] J. McClay, P. Joyce, and A. Smith, Determination of the Directional Dependent In-Plane Thermal Conductivity of K63B12 Pitch-Fiber/Epoxy Composite, *Paper IMECE2004-6000 In Proceedings of the International Mechanical Engineering Congress and Exposition* 2004 (IMECE 2004), American Society of Mechanical Engineers (ASME). November 13-19, 2004, Anaheim CA. CD-ROM.

[11] C. Cheng, Application of a 3-D Heat Flow Model to Treat Laser Drilling of Carbon Fiber Composites, *Acta Metallurgica*, 1998.

[12] T. Hirogaki, Prediction of Damage Width in Laser Drilling of Printed Wiring Board using FEM, *ICCM Proceedings*, 1997

[13] M. Dell'erba, An Experimental Study on Laser Drilling and Cutting of Composite Materials for the Aerospace Industry Using Excimer and $CO_2$ Sources, *Composites Manufacturing*, **3**, 1992.

[14] H. Zhou, Transient Temperature Rises In a Sandwich Structured Composite Induced by a Dithering or Rotating Laser Beam, *IOSR Journal of Engineering*, **2,** 2012.

[15] J. Zhang, L. Long, Finite Element Simulation for Laser Ablation of Carbon Fiber Epoxy Composite, *Applied Mechanics and Materials*, **66**, 2011.

[16] B. Garrison, Laser Ablation of Organic Polymers: Microscopic Models for Photochemical and Thermal Processes, *Journal of Applied Physics*, **57**, 1985.

[17] L. Nikitin, Calculation of the Temperature of Polymer or Composite Surfaces Placed in an Infrared Laser Field, *Mechanics of Composite Materials*, **31**, 1995.

[18] R. Cozzens, High Energy Laser Interactions with Organic Matrix Composites, *Naval Research Laboratory*, 2007. (FOUO)

[19] C. Lloyd, Ablative Polymeric Materials for Near-Infrared High-Energy Laser Beam Diagnostics, *Journal of Directed Energy*, 3, 2009.

[20] P. Nielsen, Effects of Directed Energy Weapons. Directed Energy Professional Society: Albuquerque NM, 2009.

[21] Solid State laser Technology Maturation program WAREX, *ONR*, 2012. (Distribution F).

[22] C. Lloyd, Near Infrared Laser Ablation of Organic Polymeric Materials, Doctoral Thesis, 2009.

[23] A. Kaw, Mechanics of Composite Materials. Taylor and Francis: Boca Raton, FL, 2006.

[24] G. Springer and S. Tsai, "Thermal Conductivities of Unidirectional Materials." *Journal of Composite Materials*, v 1, n 1, 1967, p 166-173

[25] M. Kulkarni and R. Brady, A Model of Global Thermal Conductivity in Laminated Carbon/Carbon Composites, *Composites Science and Technology*, **57**, 1997, p 277-285.

[26] A. Tresansky, P. Joyce, J. Radice, Numerical Modeling of the Heat Transfer from HEL Irradiation of Composite Sandwich Structures, *Directed Energy Professional Society Proceedings*. April, 2012, Gaithersburg, MD.

[27] J. Puishys, P. Joyce, Damage Tolerance of Laser Irradiated Composite Sandwich Structures *USNA*, 2011.

[28] Y. Yin, J.G Binner, T.E. Cross, The Oxidation Behaviour of Carbon Fibres, *Journal of Materials Science*, **29**, 1994, p 2250-2254.

[29] IPG Photonics YLR-100-AC Instruction Manual. Publication P21-010067, Rev. B, 2009.

[30] T. Bergman, Introduction to Heat Transfer, Wiley Publishing, Jefferson City. 2011.

[31] E. Kreyszig, Advanced Engineering Mathematics, Wiley Publishing, Jefferson City. 2011.

[32] C. Walters, D. Seibert, B. Childers, A. Cain, Laser Beam Penetration of Generic Composite Wing Components, *Directed Energy Professional Society Laser Lethality Conference*, 5 April 2012. (FOUO)

## **APPENDIX A:** DSC PROCEDURE

DSC was performed with a TA Instruments DSC 2010 (shown below) with the following specifications:

| TA Instruments DSC 2010 Specifications | |
|---|---|
| Max Temperature | 750 ºC |
| Max Sample Volume | $10mm^3$ |
| Sample Mass | 0.5-100mg |
| Purge Gas ($N_2$) Flow Rate | 25-50mL |
| Cell Volume | $200mm^3$ |
| Temperature Repeatability | +0.1 ºC |
| Thermocouple Typer | Chromel/Alumel (K) |
| Calorimetric Sensitivity | 1 µW |
| Baseline Noise | 0.5 µW |

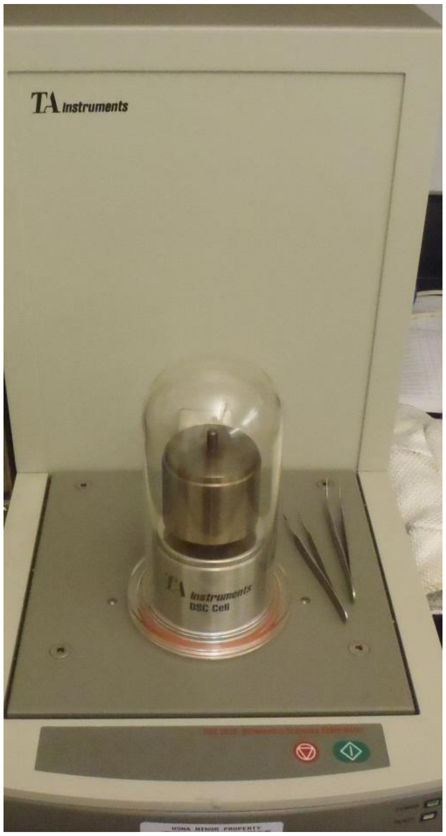

**Figure A1:** TA Instruments DSC 2010 used for Experiments

The testing was conducted at a 10°C/min heating rate in Aluminum pan under nitrogen. The procedure used follows:

1) Prepare sample by machining into flakes or powder
2) Carefully weight 2 sets of top and bottom pans that are of a matched weight. This eliminates steady state error in the differential measurements.

3) Prepare two samples, a sample pan and a reference pan. The sample pan should contain the sample to be measured. The difference in weight between the two pans is the sample weight.
4) Seal the two pans using the press (shown below)
5) The DSC measures the difference in heat flow between the two pans; the difference in heat flow is the heat flow into the sample. This specific heat flow can be used to determine the effective specific heat
6) Three runs should be conducted per material and the results averaged to eliminate variation in the measurements

**Figure A2:** Press used to prepare samples in aluminum pans (shown)

## **APPENDIX B:** ACRYLITE DSC MEASUREMENTS

Three types of Acrylite were purchased from Evonik industries and investigated by DSC using the method described previously. Acrylite 9H01 GT is a cell cast PMMA, Acrylite 9M001FF and Acrylite GP are extruded, all are loaded with carbon-black for color The GT and GP samples had a nominal thickness of 0.25” and the FF had a nominal thickness of 0.125”, although this varied enough in each sample to necessitate measurement at each individual burn test site. Samples were collected as the shavings from a band saw used on the materials. Care was taken to collect large samples and mix them to average out any non-homogeneity. Data for each of the tests run is shown. The raw data that includes the time derivative of temperature as well as the specific heat flow from the DSC are shown are plotted as the three tests for each material. The computed effective specific heat follows.

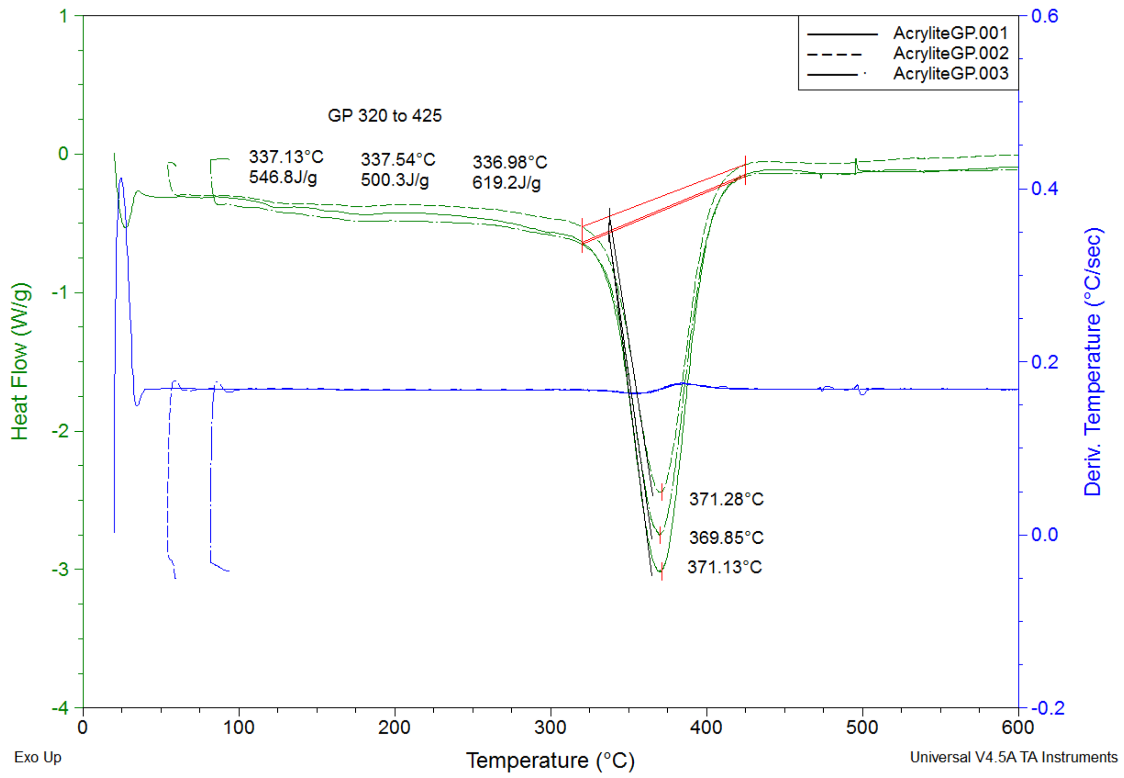

**Figure B1:** Data from DSC for three runs of Acrylite GP. Specific heat flow is shown in green and the derivative of temperature with respect to time is shown in blue.

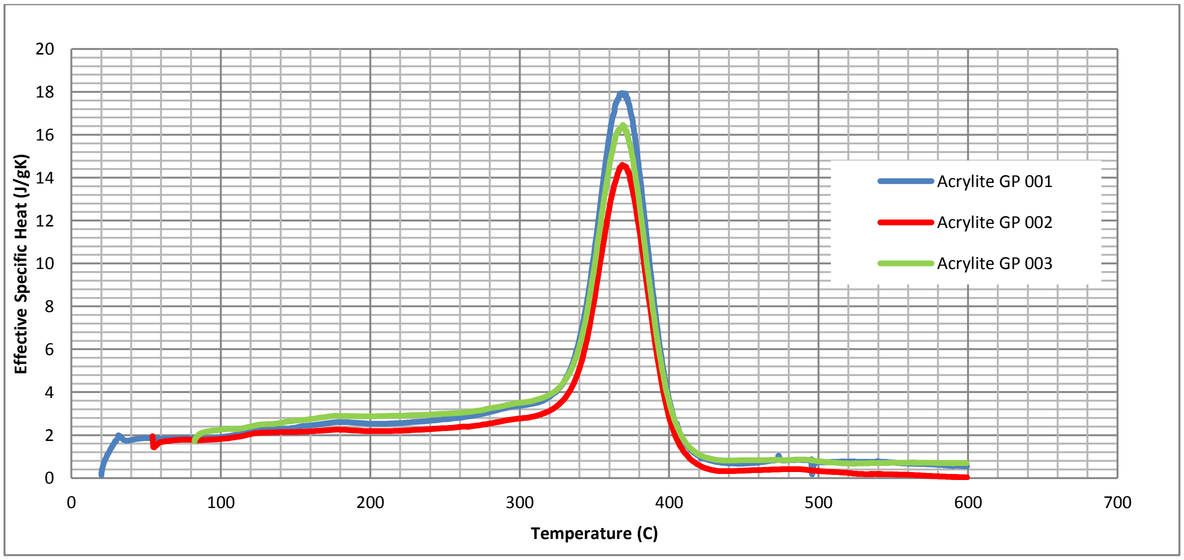

**Figure B2:** The effective specific heat computed from the DSC measurements for Acrylite GP.

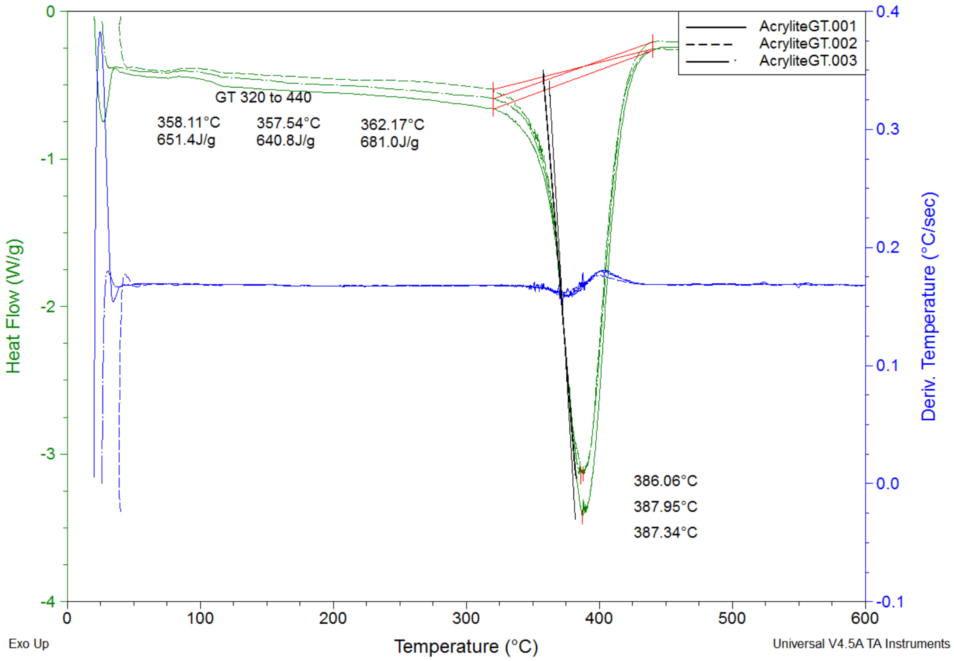

**Figure B3:** Data from DSC for three runs of Acrylite GT. Specific heat flow is shown in green and the derivative of temperature with respect to time is shown in blue.

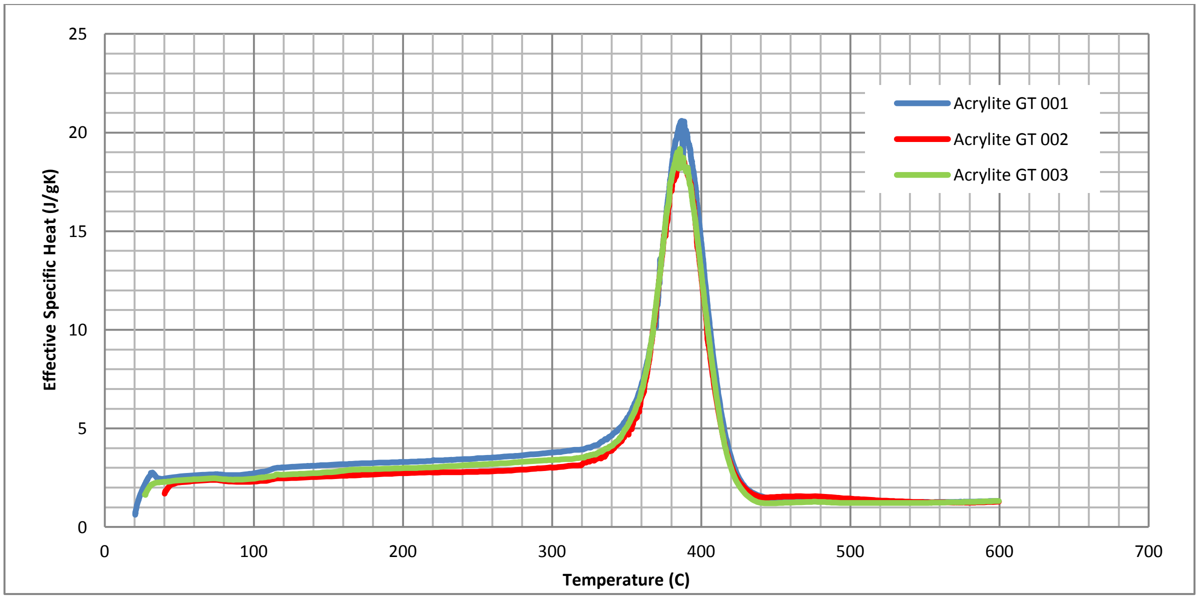

**Figure B4:** The effective specific heat computed from the DSC measurements for Acrylite GT.

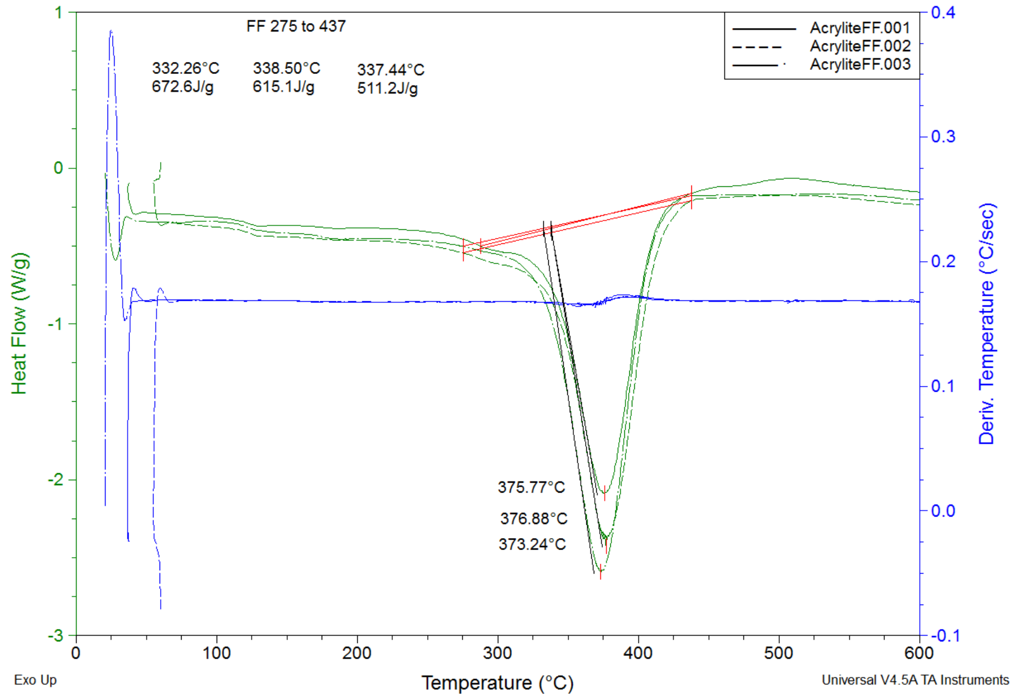

**Figure B5:** Data from DSC for three runs of Acrylite FF. Specific heat flow is shown in green and the derivative of temperature with respect to time is shown in blue.

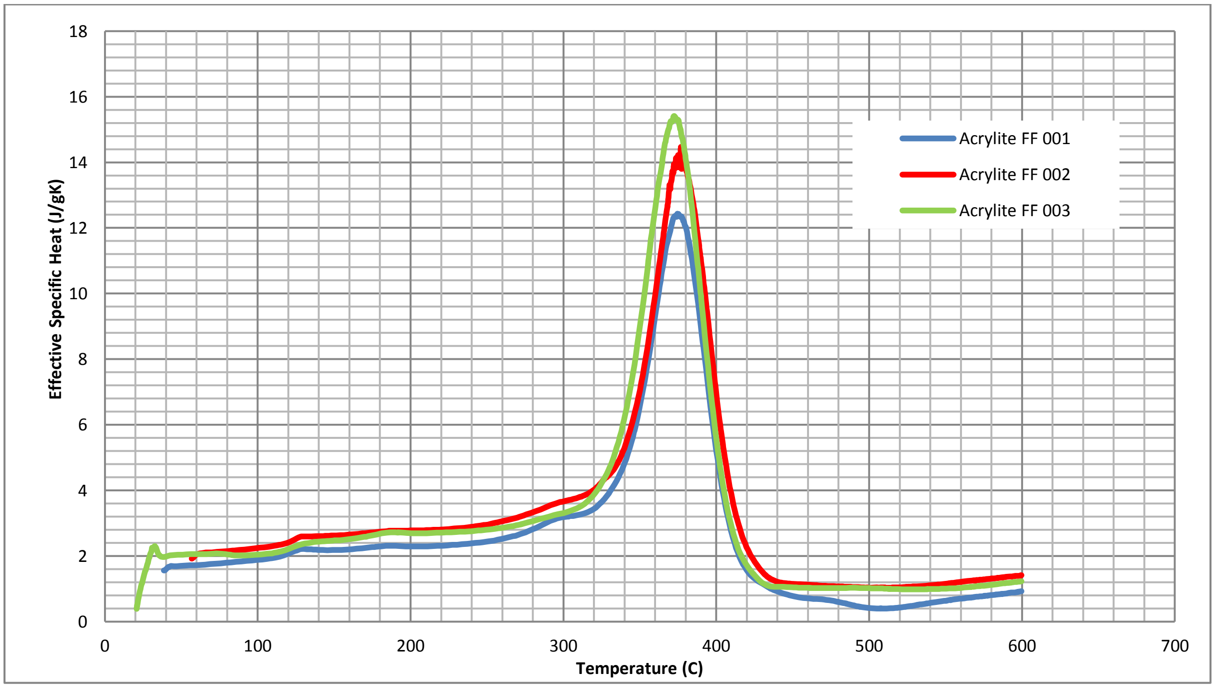

**Figure B6:** The effective specific heat computed from the DSC measurements for Acrylite GT.

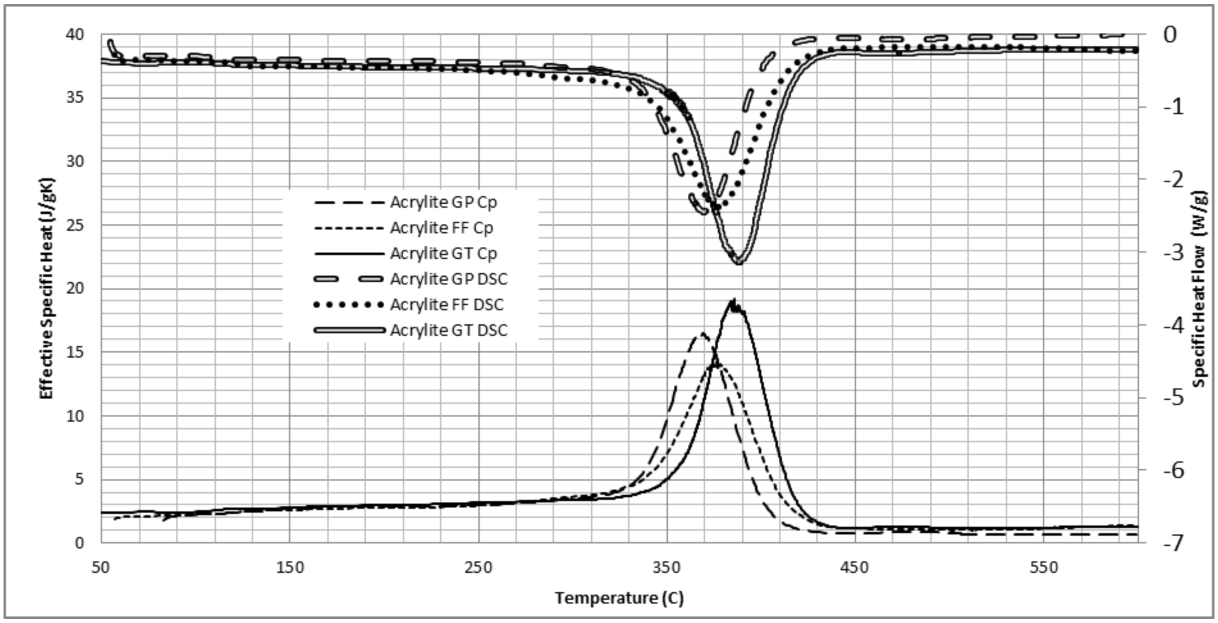

**Figure B7:** Comparison of three run average for Acrylite GP, GT, and FF for specific heat flow and effective specific heat.

## **APPENDIX C:** CFRP DSC MEASUREMENTS

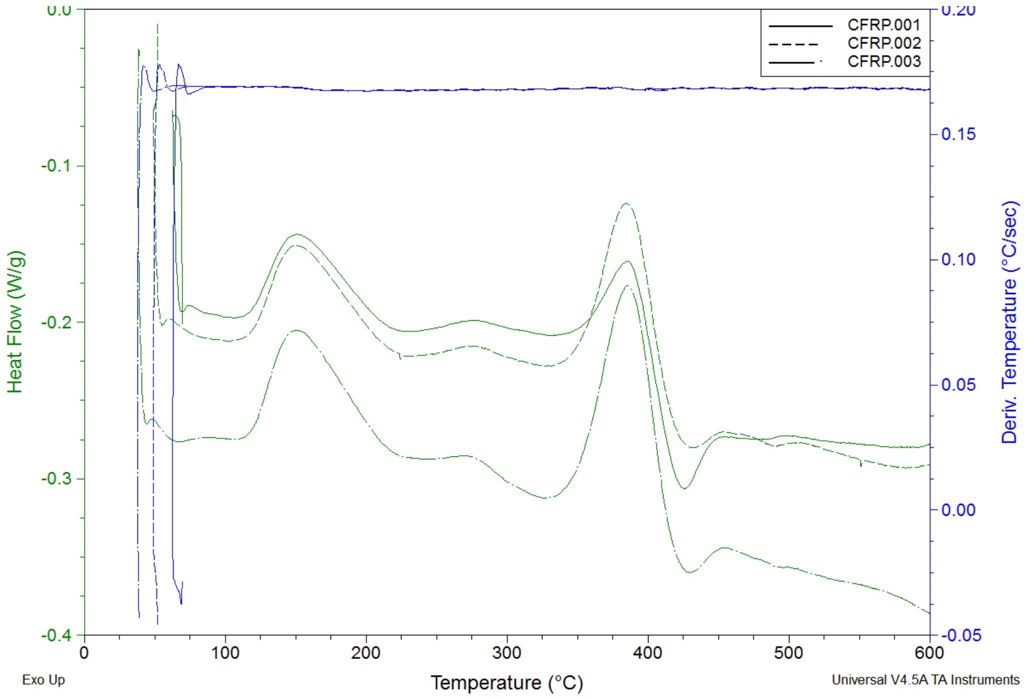

**Figure C1:** Data from DSC for three runs of CFRP. Specific heat flow is shown in green and the derivative of temperature with respect to time is shown in blue.

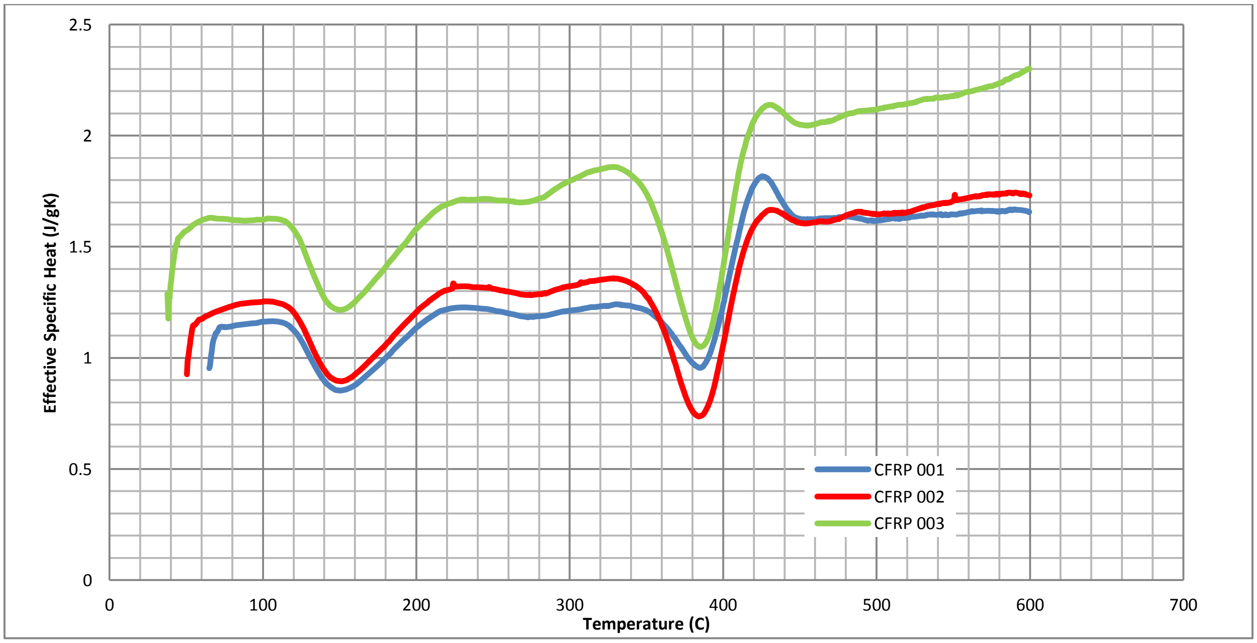

**Figure C2:** The effective specific heat computed from the DSC measurements for CFRP.

## **APPENDIX D:** LASER FLASH METHOD MEASUREMENTS

Laser flash measurements were conducted on CFRP to determine its thermal conductivity. The thermal conductivity of Acrylite was known from the material data sheet. Lash flash works by heating one side of a sample material with a laser pulse of known energy, and then measuring the response on the other side of the sample to determine the thermal diffusivity of the material. The thermal conductivity of the material can then be calculated given the specific heat and the density. LFM was performed by Dr Jin Park at the High Performance Materials Institute of Florida State University using a Netzsch LFA 457 laser flash diffusivity machine (shown) following ASTM E1461 guidelines. The specifications for the machine follow:

| Netzsch LFA 457 MicroFlash Laser Flash Diffusivity Machine Specifications | |
|---|---|
| Temperature Range | -125 to 500 or RT to 1100°C |
| Heating and Cooling Rates | 0.01 K/min to 50K/ min |
| Laser Pulse Energy (max) | 18 J/pulse |
| Measuring Range Thermal Diffusivity | 0.01 mm/s to 1000mm/s |
| Sample Dimensions | 10mm x 10mm x 1mm |

**Figure D1:** Netzsch LFA 457 Laser Flash Diffusivity Machine.

# **APPENDIX E:** FIBER OPTIC REFLECTANCE SPECTROSCOPY MEASUREMENTS

Point-based reflectance spectra were collected two different ways. Once was conducted offsite at The National Gallery with a fiber-optic spectrometer (Fieldspec-3, ASD Inc., Boulder, CO) (shown) on Acrylite. The FORS spectrometer operates from 350-2500 nm (28,571-4000 cm$^{-1}$). The spectral sampling rate is 1.4 nm from 350-1000 nm and 2.0 nm from 1000-2500 nm. An illumination probe utilizing a halogen bulb (model A122317, ASD Inc.) is held ~5 cm from the surface, providing ~5000 lux. Integration time is 100 msec, and 64 spectra are averaged for each measurement.

**Figure E1:** FieldSpec 3 Fiber Optic Spectrometer.

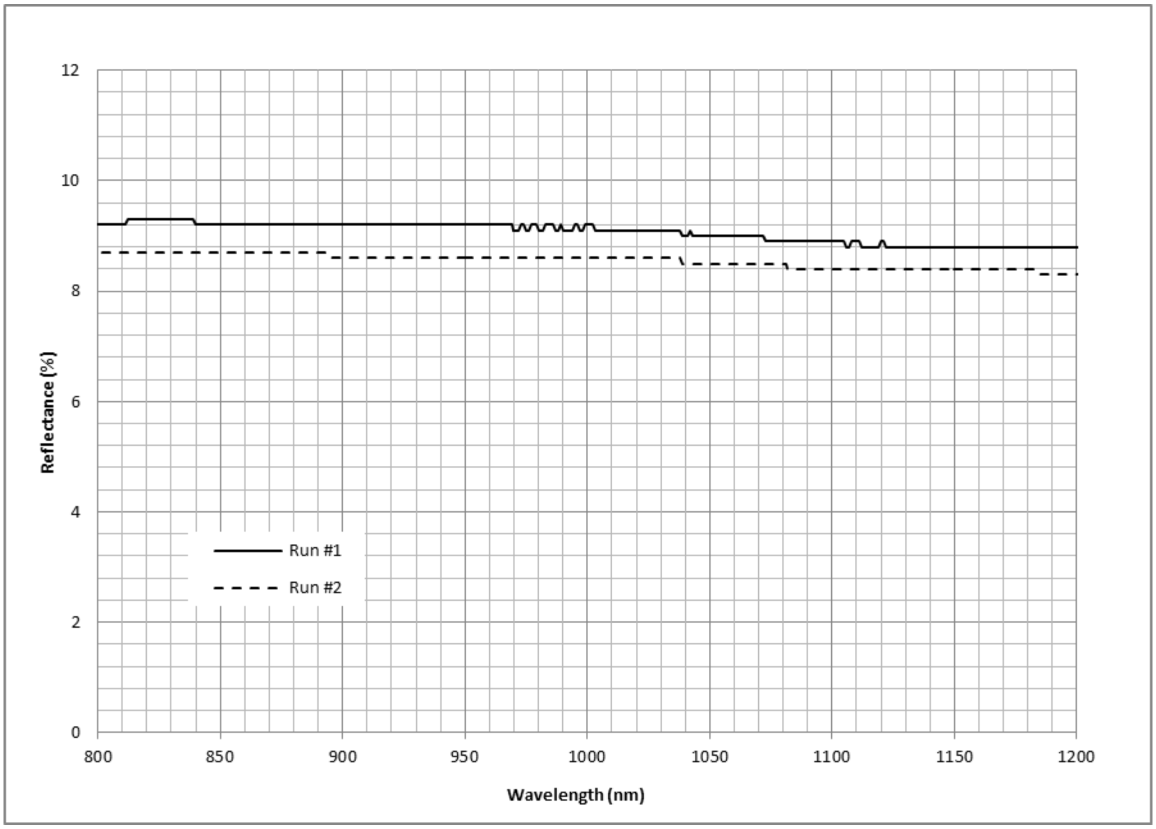

**Figure E2:** FORS data collected for a sample of Acrylite GP.

Acrylite GP was found to have a surface reflectance of approximately 9% and therefore a surface absorbance of 91%.

Measurements for CFRP were performed at USNA using a Jasco V-670 spectrophotometer (shown).

**Figure E3:** Jasxo V-670 NIR/vis Spectrophotometer.

Two sets of measurements were conducted and the results were averaged to determine that the reflectivity of CFRP was approximately 9% and the absorptivity was therefore 91% at 1.07μm.

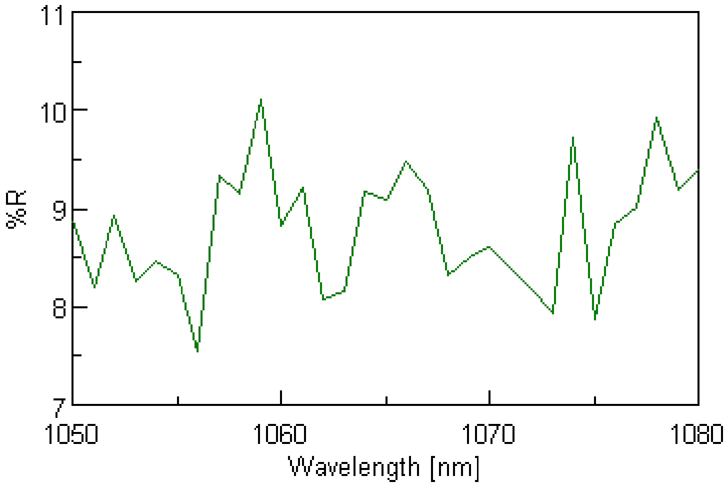

**Figure E4:** CFRP sample 1 tested by NIR spectroscopy at USNA.

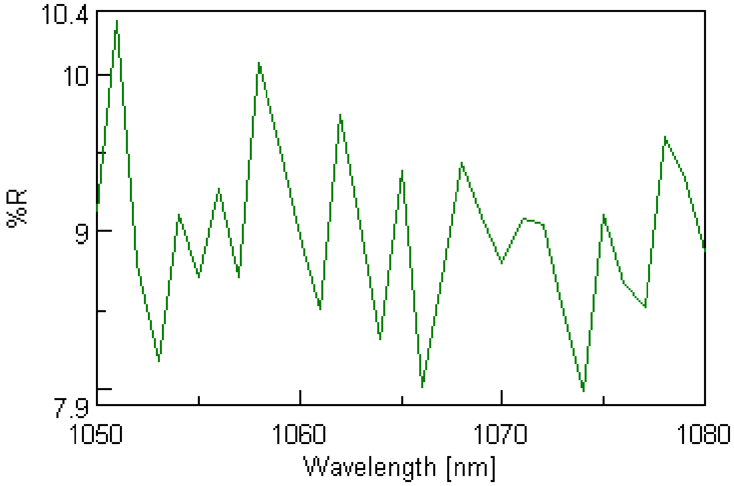

**Figure E5:** CFRP Sample 2 tested by NIR Spectroscopy at USNA

| Jasco V-670 Vis/NIR Spectrophotometer | |
|---|---|
| Optical System | Single monochromater, dual grating, dual detector, Czerny Turner Mount, Double Beam |
| Light Source | Halogen Lamp |
| Detector | Photomultiplier tube |
| Wavelength Range | 190-2700nm |
| Wavelength Accuracy | 1.5nm NIR region |
| Scanning Speed | 10-4000nm/min |

## **APPENDIX F**: HELSPECIFICATIONS

An IPG Photonics model YLR-100 AC HEL (shown) was used for the experimental testing.

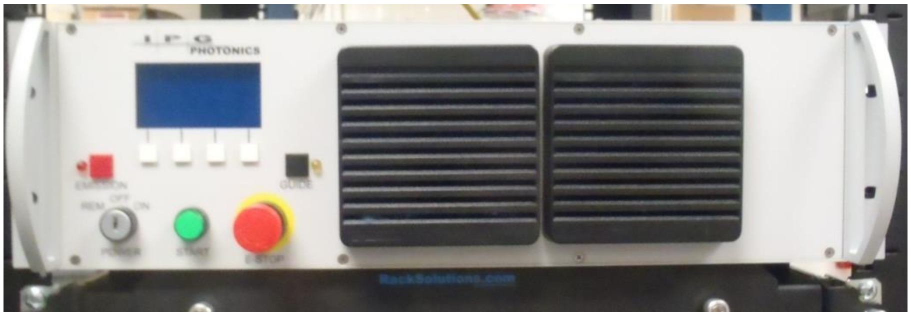

**Figure F1:** IPG Photonics YLR-100-AC HEL used for testing.

The laser is produced in the above rack mounted unit. A fiber laser has the lazing media in a long coaxial fiber optic cable. This allows the pumping diode to be pumped along the length of the fiber in a highly efficient manner. The laser is output via another fiber optic cable and this cable is terminated in a beam collimator that produces the final 5.5mm 1/e$^2$ beam diameter. The fiber is made of Ytterbium doped Yttrium Aluminum Garnet (Yb:YAG).

**Figure F2:** 5.5mm maximum diameter beam collimator

| IPG Photonics YLR-100 AC HEL | |
|---|---|
| Output Mode | Continuous Wave |
| Nominal Power | 100W |
| Switching On/Off Time | 30 µs |
| M$^2$ | 1.07 (max 1.1) |
| 1/e$^2$ Beam Diameter | 4.5-5.5mm |
| 1/e$^2$ Beam Divergence | 0.3 mrad |
| Cooling | Forced Air |
| Power Consumption | 400W (500W max) |
| Wavelength | 1070nm (1060-1100nm full range) |

## **APPENDIX G:** IR/TC MEASUREMENTS

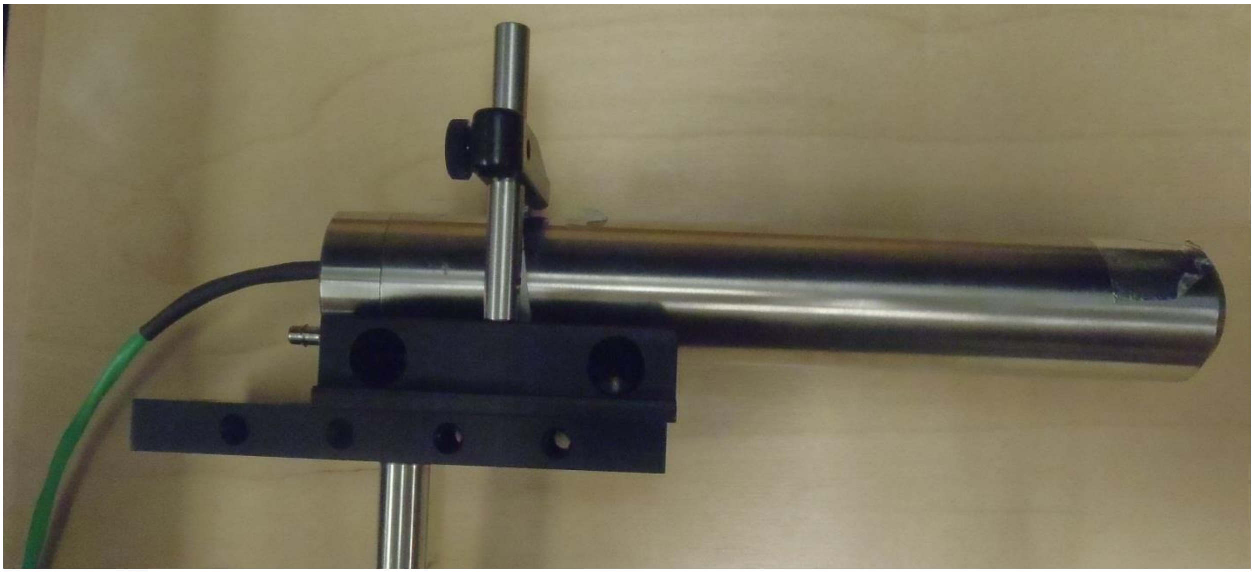

**Figure G1**: Omega OS-37-60CF-S Infrared Thermocouple

Omega produces an Infrared non contact temperature measuring device called an IR thermocouple or IR/tc (shown). Multiple models are available so the model with the tightest focal range and highest temperature range was selected. The IR/tc measures the infrared radiation from a surface and determines its temperature based on radiation laws. What makes the IR/tc different from a radiometer or a IR camera is that it does it in a self powered package that outputs the temperature as an easy to read thermocouple signal that can be measured by a thermocouple card or similar analog I/O device. Specifications follow:

| Omega OS-37-60CF-S IR/tc | |
|---|---|
| Sensing Range | 540 to 2760 °C |
| Field of View | 1° |
| Distance to spot ratio | 60:1 |
| Required Target Emissivity | >0.7 |
| Spectral Response | 2 to 20 µm |
| Output Impedance | 4 to 8kΩ |
| Dimensions | 213x35mm cylindrical |

The IR thermocouple measures the temperature of a surface based on its emitted radiation. The intensity and spectral composition of the radiation that lands on the sensor determines what temperature it outputs as a reading. This depends on surface emissivity, orientation and view factors. In order to properly calibrate the sensor it was necessary to have a suitably hot (~700-1000C) surface with similar emissivity in a similar orientation to that tested. Therefore a piece of carbon/carbon composite which has a similar surface to CFRP but will withstand heating much better was heated with a blowtorch while a K-type metal thermocouple measured the surface temperature directly. The IR/tc were oriented as shown and when the K-type thermocouple showed a steady state temperature were then calibrated to match.

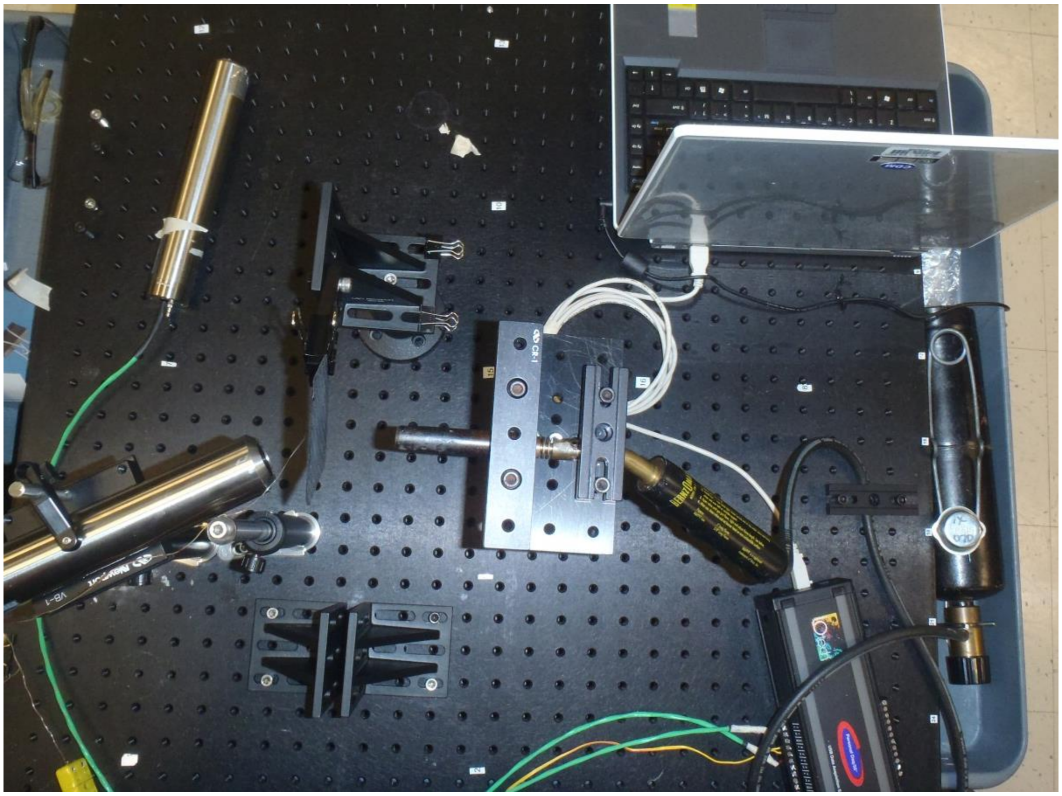

**Figure G2:** Calibration setup for IR/tc.

The IR/tc were then installed on the optical table for testing with the HEL as shown. The geometry was matched as closely as possible to avoid introducing error into the calibration.

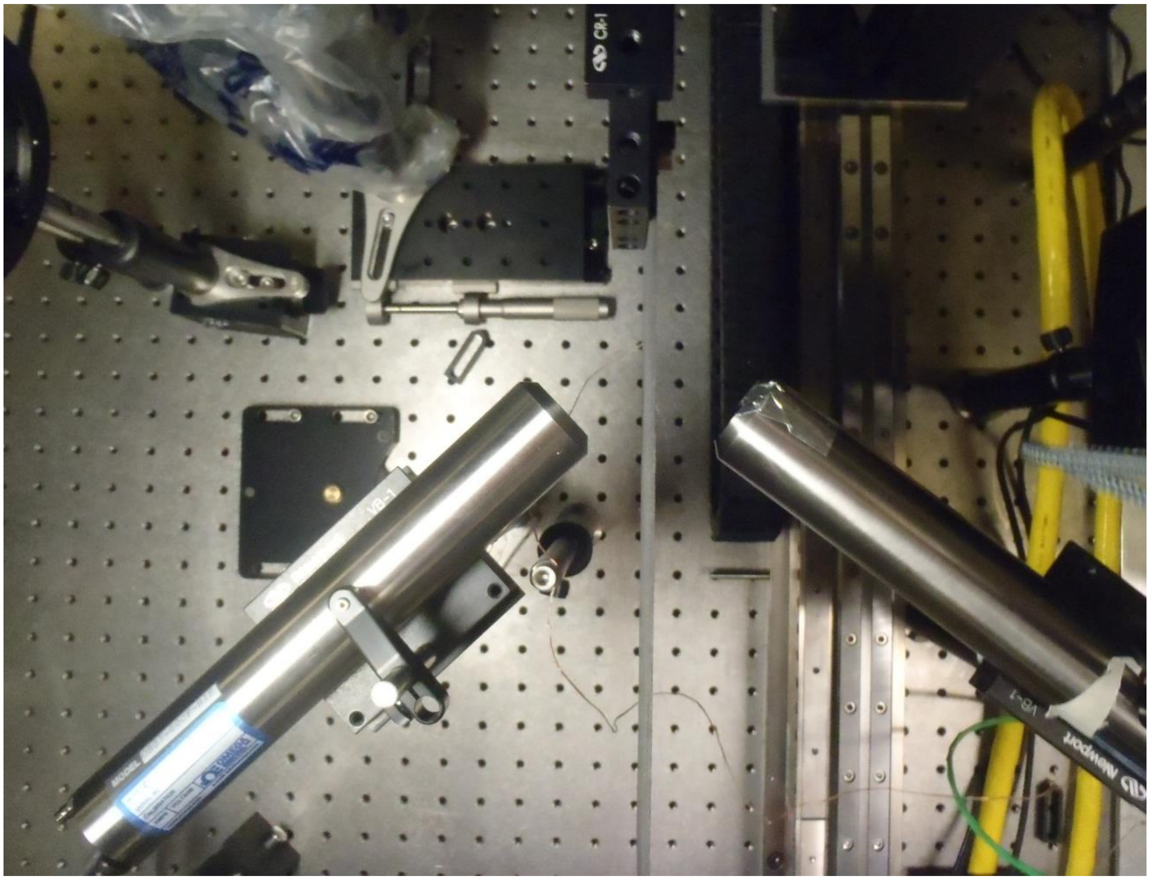

**Figure G3:** The experimental setup with IR/tc in place.